Early Dynamics and Evolution of Extrasolar Planetary Systems

Thesis by
Max Goldberg

In Partial Fulfillment of the Requirements for the
Degree of
Doctor of Philosophy

Caltech

CALIFORNIA INSTITUTE OF TECHNOLOGY
Pasadena, California

2024
Defended February 5, 2024

What has been will be again,
what has been done will be done again;
there is nothing new under the sun.
- *Ecclesiastes*

Sick of tea? That's like being sick of breathing!
- *Uncle Iroh*

ACKNOWLEDGEMENTS

First and foremost, I want to thank my advisor, Konstantin Batygin, for leading me through the incredible experience of a PhD. You taught me that one can be an astrophysicist, gin enthusiast, entrepreneur, and rockstar all in one, and how those add up to be more than the sum of their parts. I never cease to be amazed by your limitless curiosity and deep intuition. I am also incredibly grateful to Olga for being ever-welcoming and so eager to share Russian culture. Thank you as well to the other members of my thesis committee—Andrew Howard, Jim Fuller, Lynne Hillenbrand, and Dimitri Mawet—for many enriching discussions and useful feedback during my time at Caltech.

I have also benefited from an exceptional research group to bounce ideas off of. Juliette Becker, Gabriele Pichierri, Matt Belyakov, Valeria Kachmar, Ian Brunton, and the many more who have come and gone, you are great colleagues and friends, and I have no doubt we will cross paths again in the future. I am fortunate to have had as collaborators and mentors Fei Dai, Rogerio Deienno, André Izidoro, Seth Jacobson, David Nesvorný, Erik Petigura, Lauren Weiss, Jon Zink, and my undergraduate advisor Dan Fabrycky, who started me on this journey into celestial mechanics.

Public outreach and education unexpectedly became a major part of my time at Caltech. I have the deepest appreciation and respect for Cameron Hummels, who has succeeded in building an incredible outreach program in the department and demonstrated to me what an important role astronomy can play in the community.

I am indebted to the fantastic support staff at Caltech, especially Ruth Loisel, who sorted through my piles of foreign receipts and fought for all of us even in the toughest situations, and Gita Patel, for her expert managing of the department.

It would be impossible to have a better set of grad students than the Astronomy and Planetary Science departments. Thank you for the donuts, beer, softball pitches, rides into the desert, and skiing companionship. Special thanks to classmates, officemates, and friends over the years—Sarah Blunt, Adolfo Carvalho, Maria Camarca, Dillon Dong, Dee Dunne, Julie Inglis, Viraj Karambelkar, Evan Núñez, Sam Ponnada, Tony Rodriguez, Lee Rosenthal, Ryan Rubenzahl, Yashvi Sharma, Kaew Tinyanont, Sam Wu, Jerry Xuan, and Zhuyun Zhuang—to name a few.

I am enormously grateful to the students and staff of the Observatoire de la Côte d'Azur for welcoming me into their world for the three months I spent there. Thank you to Antoine Petit, Morby, Max Mahlke, Nico Müller, Fabiola Gerosa, Marjorie Galinier, Harrison Agrusa, Steve Markham, and many more. Those late nights on the beach and lunches *chez Khaled* were unforgettable.

Finally, thank you to my family, and especially my parents, for their support and encouragement during a quarter-century of schooling and science. I really couldn't have gotten here without you.

ABSTRACT

Of the thousands of discovered exoplanets, the vast majority were born billions of years ago. The process of their formation is only a tiny fraction of their lifespan and observing formation of new planets is very difficult with current techniques. However, these planets, and the planetary systems they are a part of, retain distinct fingerprints of how and when they formed. This thesis presents six studies that aim to uncover the environment in which planets form by investigating how the architectures of multiplanet systems are shaped by physical processes. I show that varying degrees of planet-planet interactions, planet-disk interactions, and tidal dissipation successfully reproduce many of the planets we see today.

Chapters 2 and 3 argue that violent dynamical instabilities are a key element of the formation process for compact systems of multiple planets of the sort detected by the Kepler space telescope. A major problem in planet formation is that during the protoplanetary disk phase, planets capture into chains of mean-motion resonances, but most planets observed today are not in such resonances. I show how resonant chains broken through dynamical instabilities reproduce several bulk features of the small planet census. I also derive a stability boundary for resonant systems that can predict which systems will go unstable in the future.

For the small fraction of systems that remain resonant, detailed analysis of their architectures can recover diverse properties of the protoplanetary disk environment and orbital histories of the planets. In Chapters 4, 5, and 6, I demonstrate that while some systems, like Kepler-221, experienced strong tidal dissipation inside the planets, others, such as TOI-1136, experienced very little. Disk conditions vary as well: TOI-1136 had a disk with low surface density and weak turbulence, while the large population of near-resonant Kepler planets requires a source of perturbation, such as MRI-driven turbulence.

Similar processes unfold in the satellite systems of giant planets, which are akin to scaled-down exoplanet systems. I show in Chapter 7 that Hyperion, an irregularly shaped satellite of Saturn, experiences strong tidal dissipation from chaotic tumbling that keeps it in mean-motion resonance with Titan, resolving a long-standing problem in Solar System dynamics.

PUBLISHED CONTENT AND CONTRIBUTIONS

Dai, F., Masuda, K., Beard, C., et al. (Feb. 2023). "TOI-1136 Is a Young, Coplanar, Aligned Planetary System in a Pristine Resonant Chain." In: *The Astronomical Journal* 165, p. 33. ISSN: 0004-6256. DOI: `10.3847/1538-3881/aca327`.
M.G. participated in the analysis and interpretation of the TTV data, advised the setup of the migration simulations, and helped write the manuscript.

Goldberg, M. & Batygin, K. (May 2023). "Dynamics and Origins of the Near-resonant Kepler Planets." In: *The Astrophysical Journal* 948, p. 12. ISSN: 0004-637X. DOI: `10.3847/1538-4357/acc9ae`.
M.G. conceived the project, conducted the numerical experiments, and wrote the manuscript.

Goldberg, M. & Batygin, K. (May 2022). "Architectures of Compact Super-Earth Systems Shaped by Instabilities." In: *The Astronomical Journal* 163, p. 201. ISSN: 0004-6256. DOI: `10.3847/1538-3881/ac5961`.
M.G. conceived the project with input from collaborators, conducted the numerical experiments, and wrote the manuscript.

Goldberg, M., Batygin, K. & Morbidelli, A. (Dec. 2022). "A Criterion for the Stability of Planets in Chains of Resonances." In: *Icarus* 388, p. 115206. ISSN: 0019-1035. DOI: `10.1016/j.icarus.2022.115206`.
M.G. conceived the project with input from collaborators, derived analytical expressions and conducted the numerical experiments, and wrote the manuscript.

Goldberg, M. & Batygin, K. (July 2021). "A Tidal Origin for a Three-body Resonance in Kepler-221." In: *The Astronomical Journal* 162, p. 16. ISSN: 0004-6256. DOI: `10.3847/1538-3881/abfb78`.
M.G. conceived the project, conducted the numerical experiments, and wrote the manuscript.

TABLE OF CONTENTS

LIST OF ILLUSTRATIONS

LIST OF TABLES

Chapter 1

INTRODUCTION

Astronomers long suspected that other stars harbored planets, but the exoplanet revolution began with a pair of unexpected discoveries. In 1992, Wolszczan & Frail found planets orbiting a millisecond pulsar, the remnant of a supernova. Three years later, Mayor & Queloz (1995) found a Jupiter-mass planet with an orbital period of just 4 days around a main sequence star, work which earned them the Nobel Prize in Physics in 2019. We now know that these two classes of objects, pulsar planets and Hot Jupiters, are intrinsically rare (Niţu et al., 2022; Howard et al., 2010). But the discoveries shattered any pretenses astronomers had that extrasolar planetary systems would resemble our own Solar System. Planets in the universe must form and evolve in a far broader range of circumstances, and via a more extensive set of mechanisms, than what transpired around the Sun.

The *Kepler* mission further cemented the oddness of the Solar System. While it arguably failed to accomplish its stated goal of determining the frequency of Earth-like planets (Kunimoto & Matthews, 2020), *Kepler*'s legacy is its discovery of thousands of planets with sizes between Earth and Neptune within one astronomical unit of their host stars (Borucki et al., 2011). These sub-Neptunes and super-Earths are ubiquitous in the galaxy, encircling roughly 50% of sun-like stars (Fressin et al., 2013; Petigura et al., 2013; Winn & Fabrycky, 2015; Zhu et al., 2018). That result, coupled with the finding that cold gas giants are relatively rare (Fulton et al., 2021), has shifted the relevant question from “why did extrasolar systems form so differently?” to “why doesn't the Solar System look like extrasolar ones?” (Batygin & Laughlin, 2015; Raymond et al., 2018) In this context, the wealth of information known about the Solar System may appear irrelevant in the quest to understand the formation of exoplanetary systems.

Is the outlook really quite so dire? Deeper investigations have revealed fundamental similarities between the Solar System and extrasolar systems. Notwithstanding some notable exceptions, most extrasolar multiplanet systems have rocky, denser planets interior to gaseous or water-rich ones (Ciardi et al., 2013; Lopez & Fortney, 2013; Millholland & Winn, 2021), and planetary orbits are typically close to circular and coplanar (Fabrycky et al., 2014; He et al., 2020). Mean-motion resonances (MMRs), nonexistent between planets in the Solar System, are rare in the extrasolar realm (Fabrycky et al., 2014). And, growing isotopic evidence points to the existence of multiple disconnected reservoirs of material in the Solar Nebula (Warren, 2011; Budde et al., 2016; Kruijer et al., 2017), inviting comparisons to the rings and gaps observed in the dust of many protoplanetary disks (Andrews et al., 2018).

Thus, it is likely that a common set of physical processes shaped both the Solar and extrasolar systems, though the outcome of planet formation in them was certainly very different. Indeed, the synthesis of the two datasets is extremely powerful (Kane et al., 2021). Solar System constraints are detailed and stringent, routinely excluding all but the most complex physical models. In contrast, extrasolar systems are enormously diverse and rich, exhibiting the full range of planet formation outcomes, even if our particular knowledge of each system or planet is far more limited. Physical processes invoked to explain the peculiarities of exoplanets may be directly testable in the Solar System or its constituent satellite systems. Likewise, almost any scenario that occurred in the Solar System should have an extrasolar analog.

This thesis investigates the assembly and evolution of compact multiplanet systems. Key physical mechanisms like planet-disk interactions, tidal dissipation, mean-motion resonant interactions, and dynamical instability combine in complex ways to generate a wide variety of outcomes. Each of these processes was first identified in the context of the Solar System but has found new importance in the picture of extrasolar system formation, leaving distinct fingerprints on the resulting system architectures.

1.1 Relevant Physical Effects

In this section I give a brief overview of the physical origin and typical properties of four of these effects, all of which appear multiple times in the following chapters.

Planet-disk interaction

Planets that are embedded in a gaseous disk deform the disk, and in turn the deformed disk back-reacts on the planets and modifies their orbits. Broadly, we can distinguish two regimes of planet-disk interaction (Paardekooper et al., 2023; Ward, 1997): one in which the planet is only a perturbation to the disk (Type I), and one in which the planet significantly affects the disk structure (Type II). For the relatively low-mass planets studied in this thesis, the Type I regime is most applicable except possibly at extremely low nebular viscosities.

The primary impact of a planet is to raise wakes in the disk (i.e., density perturbations) interior and exterior to the planet at Lindblad resonances (Goldreich & Tremaine, 1979). The interior and exterior wakes exert a positive and negative torque on the planet, respectively. In general, the two torques do not cancel perfectly and the semi-major axis of the planet evolves; in other words, the planet *migrates*. The rate of Type I migration depends on the exact types of torques considered and the local disk structure but, in typical conditions, disk torques carry planets towards the star

(Ward, 1986; Papaloizou & Larwood, 2000; Tanaka et al., 2002). At face value, Type I migration is extremely rapid: timescales are as short as 10,000 yr for a super-Earth planet at 1AU in a typical disk. However, many effects (in particular, steep gradients in disk properties) can act to slow or reverse migration (Masset et al., 2006; Paardekooper et al., 2010).

Waves raised by the planet also act to reduce ('damp') its eccentricity and inclination (Goldreich & Tremaine, 1980). The timescales of these are well-understood, and are typically faster than the migration timescale by two to three orders of magnitude (Papaloizou & Larwood, 2000; Tanaka & Ward, 2004). Rapid damping is a natural explanation for the predominantly circular and coplanar orbits of planets and also plays a key role in capture into mean-motion resonance, as discussed below.

Type I migration and damping have never been observed directly, although an analogous process may be responsible for the orbital evolution of the so-called "propellers" in Saturn's rings (Crida et al., 2010).

Tidal dissipation

The most familiar example of tidal effects is of course the tides of Earth's oceans raised by the Moon. The gravitational field of the Moon acts as a periodic forcing and drives corresponding oscillations at the surface of the Earth (Murray & Dermott, 1999). Importantly, the global flow of water is not frictionless and as a result Earth's tidal bulge points to a spot slightly ahead of the angular position of the Moon. Angular momentum is transferred from the Earth's rotation to the Moon's orbit, leading to gradual slowing of Earth's rotation (i.e., lengthening of the day) and expansion of the Moon's orbit.[1]

When the dissipating body rotates at the same speed as the tidal perturber, tides conserve orbital angular momentum but continue to transfer energy from the orbit (by reducing its eccentricity) into thermal energy (Goldreich & Soter, 1966). This effect is responsible for the extreme volcanic activity of Io (Peale et al., 1979) and existence of subsurface oceans on several Solar System satellites (Thomas et al., 2016). It is also likely important for close-in extrasolar planets that are tidally locked to their host star. Though typically too slow to observe in real time, tidal dissipation can be probed indirectly by its impact on planetary orbits and has been invoked to explain several unexpected trends in the exoplanet population (Lithwick & Wu, 2012; Lee et al., 2013; Millholland, 2019).

---

[1] The infamous 'leap seconds' added every few years are a consequence of the former effect, and the latter is measured directly by way of reflectors placed on the Moon by Apollo astronauts.

Tidal dissipation scales very steeply with orbital radius and hence is only relevant for the closest planets and satellites. Non-synchronous rotation can dramatically increase the strength of dissipation, a fact exploited in Chapters 4 and 7.

Mean-motion resonance

Gravitational interactions between planets can be enhanced by certain orbital configurations. The most important case is when the ratio of orbital periods of two planets is approximately the ratio of small integers, e.g., 2:1 or 5:3. In such an arrangement, the planets are said to be in mean-motion resonance, and gravitational kicks at planet conjunctions constructively combine to exchange energy and angular momentum periodically between the planets' orbits (Murray & Dermott, 1999). The resulting changes in orbital elements have been studied for over two centuries for the first known resonant system, the Galilean moons (Laplace, 1799; Sinclair, 1975).

One might imagine that, because MMRs exist only in a narrow region of parameter space, they would be uncommon. Nevertheless, they are present in the satellite systems of three of the four Solar System giant planets and also in the Kuiper belt (Pluto, among many other objects, is in resonance with Neptune) (Murray & Dermott, 1999; Brozović et al., 2020). The key is that MMRs are fixed points in the Hamiltonian for planet-planet interactions. Non-conservative forces, such as planet-disk interactions and tidal dissipation, can 'lock' pairs of planets or satellites into MMR, where they remain even if the additional force is removed (Henrard, 1982). The presence of resonant Kuiper belt objects, for instance, is direct evidence that Neptune migrated outwards from its original location (Malhotra, 1995), while a complex web of resonances in the saturnian satellite system indicates that tidal bulges on Saturn lose a bit of their energy to friction much like the Earth's oceans (Ćuk et al., 2016a; Lainey et al., 2017).

Dynamical instability

Not all dynamical histories are tranquil. Planets cannot be arbitrarily packed into orbits around a star because their mutual gravitational interactions will eventually overwhelm the star's gravity. When a system crosses the boundary between stability and instability, the result is a violent disruption of the system: a dynamical instability (Chambers et al., 1996). Planetary orbits intersect and planets are flung around the system, crashing into each other, the star, or are launched out of the system entirely. Eventually, the instability ends and a permanently altered planetary system is left behind. Much evidence suggests that an early instability involving the giant planets (the 'Nice model'[2]) helped shaped the Solar System, including the lack of MMRs between planets which instabilities readily destroy (Tsiganis et al., 2005; Nesvorný & Morbidelli, 2012).

---

[2] 'Nice' as in the city, although the model nicely explains many otherwise unexpected properties of the Solar System.

Studying dynamical instabilities presents some unique challenges. For one, they are strongly non-perturbative, in the sense that one cannot write formulae for slow (relative to the orbital period) evolution of orbital elements, unlike the previous three effects. Instead, they must be modeled numerically with N-body simulations. Secondly, they are chaotic, meaning that the outcome depends sensitively on the initial conditions. The same simulation run on two separate computers may give entirely different results because of differences in treatment of rounding errors. In practical terms, we will never know the pre-instability state of the Solar System giants precisely because the function mapping across the instability is fractal. Repeated simulations, however, can usually recover statistical features of the outcomes, which is sufficient for many uses (Batygin & Brown, 2010).

1.2 Outline

Detailed study of exoplanet observations, coupled with numerical and analytical predictions, can place fundamental constraints on the initial conditions of planet formation and uncover how planetary systems evolved. As the ensuing chapters reveal, a unifying thread across this thesis is the dominance of a single formation pathway. Planet migration, driven by planet-disk interactions or tidal dissipation, leads to capture into mean-motion resonances. In many cases, the resonances are disrupted by dynamical instability. The final systems are perturbed by further planet-disk interaction or tidal dissipation to match their current state. Though not universal, this scenario can explain as diverse a set of systems as the Solar System gas giants, the saturnian satellites, compact resonant chains, and the *Kepler* peas-in-a-pod planets.

Chapter 2 of this thesis provides the big-picture view of this formation pathway and connects widespread dynamical instabilities to demographic patterns found in the *Kepler* planet population. The rearrangement of system architectures following dynamical instabilities comfortably generates the prototypical *Kepler* system: non-resonant planets with similar masses and orbital spacing, on slightly excited orbits.

Chapter 3 looks more closely at the instability boundary for resonant systems. We simplified a prior perturbation theory approach and numerically tested it against a large suite of N-body simulations. In addition to expanding the understanding of dynamical stability to a broader architecture of systems, our framework enables rapid and accurate analysis of the stability of synthetic systems produced during formation simulations and provides a benchmark to test novel mechanisms of triggering instabilities.

Chapters 4–6 consider the alternate track in which the mean-motion resonances formed within the protoplanetary disk are never violently disrupted. This avenue is especially informative because the exact state of the resonances is sensitive to the conditions of the protoplanetary disk and the strength of tidal dissipation within the planets since formation.

Chapter 4 concerns a particular exoplanet system that, while formally non-resonant, has a distinct signature of previous mean-motion resonance. By careful analysis of the orbital dynamics, we show that this configuration can only be reached after strong energy dissipation inside the planets. One candidate for the source of dissipation is obliquity tides; our work is some of the clearest evidence that this form of tidal dissipation actually occurs in low-mass exoplanetary systems.

Chapter 5 expands to the broader set of near-resonant systems that undergo transit timing variations (TTVs). Although TTVs are primarily used to measure planet masses, we show that they constrain dynamical parameters of the resonance that can be directly linked to the protoplanetary disk conditions. We find evidence that these systems were embedded in disks with moderate turbulence that mildly excited their orbits. The degree of turbulence in the inner regions of the protoplanetary disk is currently of considerable theoretical and observational interest, and the state of resonances between planets (or their absence) is a promising method to provide constraints far closer to the star than ALMA can probe.

Chapter 6 is adapted from the discovery paper of TOI-1136, a resonant chain of six planets observed by the TESS mission. Initially, poor TTV coverage of the system made it difficult to determine whether the resonances were actually active. The new insights gained from Chapter 5 allowed us to improve the TTV analysis and confirm that the entire system is precisely locked in a complex web of resonances. Of particular note is the rare second-order 7:5 resonance between planets e and f, which necessitates very gentle migration and capture into resonance. TOI-1136 is the first clear example of the libration of a mean-motion resonance of higher than first order outside the Solar System. This system is an uncommon outcome of planet formation, yet its mere existence provides considerable information on migration rates and the location of an inner edge in the protoplanetary disk.

These processes arise not only in protoplanetary disks but also in different environments and scales. Chapter 7 turns inward to the Solar System and the satellites of Saturn. A strong analogy connects them to extrasolar systems: Saturn takes the role of the host star, satellites of the exoplanets, tidal migration (from dissipation within Saturn) replaces Type I migration, and, in this case, strong eccentricity damping from Hyperion's rapid rotation replaces the damping from planet-disk interactions. The last piece is vital: Hyperion's famed chaotic tumbling protects it from the eccentricity growth generated by the mean-motion resonance with Titan. The orbital dynamics of Hyperion appear simple, but a consistent picture of its history has eluded comprehension until now.

Finally, Chapter 8 presents concluding thoughts and future outlook.

C h a p t e r 2

ARCHITECTURES OF COMPACT SUPER-EARTH SYSTEMS SHAPED BY INSTABILITIES

Goldberg, M. & Batygin, K. (May 2022). “Architectures of Compact Super-Earth Systems Shaped by Instabilities.” In: *The Astronomical Journal* 163, p. 201. ISSN: 0004-6256. DOI: `10.3847/1538-3881/ac5961`.

2.1 Introduction

Over the course of the past two decades, the discovery and characterization of thousands of extrasolar planets by the *Kepler* and TESS missions has shown that planet formation is both highly efficient and suggested that the dominant mode of planet formation is one that produces so-called super-Earths. These planets tend to exist in multiples, and typically have masses a few times that of Earth and orbital periods smaller than $\sim$ 100 days (Howard et al., 2012; Batalha et al., 2013; Fressin et al., 2013; Marcy et al., 2014; Thompson et al., 2018). A remarkable discovery of this expanding census is the physical diversity of the galactic planet sample. Planets vary by several orders of magnitude in radius, mass, and orbital distance and frequently orbit stars not similar to the Sun (Raymond & Morbidelli, 2020). While not fully quantified, the emerging picture suggests the Solar System is an unusual outcome of planet formation because of the presence of Jupiter and lack of a compact system of inner planets (Batygin & Laughlin, 2015; Izidoro et al., 2015; Raymond et al., 2018).

An equally remarkable, but more recent discovery, is that the galactic diversity largely disappears when considering only individual planetary systems. The “peas-in-a-pod” pattern of intra-system uniformity has demonstrated that the dispersion in planet spacing, mass, and radius within individual planetary systems is much smaller than that across the exoplanet population as a whole (Weiss et al., 2018; Millholland et al., 2017; Wang, 2017). In other words, many systems seem to have a characteristic planet mass, radius, and spacing that is representative for a particular star, but differs drastically system-to-system. The physical origin of this uniformity remains unresolved.

A distinct mystery is the origin of the period ratio distribution. Plausible models of super-Earth formation typically include planet-disk interactions that drive inward migration and often lead to capture of the planets into mean-motion resonances (MMRs)—orbital configurations where the period ratios are approximated by nearby integers (Terquem & Papaloizou, 2007). While there is weak clustering of planet just wide of mean-motion resonances, near-resonant planets form a distinct minority in the close-in planet sample (Fabrycky et al., 2014). A rare, but important exception to this rule is the class of resonant chains, such as Kepler-60, Kepler-80, Kepler-223, K2-138, TRAPPIST-1, and TOI-178 (Goździewski et al., 2016; MacDonald et al., 2016; Mills et al., 2016; Christiansen et al., 2018; Luger et al., 2017; Leleu et al., 2021a), as well as a subset of near-resonant systems that show hints of past resonant behavior (Pichierri et al., 2019; Goldberg & Batygin, 2021). Nevertheless, the dominantly non-resonant orbital configurations of short-period planets constitute an important point of tension between theory and observations.

Multiple ideas have been put forth to explain this discrepancy over the last decade and a half. One suggestion is that disk turbulence destabilizes resonances for small planets (Adams et al., 2008; Rein & Papaloizou, 2009; Batygin & Adams, 2017). However, both analytic calculations (Batygin & Adams, 2017) as well as numerical simulations have confirmed that this effect is too small to explain the discrepancy (Izidoro et al., 2017). Likewise, resonant metastability, proposed in Goldreich & Schlichting, 2014, operates in region of parameter space that does not encompass most of the sample. As a whole, these models have failed to provide a complete explanation for the data, and detailed hydrodynamic simulations (e.g., Cresswell & Nelson, 2008; Ataiee & Kley, 2020, and the references therein) find that formation of compact resonant chains is a common outcome of disk-driven orbital evolution. Given this tension between theoretical expectations and observational ground-truths, physical processes must either prevent the formation of resonances in the first place, or disrupt them later.

The recently-proposed "breaking the chains" scenario of (Izidoro et al., 2017) argues for the latter alternative. In this model, resonances *are* in fact routinely established in nascent exoplanetary systems during orbital migration. Subsequently, the gaseous disk, which had provided eccentricity damping, dissipates, and the planetary system relaxes through the onset of dynamical instability and collisions. Several aspects of the exoplanetary sample are consistent with this hypothesis. First, planetary systems lie close to the margin of stability on Gyr timescales, suggesting that they experienced dynamical sculpting, i.e., encountering instabilities until becoming stable (Pu & Wu, 2015). Second, widespread instabilities reproduce the shape and slope of the observed period-ratio distribution if $\sim 90\%$ of systems experience such a disruption in their lifetime (Izidoro et al., 2017; Izidoro et al., 2021). As successful as this scenario is in explaining many constraints of the observed planetary sample, an important outstanding problem remains. Naively, consolidation of planets during collisions could destroy the delicate intra-system uniformity that is observed. Furthermore, orbital eccentricities are excited by planet-planet scattering, but damped by collisions (Matsumoto & Kokubo, 2017; Esteves et al., 2020; Poon et al., 2020) and it remains unclear whether measured low eccentricities of planets in compact systems are consistent with typical post-instability orbits (Hadden & Lithwick, 2014; Mills et al., 2019; Yee et al., 2021).

System	# planets	$\overline{m}/(M_\star/M_\odot)$ ($\mathrm{M}_\oplus$)	$\sigma_m/\overline{m}$	Resonances present	Source of mass measurements
Kepler-60	3	3.91	0.18	4:3, 5:4	Jontof-Hutter et al., 2016
TRAPPIST-1	7	11.51	0.46	5:3, 8:5, 3:2, 4:3	Agol et al., 2021
Kepler-223	4	5.63	0.31	3:2, 4:3	Mills et al., 2016
Kepler-80	6	8.43	0.23	3:2, 4:3	MacDonald et al., 2016
TOI-178	6	6.41	0.53	2:1, 5:3, 3:2	Leleu et al., 2021a
K2-138	5	7.06	0.62	3:2	Christiansen et al., 2018

Table 2.1: Basic properties of the six well-characterized resonant chains with sub-Jovian planets. Note that only 4 planets in Kepler-80 have measured masses, and Kepler-80 f and K2-138 g have been excluded because they are decoupled from the resonant dynamics.

The remainder of this chapter details our investigation into the compatibility of the observed peas-in-a-pod correlations with the instability model. We create physically motivated models of pre-instability super-Earth/sub-Neptune systems, trigger instabilities, and compute statistical properties of their post-instability architectures. We then compare them to observed results. In Section 2.2, we describe how we construct physically realistic initial conditions of resonant systems informed by real, stable, resonant chain systems. In Section 2.3, we describe how we trigger dynamical instabilities and track evolution of the systems through collisions and mergers. In Section 2.4 we present the results of our suite of simulations and their degree of consistency with observed data. We summarize and discuss our results in Section 2.5.

2.2 Initial Conditions

The first step in modeling the instability scenario is to construct a broad library of initial conditions. In the framework of this model, the observed resonant chains are the small fraction of systems that did not undergo episodes of post-nebular planet-planet scattering. Therefore, we construct our initial conditions informed by this observed subsample. By virtue of being near MMR, these systems lend themselves to precise mass determinations through transit timing variations (Lithwick et al., 2012), and are well-studied with spectroscopic surveys (e.g., Petigura et al., 2017).

To construct multi-resonant systems through convergent orbital migration, we select the number of planets N, average planet mass $\overline{m}$, planet relative standard deviation $\sigma_m/\overline{m}$, and initial resonant indices $p : q$. We take $N = 11$, approximately twice the inferred true average multiplicity (Zink et al., 2019). To cover a similar distribution of masses as the observed resonant chains (Table 2.1), we pick values of $\overline{m} = 10.0$ for a higher-mass sample (runs 1-8) and $\overline{m} = 1.5$ for a lower-mass sample (run 9), typically selecting the highest mass for which the resonances can be formed without triggering an instability in the presence of the disk. Initial mass dispersions $\sigma_m/\overline{m}$ are in the range 0 to 0.5. Each simulation draws masses from a normal distribution with mean $\overline{m}$ and variance σ_m^2. While real resonant chain systems, such as the ones in Fig 2.1, contain a variety of first-, second-, and third-order resonances, our constructed systems must be more compact than the observed

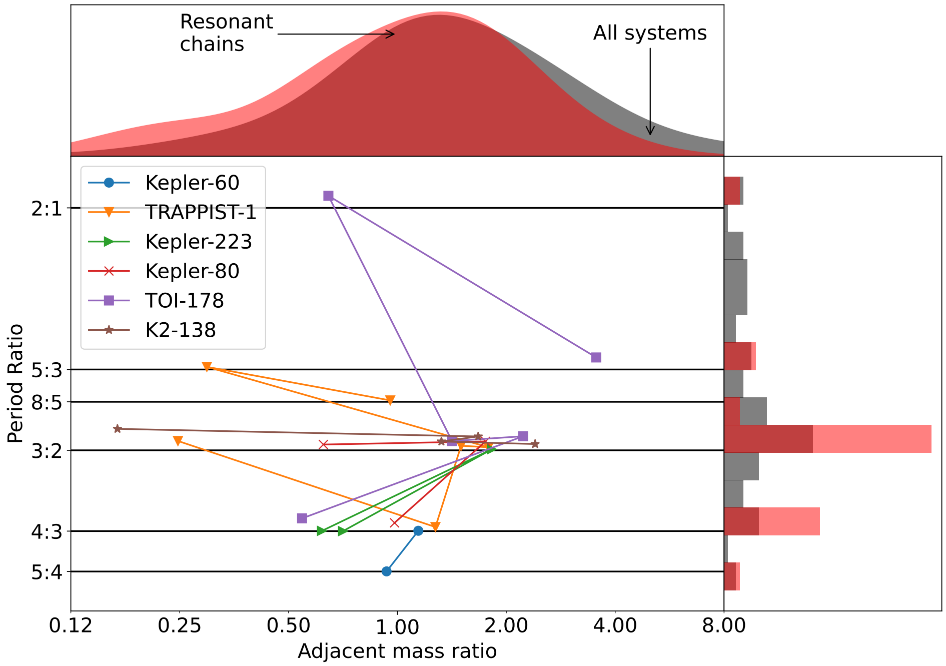

Figure 2.1: Mass ratios and orbital period ratios of five well-characterized resonant chains. Center: colored points represent adjacent pairs of planets and are placed according to mass and orbital period ratio computed from outside-in. Colored lines connect adjacent pairs in the same system, and horizontal black lines mark orbital resonances. Adjacent pairs missing at least one measured mass were discarded. Top: kernel density estimates of the distribution of mass ratio for the five resonant chains (red) versus all sub-Jovian systems (gray). Right: histogram of period ratios of adjacent planets with the same color scheme as the top panel. Overall, resonant chains exhibit tighter clustering in both period ratios and mass ratios than the overall sample of sub-Jovian exoplanets.

resonant systems in order to go unstable. Therefore, we pick resonances with smaller period ratios, specifically 4:3 for the high-mass sample and 5:4 for the low-mass sample. These initial conditions are summarized in Table 2.4.

We simulate resonant chain formation and subsequent evolution with the `mercurius` integrator from the `rebound` gravitational dynamics software package, with timesteps lower than 1/15 the innermost orbital period (Rein et al., 2019). Planets are placed on circular, coplanar orbits around an $M_\star = 1 M_\odot$ star, with the semi-major axis of the innermost planet set to 0.1 AU and period ratios just wide of the intended resonance. We then activate convergent migration with eccentricity damping, implemented within `reboundx` (Tamayo et al., 2020b), until the planets have entered the intended resonance ($\lesssim 10^5$ yr). The details of the migration and damping timescales are provided in Appendix 2.6. In practice, planets in the lower-mass simulations entered either the 5:4 or the 6:5 resonance. Then, we remove semi-major axis and eccentricity damping exponentially over a timescale of 10^3 yr. We have checked that increasing these timescales does not meaningfully alter our results. The final pre-instability systems contain many librating resonance angles and the orbital orbital eccentricities are typically ~ 0.05 or smaller. At this point we rescale the systems so that the inner planet has semi-major axis 0.1AU, which corresponds to a drop-off in prevalence of super-Earths (Petigura et al., 2013).

2.3 Instabilities

The instability and collision-driven model necessitates a source of instabilities. To this end, Izidoro et al., 2017 and Izidoro et al., 2021 produce post-disk-dissipation planetary systems that are too tightly packed to remain stable on $\sim$ Gyr timescale, and hence will undergo an intrinsic dynamical instability triggered purely by gravitational dynamics. However, there are many other possible instability mechanisms due to extrinsic, i.e., astrophysical, factors. Spalding & Batygin, 2016 and Spalding et al., 2018 demonstrate that an oblique and initially rapidly-rotating star can excite mutual inclinations, leading to secular resonances that drive instabilities (see also Schultz et al., 2021). Matsumoto & Ogihara, 2020 show that mass loss in the systems (of order $\sim 10\%$ in planetary mass or $\sim 1\%$ in stellar mass) can also induce instabilities and break resonant chains. As a whole, if instabilities occur frequently, they unavoidably play a major role in modifying orbits and shaping the architectures of exoplanetary systems (Ogihara & Ida, 2009).

Our intention is not to test various instability mechanisms; rather, we want to investigate the consequences of collisions and mergers. Additionally, the instability mechanism is not believed to dramatically affect the post-instability configuration itself (Nesvorný & Morbidelli, 2012). Therefore, we adopt the mechanism of Matsumoto & Ogihara, 2020: planet masses are exponentially decreased with an evolution timescale of 1 Myr until they reach 90% of their original mass. This suffices to trigger instabilities in many cases without qualitatively changing the system and does not require overly long integrations. We evolve the initially resonant systems for a further 5 Myr monitoring for collisions. When one is detected, we record the colliding pair's masses and relative velocities and then replace them with a single planet whose mass and linear momentum are the sum of the mass and linear momentum of the colliders. While this assumes collisions are perfect mergers, we verify this assumption below, in agreement with the results of Poon et al., 2020 and Esteves et al., 2022. To produce a statistically useful sample, we repeat the collision phase 50 times, starting from the mass reduction, but use a mass loss timescale that is randomly shifted by $\sim 1\%$ from 1 Myr. Because of the chaotic dynamics of planet-planet scattering, each run produces a different set of collisions and it is possible to compute distributions of final parameters (Figure 2.2).

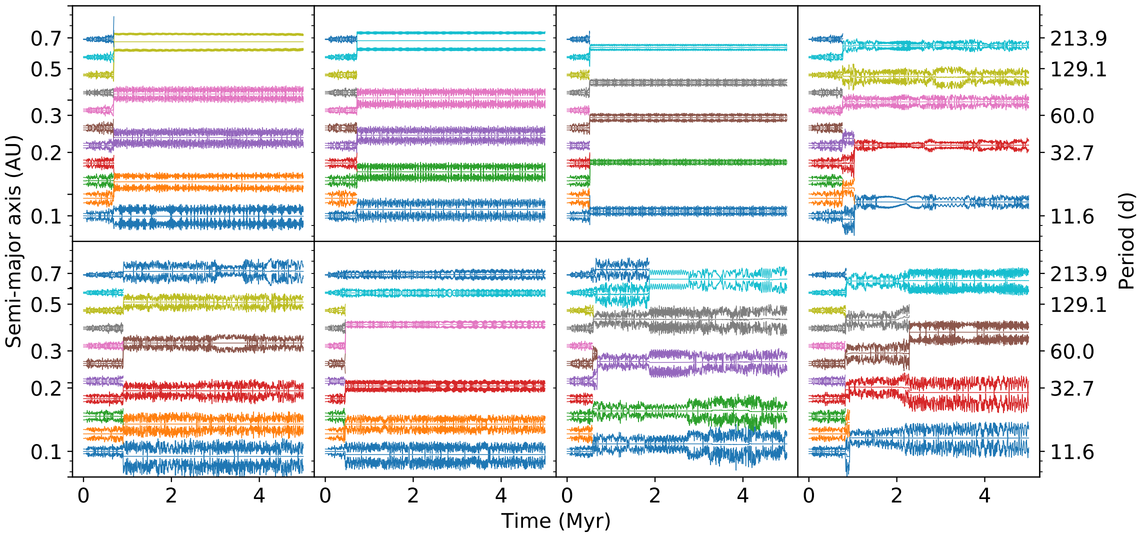

Figure 2.2: Eight collisional outcomes for the same initial system with $N = 11$, $\overline{m} = 8.6M_\oplus$, initial resonance 4:3, and initial mass dispersion $\mathcal{D} \approx 0.1$. For each planet, the semi-major axis a, pericenter distance $a(1-e)$, and apocenter distance $a(1+e)$ are plotted in the same color. When two planets collide, the traces retain the color of the inner planet. Instability-driven evolution leads to wider orbital spacing, while retaining a degree of mass-uniformity that is compatible with the data.

2.4 Results

To evaluate whether collisions are consistent with the architecture of observed planetary systems, we compute statistical measures used in previous works to characterize the mass and spacing uniformity of our synthetic systems. To construct the sample of observed systems with which to compare our synthetic ones, we select all systems from the Exoplanet Archive[1] with at least 3 planets that do not contain planets more massive than $30\mathrm{M}_\oplus$. The latter constraint is chosen because mass uniformity vanishes in systems with giant planets (Wang, 2017). The six resonant chains in Table 2.1 and Figure 2.1 are a subset of this sample.

Intra-system Uniformity

Although the works that identified the intra-system uniformity pattern each used different statistics to identify the uniformity (Millholland et al., 2017; Wang, 2017; Weiss et al., 2018), for definitiveness, we adopt a modified version of the mass uniformity metrics from Wang, 2017. Specifically, we normalize by the average planet mass in a system, so that larger planets do not appear less uniform, and by the total number of systems, so that the metric does not depend on the number of systems.

---

[1] `exoplanetarchive.ipac.caltech.edu`

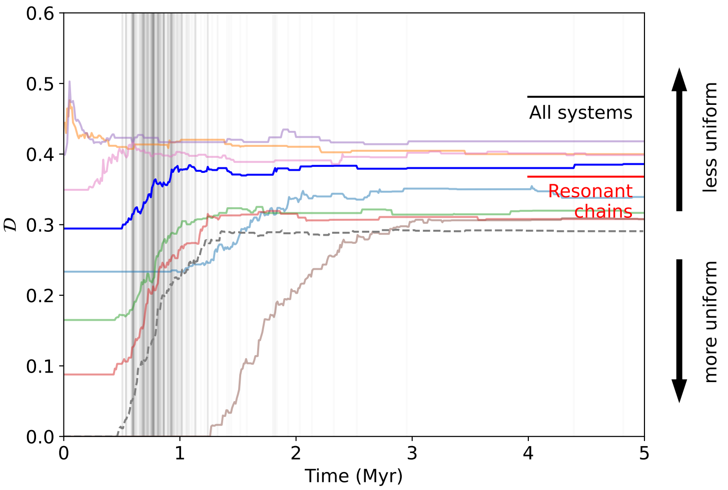

Figure 2.3: Runs of 50 integrations of nearly the same initial conditions, with $N = 11$, $\overline{m} \sim 10M_\oplus$, and initial resonance 4:3, but differing initial mass dispersion $\mathcal{D}$. The dashed line marks the evolution for run 9, which has different initial conditions (see Table 2.4). The red and black horizontal lines represent $\mathcal{D}$ for the resonant chains from Section 2.2 and all systems, respectively. For the run starting around $\mathcal{D} \approx 0.35$, plotted darker in blue, translucent vertical lines indicate the time of a collision, which triggers a change in $\mathcal{D}$.

Hence, we define

$$\mathcal{D} = \frac{1}{N_{\rm sys}} \sum_{i=1}^{N_{\rm sys}} \sqrt{\frac{\sum_{j=1}^{N_{\rm pl}} (m_j - \overline{m}_i)^2}{\overline{m}_i^2 (N_{\rm pl} - 1)}} = \frac{1}{N_{\rm sys}} \sum_{i=1}^{N_{\rm sys}} \frac{\sigma_m}{\overline{m}_i}. \tag{2.1}$$

Here, the inner sum is taken over a single system: $N_{\rm pl}$ is the number of planets in a system and m_j is the individual mass of the j-th planet. The outer sum is taken over all systems: $N_{\rm sys}$ is the total number of systems considered and $\overline{m}_i = \sum_{j=1}^{N_{\rm pl}} m_j / N_{\rm pl}$ is the average planet mass in a system. The metric $\mathcal{D}$ is dimensionless, and can be understood as the average relative standard deviation in mass. It is also closely related to the mass partitioning Q defined in Gilbert & Fabrycky, 2020, differing by a square root and a factor of $N_{\rm pl}$. A similar expression for uniformity in radius can be defined, but we do not explicitly use it because radii in our simulations are computed directly from the mass and assume a constant density. The uniformity metric for our multiplanet sample is $\mathcal{D} = 0.48$, and $\mathcal{D} = 0.37$ for the six resonant chains. Hence, the resonant chains are somewhat more uniform in mass than the full population (see also Figure 2.1).

As collisions combine planets, $\mathcal{D}$ varies significantly, and its final value depends strongly on which planets collide. Accordingly, we take the average of $\mathcal{D}$ across the 50 runs and track it as a function of time. The evolution of the average $\mathcal{D}$ for the high-mass sample is shown in Figure 2.3. During the 5 Myr integration, the number and masses of planets change as planets collide and merge or,

Run	initial $\overline{m}$ ($M_\oplus$)	final $\overline{m}$ ($M_\oplus$)	initial resonance	initial $\mathcal{D}$	final $\mathcal{D}$	final r	final $\overline{\Delta}$	final f
1	8.0	16.6	4:3	0.00	0.31	0.34	10.2	0.46
2	8.6	17.1	4:3	0.09	0.31	0.44	11.6	0.43
3	9.1	18.2	4:3	0.16	0.32	0.57	11.4	0.43
4	9.6	20.2	4:3	0.23	0.34	0.36	10.1	0.46
5	10.2	21.9	4:3	0.29	0.39	0.46	11.4	0.41
6	10.7	23.7	4:3	0.35	0.41	0.53	12.1	0.43
7	11.3	24.7	4:3	0.40	0.42	0.36	12.8	0.39
8	11.8	26.5	4:3	0.44	0.40	0.46	13.1	0.37
9	1.50	2.64	5:4, 6:5	0.00	0.30	0.44	16.5	0.46

Table 2.2: Key system architecture parameters in our suite of simulations with $N = 11$.

rarely, are ejected from the system. For more uniform initial conditions $\mathcal{D}$ generally increases, and settles to a value of $\sim 0.3 - 0.4$. This lies slightly above the observed $\mathcal{D}$ of 0.37 for resonant chains and below 0.48 for all systems with $M_{\max} < 30M_\oplus$, meaning that even after dynamical relaxation and the associated collisions, this set of post-instability systems is marginally more uniform than the overall Kepler sample.

Surprisingly, the final value of $\mathcal{D}$ does not strongly depend on the initial mass distribution. We ran 8 suites of simulations with $\overline{m} \sim 10M_\oplus$, 4:3 resonances, and initial $\mathcal{D}$ varying from 0 to 0.45. The results, shown as translucent lines in Figure 2.3, indicate that the cascade of collisions does not necessarily increase $\mathcal{D}$, but brings it within a range $0.3 - 0.4$. This suggests that an arbitrary choice of initial $\mathcal{D}$ does not significantly bias the results.

Hill spacing and period uniformity

A straightforward consequence of an instability phase is that the post-instability system must be stable on $\sim$ Gyr timescales. This manifests as an increase in the Hill spacing. First, we define the mutual Hill radius as

$$R_{Hj} = \left(\frac{m_{j+1} + m_j}{3M_\star}\right)^{1/3} \frac{a_{j+1} + a_j}{2}, \tag{2.2}$$

which represents a characteristic length scale for gravitational interactions between planets. Then, the Hill spacing is

$$\Delta_j = \frac{a_{j+1} - a_j}{R_{Hj}}, \tag{2.3}$$

and the average Hill spacing $\overline{\Delta}$ is simply the average of Δ_j in a system. The lifetime of a multiplanet system strongly depends on $\overline{\Delta}$ (Chambers et al., 1996), so collisions will proceed until $\overline{\Delta}$ grows and the system relaxes. The final values of $\overline{\Delta}$ in Table 2.4 are $10 - 13$ for the high-mass sample, comparable to observed compact multiplanet systems (Pu & Wu, 2015).

Because Equations 2.2 and 2.3 depend exclusively on planet mass and semi-major axis, intra-system uniformity in mass and Hill spacing directly implies uniformity in semi-major axis ratio

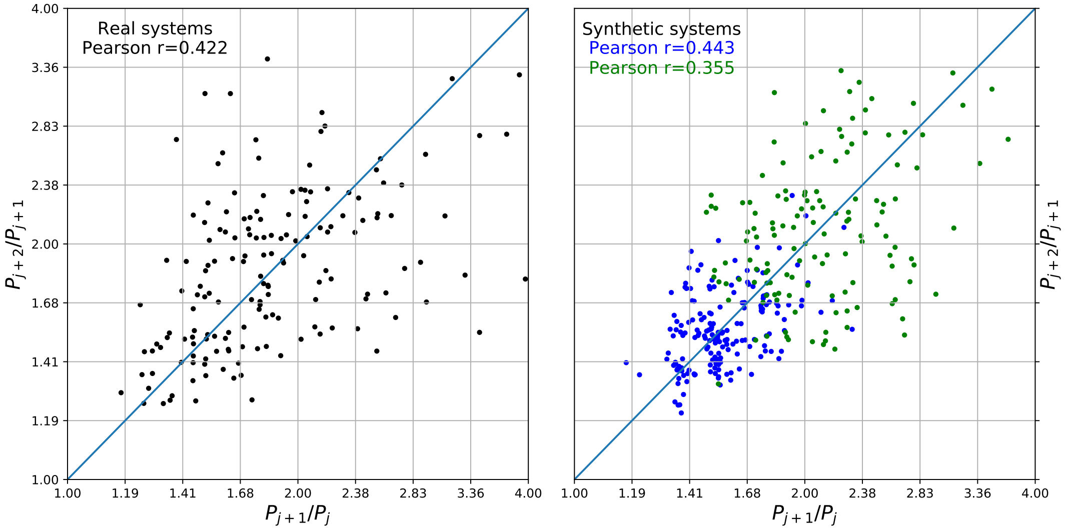

Figure 2.4: Period ratios of outer planet pairs and inner planet pairs for the well-characterized systems in Weiss et al., 2018 (left) and synthetic systems (right). In the right panel, blue and green dots correspond to the low-mass and high-mass samples, respectively. The Pearson r correlation between the orbital period ratios is statistically significant ($p < 10^{-4}$) in both cases.

and therefore period spacing. To quantify this, we adopt the metric from Weiss et al., 2018, which is to compute the Pearson r correlation coefficient of period ratios of adjacent pairs of planets, i.e., P_{i+2}/P_{i+1} and P_{i+1}/P_i. With their sample of well-characterized planets, they find a correlation of 0.46 and high statistical significance. Our simulations broadly reproduce this in the high- and low-mass simulations this with an average correlation of $\overline{r} = 0.44$ and some scatter (Table 2.4, Figure 2.4).

Period ratio distribution

The principal difference between our high-mass and low-mass systems is the period ratio distribution. Higher-mass systems must be more widely spaced to ensure stability. The high-mass sample lacks almost any planet pairs with period ratio less than 1.5 but otherwise matches the slope of the cumulative distribution. On the other hand, the low-mass sample misses period ratios above 2.0. This suggests that we should combine the samples in a particular proportion to produce an optimal match to the data. A similar approach was taken in Izidoro et al., 2017; Izidoro et al., 2021. We create the blended populations by choosing a fraction of systems to draw from the low-mass sample (run 9) while drawing the remainder from run 5 of the high-mass sample, which has average mass and initial dispersion similar to the resonant chains. Figure 2.5 shows the results of this exercise. A mixture of 25% of systems taken from the low-mass sample and 75% from the high-mass one fits

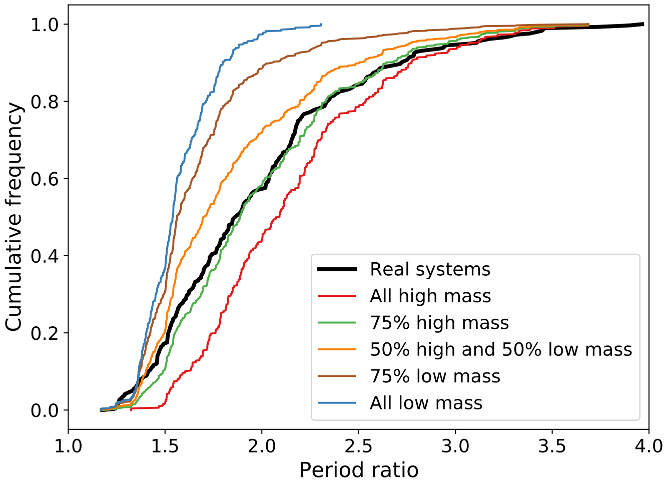

Figure 2.5: Cumulative frequency of period ratio for the post-instability synthetic systems (colored lines) and real systems (black line). Blended samples are constructed by mixing the two populations of low- and high-mass planets in the listed fractions.

the period ratio distribution best. We emphasize that these numbers are not to be taken literally—super-Earth planetary systems do not form in these two discrete mass ranges—but we highlight that a simple model of two populations reproduces many aspects of the observed sample with surprising ease. Because the uniformity observed in super-Earth systems is confined to planets that orbit a common star, it is not suppressed by combining a diverse set of systems. Accordingly, this merged sample has a period ratio correlation of $r = 0.56$ and intra-system mass dispersion $\mathcal{D} = 0.33$.

Collisions

While our simulations treat impacts as perfect mergers, the outcomes of planetary-scale collisions in general depend strongly on the speed and angle of the encounter as well as the mass ratio of the colliders (Stewart & Leinhardt, 2012). Consider a projectile of mass m' and radius s' that collides with a target of mass m and radius s at a relative velocity V_{imp} and impact angle θ. Only a fraction of the projectile interacts with the target, specifically the interacting mass

$$m'_{\text{interact}} = \frac{3s'l^2 - l^3}{4s'^3} m' \tag{2.4}$$

where l is the projected length

$$l = (s + s')\,(1 - \sin\theta) \tag{2.5}$$

(Leinhardt & Stewart, 2012). Numerical simulations have shown that collisions are nearly perfect mergers if the collisional speed does not exceed the escape velocity of the newly formed planet,

$$V_{\text{esc}} = \sqrt{2G(m + m'_{\text{interact}})/S} \tag{2.6}$$

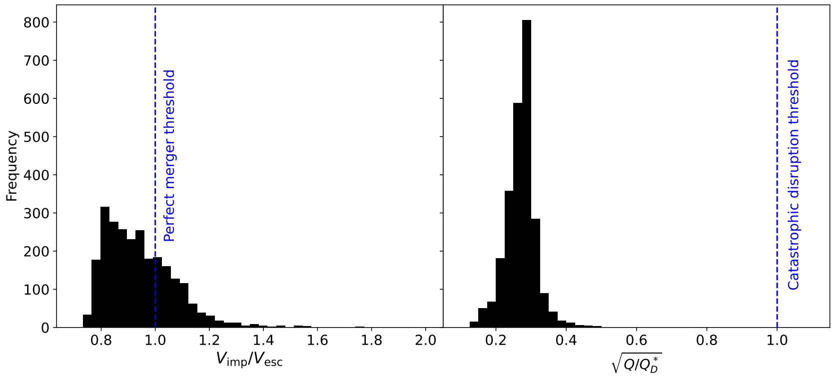

Figure 2.6: Collisional energetics of impacts in our simulations. Left panel: the distribution of the relative speed just before a collision, scaled by the escape velocity of the new planet. Collisions with $V_{\rm imp}/V_{\rm esc} < 1$ are expected to be perfect mergers. One event with $V_{\rm imp}/V_{\rm esc} \approx 12.4$ has been omitted for clarity. Right panel: the distribution of specific collision energy to the energy required for catastrophic disruption. The event omitted from the left panel lies just below $Q/Q_D^* = 1$.

where G is the gravitational constant and $S = (s^3 + s'^3)^{1/3}$ is the radius of the new planet, assuming constant density (Stewart & Leinhardt, 2012).

The left panel of Figure 2.6 shows the ratio of collision speed to escape velocity for the 2529 collisions in our simulations. While all collisions occur above $0.7V_{\rm esc}$ due to mutual gravitation of the planets as they come together in the collision, approximately 70% of collisions occur below the final escape velocity. Of the $\sim$ 30% of collisions with $V_{\rm imp} > V_{\rm esc}$, most are just above the threshold for merging except for one collision with $V_{\rm imp} \approx 12V_{\rm esc}$, not shown in the histogram. This unusual event likely resulted from a retrograde orbit formed during the scattering process.

Nevertheless, even collisions above the escape velocity do not necessarily disperse material completely. Specifically, for the projectile to catastrophically disrupt and unbind the target of mass into two or more pieces, the specific impact energy Q must exceed the catastrophic disruption threshold Q_D^*, where

$$Q = \frac{m' V_{\rm imp}^2}{2(m + m')} \tag{2.7}$$

and, in the gravity dominated regime,

$$Q_D^* = q_g \rho_m \left(\frac{s}{1\rm cm}\right)^b \tag{2.8}$$

where, for high-speed collisions of basalt, $q_g \approx 0.5$ erg cm^{3}g^{-2}, $\rho_m \approx 3$ g cm^{-3} is the density, and $b = 1.36$ (Armitage, 2020). The right panel of Figure 2.6 shows the ratio $\sqrt{Q/Q_D^*}$ for the same collisions. All events lie below the catastrophic disruption threshold, including the exceptional event referred to above, which has $\sqrt{Q/Q_D^*} = 0.98$.

These results are broadly consistent with those of Poon et al., 2020. They use a different definition of escape velocity that is, in practice, always smaller than Equation 2.6, but nonetheless find that the majority of collisions occur only slightly above the escape velocity of the merged planet. They show furthermore that typical collisions do not dramatically change the ice fraction, but can strip gaseous envelopes. Similarly, Esteves et al., 2022 find that, while fragmentation during collisions can occur, the total amount of material that is stripped is small and has little effect on the dynamics.

2.5 Discussion

This work investigates the implications of dynamical instabilities and collisions on compact multi-planet system architectures. Within the context of this picture, we argue that the currently observed sub-sample of multi-resonant chains constitutes an adequate set of initial conditions for the instability model, and from this we conduct a suite of simulations to quantify the outcome of breaking the resonant locks. By and large, our calculations show that intra-system uniformity in mass, seen in resonant chains, is preserved after collisions and mergers in a way that is consistent with observations. Furthermore, as the planetary orbits are dynamically sculpted, a smooth period ratio distribution and period spacing uniformity naturally arise. Finally, we demonstrate that typical collisions are slow and unlikely to disrupt a large fraction of the planets.

An intriguing feature exhibited by the observational data is that the degree of orbital packing correlates inversely with the average planetary mass. That is to say, low-mass planets occupy more compact orbital architectures than their more massive counterparts (Weiss et al., 2022). This feature is distinct from a simple requirement of uniformity and long-term dynamical stability. For example, the Titius-Bode law is reflective of a period uniformity in the Solar System, despite a lack of mass uniformity (Hayes & Tremaine, 1998). The fact that a correlation which links mass and spacing exists hints that beyond any disk-driven processes that may regulate the terminal masses of forming planets (e.g., Lambrechts et al., 2014; Ormel, 2017), the planetary masses themselves play a role in regulating the terminal spacings. Early dynamical evolution driven by transient instabilities provides the most natural mechanism to produce this feature in the data.

A possible drawback of the instability model is the degree of dynamical heating from violent gravitational interactions. That is, orbit crossings entail growth in eccentricities and mutual inclinations (Tremaine, 2015). Figure 2.7 shows the distributions of orbital eccentricities in our simulations. Post-instability planets have eccentricities that approximately follow a Rayleigh distribution with scale parameter σ_e that depends on the initial mass. For the high-mass sample, $\sigma_e \approx 0.05$, as has been seen in previous work (Dawson et al., 2016; Izidoro et al., 2017). For the low-mass sample, $\sigma_e \approx 0.02$. Median system eccentricities are higher for higher intrinsic multiplicities, in line with the expectation from the maximum-AMD model of He et al., 2020.

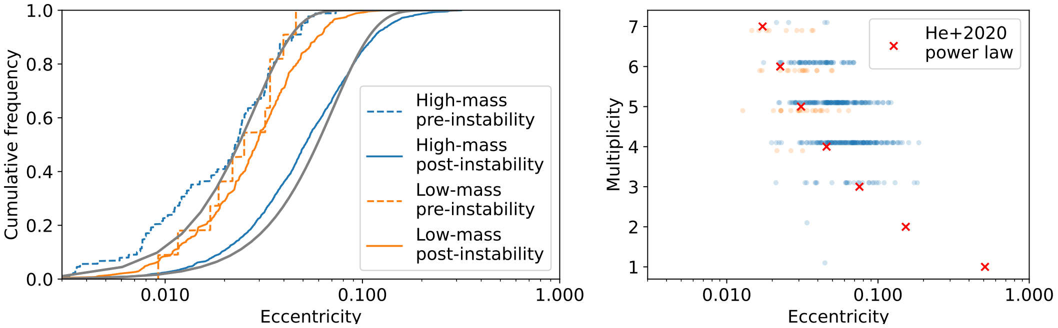

Figure 2.7: Eccentricity distributions for our suite of simulations. Left panel: cumulative frequency of planet eccentricity for pre- and post-instability planets for the high-mass sample (runs 1-8) and the low-mass sample (run 9). Thicker gray lines represent Rayleigh distributions with scale factors 0.02 and 0.05. Right panel: median system eccentricity as a function of multiplicity, with the same colors as the left panel. Multiplicities are shifted slightly for clarity. Red crosses mark the power law (Equation 51) from He et al., 2020.

Eccentricity measurements of observed planets typically come from one of two methods. The first is a forward modeling approach that treats eccentricities and mutual inclinations as underlying distributions, along with other system parameters. Synthetic systems are then compared to observations; in particular, transit durations are the primary constraint on eccentricity (Ford et al., 2008). Such studies tend to recover scale parameters of ~ 0.05 Xie et al., 2016; Van Eylen et al., 2019; Mills et al., 2019; He et al., 2020. More recent work has suggested evidence for a multiplicity dependence on the distribution parameters, although that requires additional assumptions on system architecture as well as observational constraints from transit duration variations to confirm (He et al., 2020; Millholland et al., 2021).

The second method is through transit timing variations (TTVs), which, while typically used to measure masses, also depend strongly on eccentricity (Agol et al., 2005). Statistical studies with this technique recover smaller eccentricities, with scale factor ~ 0.02 (Hadden & Lithwick, 2014). Furthermore, TTV systems have been shown to be significantly more circular than required for stability (Yee et al., 2021). However, two important biases limit the conclusions that can be drawn from TTV-derived eccentricities. Planet mass and eccentricity are degenerate in most cases, and hence eccentricity distributions depend on the choice of mass prior (Hadden & Lithwick, 2017). Additionally, TTV systems are a non-uniform sample of the multiplanet system population that preferentially selects planet pairs that are close to resonance and coplanar. In the instability scenario, these may be the systems that remained stable and did not experience growth in eccentricity. Or, if they did encounter an instability, they may have experienced a smaller degree of scattering that left them unusually coplanar and circular (Esteves et al., 2020).

For simplicity, our simulations were confined to the plane. In reality, planets are expected to exit the protoplanetary disk with inclinations of $\sim 0.1^{\circ}$. To test the impact of small but non-zero inclinations, we repeated runs 1-5 starting from the mass loss step but gave each planet an inclination drawn uniformly from $[0^{\circ}, 0.1^{\circ}]$. Because first-order resonances do not depend on inclination, the resonant angles continued to librate until the instability was triggered. The final intra-system uniformity in masses and period ratios was consistent with the results of the planar simulations. However, because in three dimensions orbital eccentricities can grow larger without guaranteeing a collision, collisional velocities were $\sim$ 20% higher and the final eccentricity distribution had a longer tail past $e \sim 0.1$. These results are consistent with the trends seen by Matsumoto & Kokubo, 2017. Nevertheless, this set of inclined simulations likely overestimates eccentricities somewhat because the final planets have $\sim$ 30% larger masses than in the coplanar simulations, which are themselves larger than typical super-Earth masses.

Even if eccentricities from post-instability systems are higher than those that are observed, this is not evidence against the instability model. Planet pairs just wide of mean-motion resonances require a mechanism that damps eccentricity after disk dissipation and this mechanism could operate in non-resonant systems as well (Lithwick & Wu, 2012; Batygin & Morbidelli, 2013). Future work should determine to what extent tides or planetesimal scattering can reproduce the observed eccentricity distribution and whether such damping leaves observational signatures that can constrain post-nebular evolution.

Beyond consideration of the angular momentum deficit itself, collisions may effect a preference for ordering in systems by mass (Ogihara et al., 2015). Our initial conditions have no ordering as planet masses are chosen randomly. However, in real systems, planets tend to increase in mass and radius as orbital radius increases (Millholland et al., 2017; Weiss et al., 2018). To quantify any ordering in mass, we adapt the metric from Weiss et al., 2018 that considers the fraction f of planet pairs in which the outer planet is more massive; unordered systems have $f = 0.5$. As collisions proceed, mass tends to settle close to the star; by the end of our simulations, $40 - 50\%$ of planet pairs have a more massive outer planet. This prediction of the model does not match observed trends wherein 65% of planet pairs have a larger radius outer planet (Weiss et al., 2018) and a similar ordering exists in mass (Millholland et al., 2017). Planet radii measured from transit observations include atmospheres that may be strongly affected by photoevaporation or tidal heating (Millholland, 2019) and are therefore not a reliable estimate of mass (Chen & Kipping, 2017). However, the presence of a marginally significant, but similar trend in mass measurements highlights a shortcoming of the instability scenario. A possible solution could be to consider a mass ordering in the initial conditions as an outcome of the planet formation process that is later partially eroded by collisions. Another potential process may be additional post-nebular accretion of left-over debris. These avenues for continued quantification of the instability mechanism as the process responsible for shaping the terminal architectures of exoplanet systems are worthy of investigation as their post-nebular evolution comes into sharper focus.

2.6 Appendix

Migration prescription

Here we specify details of our ad-hoc migration prescription to construct the original resonant chains. The migration timescale is

$$t_m = \frac{a}{\dot{a}} = -\frac{2 \times 10^5}{\log_{10}(r/\mathrm{AU}) + 1}\ \mathrm{yr} \tag{2.9}$$

where r is the orbital radius. The timescale for eccentricity damping is

$$t_e = \frac{e}{\dot{e}} = -\frac{2 \times 10^2}{r/\mathrm{AU}}\ \mathrm{yr}. \tag{2.10}$$

The purpose of such a prescription is as follows. Capture into resonance depends only on the relative migration rate between a pair of planets. Denoting the inner planet by 1 and the outer planet by 2, that rate is

$$\frac{1}{t_{m,2}} - \frac{1}{t_{m,1}} = \frac{\dot{a}_2}{a_2} - \frac{\dot{a}_1}{a_1} = \frac{\log r_1/r_2}{2 \times 10^5\ \mathrm{yr}} = \frac{\log P_1/P_2}{3 \times 10^5\ \mathrm{yr}}.$$

For $P_2 > P_1$, this rate is negative, and migration is always convergent. Furthermore, the migration rate depends only on the period ratio and not the radius or period itself. The normalization constant in the denominator causes no migration at 0.1 AU. The eccentricity damping timescale is chosen to be approximately two orders of magnitude smaller than the relative migration rate, in line with typical disk models (Tanaka & Ward, 2004; Cresswell & Nelson, 2008).

Figure 2.8 shows a typical capture into a resonant chain using this prescription. Planets spaced just wide of the intended resonance smoothly capture into the resonance and all 20 angles librate. The final eccentricities are consistent with more physically-motivated simulations (Izidoro et al., 2017).

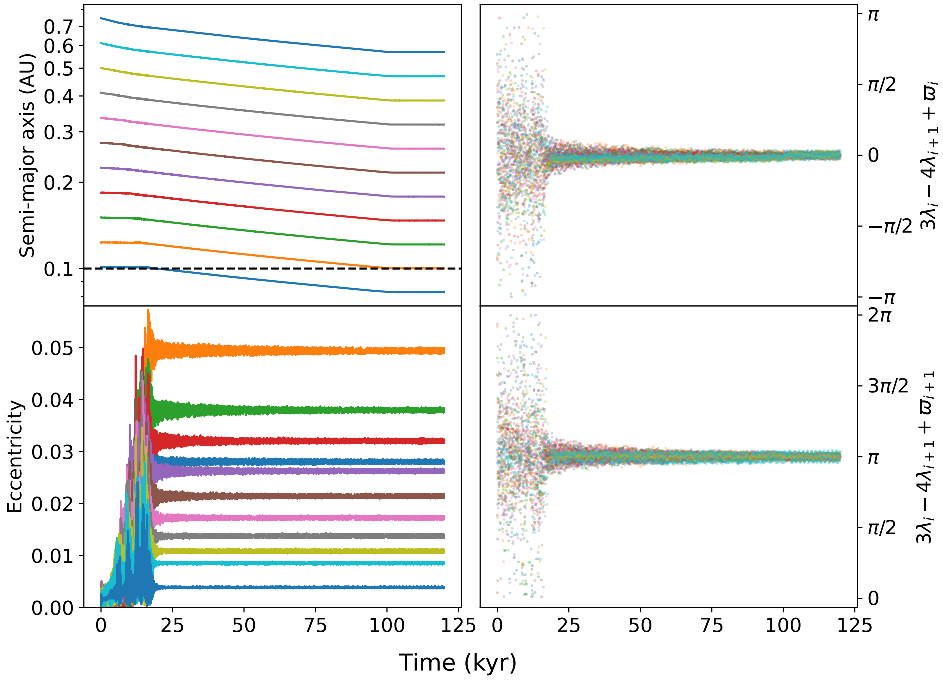

Figure 2.8: Evolution of orbital elements during a typical simulation of capture into a resonant chain. Here, the planet parameters are those of Run 1 (see Table 2.4). Migration and eccentricity damping proceeded from $t = 0$ to $t = 100$ kyr, at which point t_m and t_e increase exponentially, representing gas disk removal. At $t = 110$ kyr, both timescales are set to infinity.

Chapter 3

A CRITERION FOR THE STABILITY OF PLANETS IN CHAINS OF RESONANCES

Goldberg, M., Batygin, K. & Morbidelli, A. (Dec. 2022). “A Criterion for the Stability of Planets in Chains of Resonances.” In: *Icarus* 388, p. 115206. ISSN: 0019-1035. DOI: `10.1016/j.icarus.2022.115206`.

3.1 Introduction

Although compact systems of sub-Neptune planets are abundant, a detailed understanding of their formation remains incomplete. According to most theories of planet formation, planets form in gaseous protoplanetary disks where interactions between the planets and gas are inevitable. These interactions cause inward migration of the planets towards the disk’s inner edge and capture them into chains of mean-motion resonances (Terquem & Papaloizou, 2007; Cresswell & Nelson, 2008; Ida & Lin, 2008; Ida & Lin, 2010; Cossou et al., 2014; Hands et al., 2014). Indeed, we expect that resonant chain systems such as TRAPPIST-1, Kepler-80, Kepler-223, and GJ 876 formed in this way (Mills et al., 2016; Luger et al., 2017).

Yet, population studies of exoplanet systems have revealed that resonant chains are in fact rare and that systems of multiple sub-Neptune planets are typically *not* in resonance (Fabrycky et al., 2014). Thus, either some process prevents the formation of resonances in the first instance, or primordial resonant chains are disrupted after the gaseous nebula dissipates. Recent work (Izidoro et al., 2017; Izidoro et al., 2021; Goldberg & Batygin, 2022) argues for the latter scenario, hypothesizing that widespread dynamical instabilities break the resonances and then a phase of giant impacts sculpts the system. Detailed simulations of such a process produce results matching the observed period ratio distribution, transit multiplicities, and peas-in-a-pod patterns of intrasystem uniformity. However, the mechanism of the instability itself is not well understood from a fundamental level, nor is there a practical way to predict which resonant chain systems are unstable.

The stability of planetary systems has been a topic of research for centuries since the development of celestial mechanics (Laplace, 1799; Le Verrier, 1840; Poincaré, 1899). With the introduction of numerical integration, the Solar System was recognized to be chaotic (Wisdom, 1983; Roy et al., 1988; Laskar, 1989) and hence unpredictable on gigayear timescales, at least on a quantitative level (Batygin & Laughlin, 2008; Laskar, 2008). Now, the rapidly growing population of exoplanetary systems, and their exotic architectures, has spurred a renewed interest in fully understanding the stability of general systems of planets (Deck et al., 2012; Batygin et al., 2015).

Previous studies, while extensive, have generally focused on two-planet systems (Gladman, 1993; Deck et al., 2013; Hadden & Lithwick, 2018; Petit et al., 2018) and the non-resonant 3+ planet regime (Chambers et al., 1996; Quillen, 2011; Petit et al., 2020b; Tamayo et al., 2021; Rath et al., 2022). On the other hand, the stability of planetary systems in chains of resonances has received only limited attention. Early work was primarily empirical: Matsumoto et al., 2012 performed numerical integrations of equal mass planets locked into $k{:}k-1$ resonance and found that the maximum number of planets that could be captured into the chain decreased with increasing k and planet mass. Later work (Matsumoto & Ogihara, 2020) confirmed these conclusions and uncovered the unexpected result that a nominally stable resonant chain could be made unstable by a *decrease* in the mass of either the planets or the star.

On the analytical side, Pichierri & Morbidelli, 2020 considered an equal-mass three-planet system as the simplest instance of a first-order resonant chain. Through involved perturbation theory, they showed that a secondary resonance between the fastest resonant libration frequency and a difference of the synodic frequencies can drive an instability. Rather than continuing their analytical approach, in this work we simplify their results and generalize to unequal masses and an arbitrary number of planets. Our analysis of the Pichierri & Morbidelli, 2020 mechanism naturally leads to a criterion for the stability of a resonant chain, and a limit on the planet mass—or alternatively, multiplicity—in a resonant chain. We verify these results numerically on a suite of synthetic planetary systems.

3.2 Analytical Estimate of Stability

We define a resonant chain as a system of three or more planets in which each adjacent pair of planets is locked into mean-motion resonance. One can construct a wide variety of oscillation frequencies from the orbital elements, but important frequencies can be broadly separated into three categories: synodic, resonant, and secular. Synodic frequencies are linear combinations of the mean motions n_i and do not depend on planet masses. Resonant frequencies describe the oscillations of critical resonant angles which, for two-body first-order resonances, take the form

$$\phi_{i,i+1} = k_i\lambda_{i+1} - (k_i - 1)\lambda_i - \varpi. \tag{3.1}$$

Here, k_i is the resonant index, λ_i is the mean longitude, and ϖ is the longitude of pericenter of the i-th or $i+1$-st planet. Finally, secular frequencies, which arise from orbit-averaged perturbations, are typically much slower than synodic and resonant frequencies and thus are not considered in this work.

Pichierri & Morbidelli, 2020 hypothesized that the onset of dynamical instability in compact resonant chain systems is triggered by the commensurability, or near equality, between a resonant libration frequency and a difference of synodic frequencies. Modulation of the resonant angles by synodic perturbations allows the resonant locks to break, leading to chaotic behavior. Our goal is to extend that work to more than three planets of unequal mass.

Consider a resonant chain of N planets with masses $m_1, ..., m_N$ and in pairwise first-order resonances of $k_1{:}k_1 - 1, \dots, k_{N-1}{:}k_{N-1} - 1$ so that the period ratios are $P_i/P_{i+1} \approx (k_i - 1)/k_i$. Studying the secondary resonance of Pichierri & Morbidelli, 2020 would require writing the Hamiltonian of the entire system. However, we can take a simpler approach by comparing the libration frequencies of the individual resonances to the differences in synodic frequencies throughout the system.

For the purposes of computing libration frequency, we will ignore the contributions of planets that are not in the pair being considered. We verify this assumption below in our n-body simulations. In that case, the angular frequency of libration for the angle $\phi_{i,i+1} = k_i\lambda_{i+1} - (k_i - 1)\lambda_i - \varpi_i$ is approximately (Batygin, 2015)

$$\omega_{i,i+1} = \frac{3n_i}{2}\left(\frac{m_1 + m_2}{M_*}\right)^{2/3}\left[\frac{((k_i - 1)^{10}/k_i^4)^{1/9}}{(3(f_{\rm res})^2)^{-1/3}}\right] \tag{3.2}$$

where M_* is the stellar mass and $f_{\rm res} \approx -0.8k_i + 0.34$ is a constant derived from Laplace coefficients (e.g., Deck et al., 2013). As discussed in Pichierri & Morbidelli, 2020, the $(m_i/M_*)^{2/3}$ scaling is appropriate only at low eccentricities where a shift in the equilibrium point induces a forced eccentricity. At higher e, the scaling is $(m_i/M_*)^{1/2}$.[1]

Synodic frequencies are straightforward to compute. Following Pichierri & Morbidelli, 2020, we have

$$\delta\dot{\lambda}_{i,i+1} = n_i - n_{i+1} = n_i - \frac{k_i - 1}{k_i}n_i = \frac{1}{k_i}n_i \tag{3.3}$$

as the angular frequency of conjunctions of planets i and $i+1$. However, the analysis of Pichierri & Morbidelli, 2020 specifically identifies the *difference* in synodic frequencies as the slower and more relevant frequency. This is

$$\Delta\delta\dot{\lambda}_{i,i+1,i+2} = \delta\dot{\lambda}_{i,i+1} - \delta\dot{\lambda}_{i+1,i+2} = \frac{k_{i+1} - k_i + 1}{k_i k_{i+1}}n_i. \tag{3.4}$$

Synodic frequencies are typically faster than libration frequencies. Thus, overlap is most likely to occur when the slowest difference of synodic frequencies is commensurate with the fastest libration frequency. We define the characteristic quantity for resonant chain stability to be

$$\chi \equiv \frac{\min(\omega_{\rm syn})}{\max(\omega_{\rm lib})}, \tag{3.5}$$

---

[1] Specifically, the change in scaling occurs at $e \sim (|f_{\rm res}|m/(k^2M_*))^{1/3}$, where there is a bifurcation in the resonant equilibria in the phase space of the Hamiltonian (Batygin & Morbidelli, 2013). For the typical systems discussed in this chapter, this corresponds roughly to $e \sim 0.03$.

where the minimum and maximum are taken over all synodic and libration frequencies in the chain, respectively.

So far we have maintained generality, but for simplicity we will now assume that all the resonances have the same index k and the mass of each planet is m. Now, the slowest difference of synodic frequencies is $\Delta\delta\dot{\lambda}_{N-2,N-1,N}$ and the fastest libration frequency is $\omega_{1,2}$. Setting $\chi = 1$ leads to a maximum mass of planets in the chain of

$$m_{\max}/M_* \approx 0.2 \left(\frac{k-1}{k}\right)^{1.5N} k^{1.2}(k-1)^{-6.2}. \tag{3.6}$$

This is an explicit computation of the critical mass identified by Pichierri & Morbidelli, 2020.

3.3 Numerical Tests

We ran a suite of numerical experiments to test the validity of Equation 3.6 for different values of k and N. We place N planets of mass $m/M_* = 3 \times 10^{-6}$ on orbits $1-2\%$ wide of the k:$k-1$ resonance. The semi-major axis of the inner planet is fixed and eccentricity damping is applied to all planets. To ensure sequential capture into resonance, migration is turned on for every planet except the innermost one, using a ratio of migration to eccentricity damping timescales of $\tau_m/\tau_e = 3 \times 10^2$. Once the two-body resonant angles begin to librate, we remove migration and eccentricity damping exponentially so that the system settles to its stable multi-resonant state. Typical orbital eccentricities at this point are ~ 0.01. Then, we begin exponentially increasing the mass of each planet adiabatically (i.e., with $\tau_m \gg 1/\omega_{1,2}$) in order to increase the libration frequency. Once an instability occurs (defined as any planet orbit becoming hyperbolic) we stop the simulation and record the planet masses. We attempted this process for integer values of k between 2 and 8, and N between 3 and 9. For each pair of k and N, we repeated the simulations 10 times with slightly different initial conditions to smooth over the chaotic behavior, although in all cases the scatter was very small. Our simulations use the `whfast` n-body integrator from the `rebound` software package and a maximum timestep of $1/20$ of the inner orbital period (Rein & Tamayo, 2015). Migration and eccentricity damping are included from the `reboundx` extension (Tamayo et al., 2020b).

An example of such a simulation is shown in the left panel of Figure 3.1, which has $N = 3$ and $k = 5$. As the planetary masses are increased, the libration frequencies increase, but the synodic frequencies remain constant. After 2×10^6 orbits of the inner planet, the resonant angles begin to circulate and the orbital eccentricities grow rapidly until there is a close encounter. Within a few orbits, at least one planet orbit becomes hyperbolic and the simulation ends. The onset of instability happens almost precisely when the highest-frequency mode of the innermost resonant angle (involving λ_1 and λ_2), as estimated by Fourier transform of the libration angle,

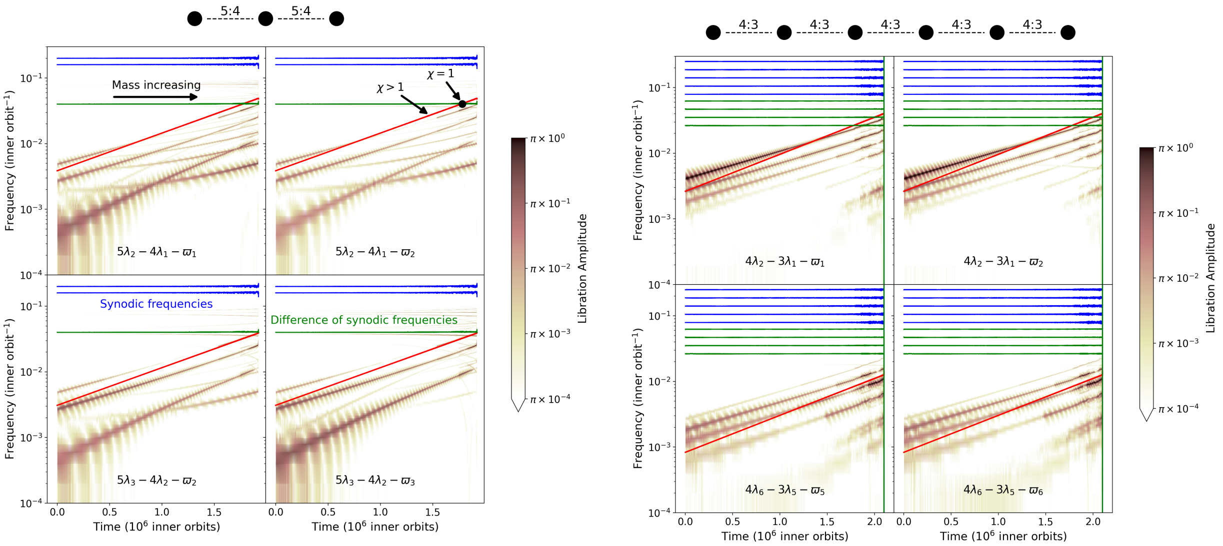

Figure 3.1: The evolution of resonant libration and synodic frequencies as planet masses are increased until the instability occurs, for two initial planet configurations shown as cartoons above each grid. The left grid corresponds to a system with 3 planets started in 5:4 resonances. Each panel represents one of the four resonant angles; the red colormap is a spectrogram, or the amplitude of the Fourier transform over time, of that angle. Each resonant angle has multiple libration modes, the frequencies of which increase with mass. The bright red lines plot the analytical estimate of the libration frequency from Equation 3.2. Horizontal colored lines indicate synodic frequencies: blue lines are the synodic frequencies themselves and the green line is the difference of synodic frequencies (Equation 3.4). The right grid is the same as the left, but with 6 planets in a chain of 4:3 resonance. Only the libration frequencies for the innermost (top) and outermost (bottom) pairs of planets are plotted.

intersects the difference of synodic frequencies. The bottom panels show that the libration of the resonant angle involving λ_2 and λ_3 is slower and a resonance with the synodic frequencies does not occur within the simulation timeframe. Figure 3.1 also demonstrates the accuracy of the analytical estimate for libration frequency, which remains within a factor of 2 of the true value throughout the simulation. The libration frequency approximation predicts that the instability will arise at $m_{\max}/M_* = 1.0 \times 10^{-4}$, whereas in the simulation the instability comes slightly later, at $m_{\max}/M_* = 1.4 \times 10^{-4}$. Nevertheless, the numerically-estimated libration frequencies grow more steeply with mass than the analytical estimate, suggesting that the low eccentricity assumption in Equation 3.2 has been violated.

A more complicated example is shown in the right panel of Figure 3.1 in which $N = 6$ and $k = 4$. Here, the frequency structure is more complex and the outermost synodic frequencies are slower. At the first crossing of libration and synodic frequencies, there is a resonant kick and the libration amplitudes increase instantaneously (visible as the blue synodic frequency lines becoming thicker).

Upon the equality of the fastest libration frequency and the second-slowest synodic frequency, the resonant angles begin to circulate and the instability is triggered. Because the instability happens after the libration frequency of the inner planet pair has ‘overshot’ the difference in synodic frequencies of the outer triplet, the analytical maximum mass prediction is an underestimate of the simulation results by a factor of ~ 2.

The full set of simulations is summarized in Figures 3.2 and 3.3. Figure 3.2 explores how the maximum planet mass varies with resonant index k for constant multiplicity. Our analytical estimate is an excellent fit to the numerical results over a broad range of parameter space. In particular, Equation 3.6 maintains accuracy for values of k between 3 and 7, correctly reproducing the downward trend with k. This trend is in fact analogous to the Hill spacing stability criterion in non-resonant systems because the semi-major axis ratios are smaller for higher k. However, instability in non-resonant systems can be fully accounted for by averaging over synodic terms and considering two-body resonance overlap and three-body resonance diffusion (Petit et al., 2020b; Rath et al., 2022). Indeed, Figure 3.2 demonstrates that the non-resonant stability boundary from Petit et al., 2020b, including the > 4 planets correction, consistently predicts a smaller maximum planet mass than is actually seen in resonant chains. Resonant chains can be stable at separations for which non-resonant systems are unstable because resonant chains reside at a fixed point in the phase space. However, interactions between synodic and resonant frequencies can excite the system away from this fixed point and into the surrounding chaotic region.

Figure 3.3 contains the same data but shows how the maximum mass varies with multiplicity N for a constant resonant index. Our analytical estimate predicts an exponential decrease in m_{max} with N. While this is true for small N, the dependence on multiplicity seems to flatten out near ~ 6 planets. This may be because the inner resonance is less able to “communicate” its frequency to the outer planets for high values of N, and as a result, the chain behaves like one with fewer planets. It is worth noting that a similar pattern of saturation, in which stability decreases with N but flattens after $N \gtrsim 5$, occurs in the non-resonant case (Chambers et al., 1996). A somewhat more accurate definition of χ (Equation 3.5) would therefore consider only adjacent subsystems of $5 - 6$ planets. However, to maintain simplicity, for this work we will use the previous definition that assumes perfect coupling among all planets.

Figure 3.3 also shows poor agreement between our prediction and simulations for the 2:1 resonance. This is likely due to the presence of indirect terms and asymmetric libration in that resonance (Beauge, 1994). That is, when eccentricities grow past ~ 0.03, the libration centers shift away from 0 and π. This is exceeded in our numerical experiments for the 2:1 resonance and our analytical estimates do not consider the asymmetric libration.

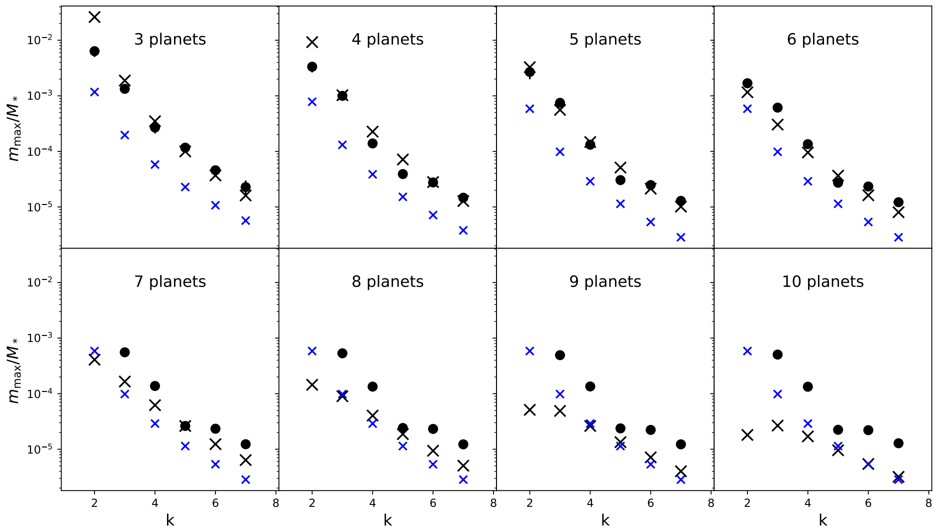

Figure 3.2: Maximum planet mass in a resonant chain as a function of resonant index k, for different planet multiplicities. Black crosses mark the analytical estimate from Equation 3.6, while dots show the results of our numerical simulations. The smaller blue crosses are the *non*-resonant stability boundary from Petit et al., 2020b.

3.4 Applications to the Formation of Planetary Systems

While the results of the previous section are promising, it remains to be demonstrated whether the criterion for resonant chain stability is relevant to the more complex system architectures that are anticipated in the formation of compact super-Earth systems. Here, we apply the criterion to simulations of super-Earth system formation to show that it effectively predicts their long-term stability as well.

Our test sample is the set of synthetic planetary systems produced in the simulations of Izidoro et al., 2021. The final systems closely replicate many aspects of the observed sample of compact super-Earth systems. Beyond n-body dynamics, these simulations incorporate orbital migration and eccentricity and inclination damping due to planet-disk interactions as well as pebble accretion. In other words, the simulation suite of Izidoro et al., 2021 constitutes a successful instance of population synthesis. Within the context of these formation simulations, the gas disk dissipates at $t = 5$ Myr, but the integrations continue until $t = 50$ Myr in order to allow for instabilities that were suppressed by the protoplanetary disk to arise. We consider "stable" systems to be those that do not experience an instability after $t = 5$ Myr, and "unstable" systems to be those that did experience an instability after $t = 5$ Myr.

We removed planets with masses below $0.3M_\oplus$ because they tend to interfere with analyzing the chain while not contributing significantly to the dynamics. We also removed systems with a pair of planets that have semi-major axis ratios less than 1.05 because our criterion does not account for the 1:1 resonance. After these cuts, there were 54 unstable systems and 30 stable ones.

The next step is to identify the likely resonances within the chain. We do this by computing the period ratio of adjacent planets. If the ratio is within 3% of a first-order resonance k:$k-1$, for $1 < k < 11$, we assume the planet pair lies in that resonance. If not, we search for second- and third-order resonances with the same method but halve the threshold distance. In the case that no candidate resonance is found, we consider the chain to end at that point. For each planetary system, this process generates a collection of resonant chains separated by secular architecture. Chains with fewer than three planets are discarded because they have no difference of synodic frequencies.[2] We then calculate the libration frequency $\omega_{i,i+1}$ for each first-order resonance using Equation 3.2 (higher-order resonances are ignored) and the difference of synodic frequencies $\Delta\delta\dot{\lambda}_{i,i+1,i+2}$ for each (adjacent or non-adjacent) planet triplet using Equation 3.4. Finally, the stability criterion is computed using Equation 3.5. Because some systems contain multiple resonant chains, and an

---

[2] Specifically, stability for two planets is set by the Hill criterion (Gladman, 1993; Petit et al., 2018)

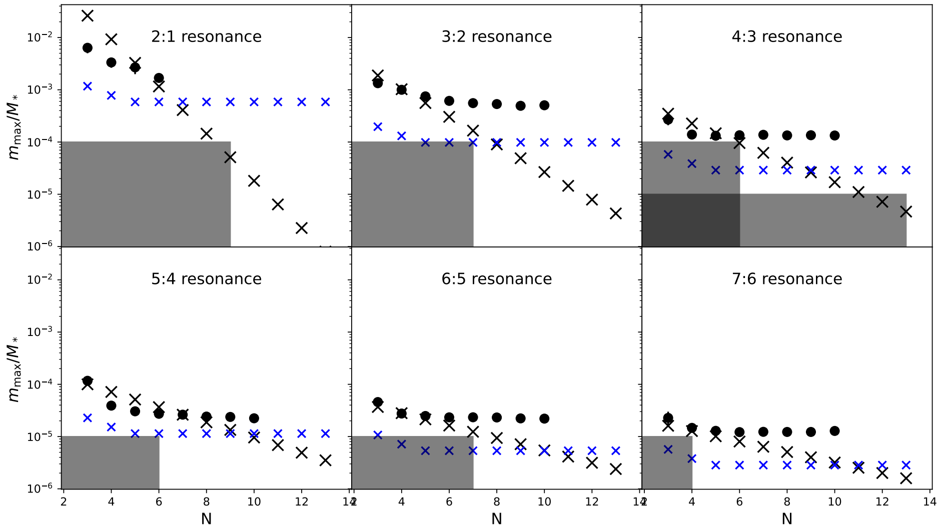

Figure 3.3: Maximum planet mass in a resonant chain as a function of planet multiplicity N, for different resonances. As in Figure 3.2, black and blue crosses mark the resonant and non-resonant criterion, respectively, while dots show the results of our numerical simulations. Gray boxes reflect the implied regions of stability from Matsumoto et al., 2012 and Matsumoto & Ogihara, 2020.

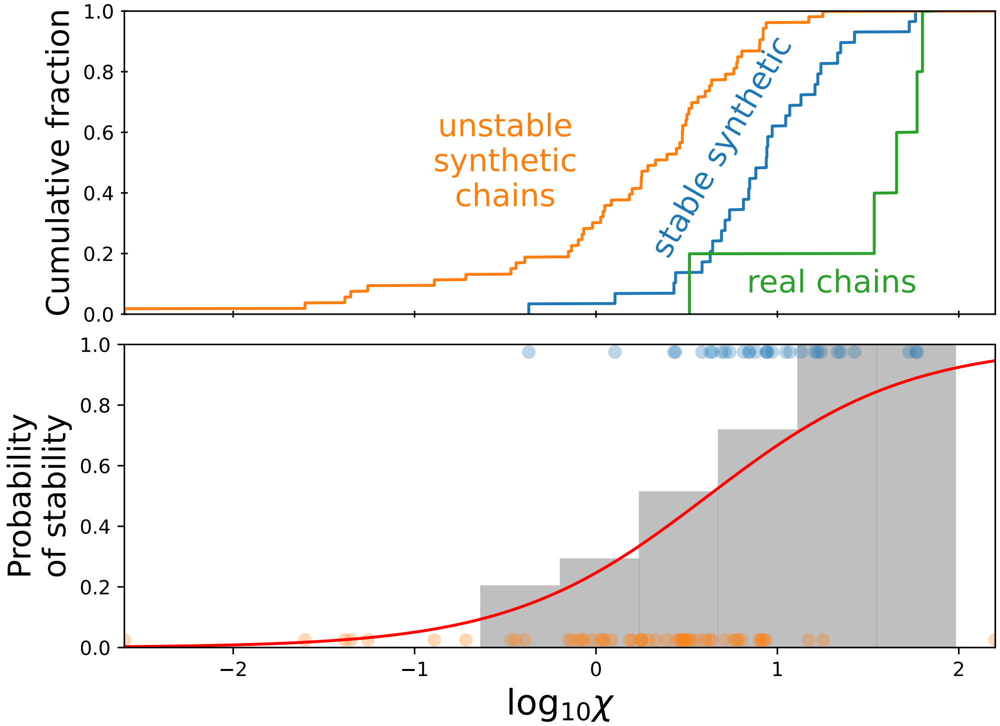

Figure 3.4: Relationship between our stability criterion χ and the true stability of synthetic and real resonant chains. Top: the cumulative distribution of $\log_{10}\chi$ for unstable and stable synthetic resonant chains from Izidoro et al., 2021, and the half-dozen well-characterized chains with small planets. Bottom: blue and orange points mark the same synthetic systems as in the top panel. Gray bars show the fraction of systems within that bin that are stable; the red curve is a logistic regression fit of the probability of stability.

instability in any one of the chains classifies the system as unstable, the system χ is taken to be the smallest χ of any of the chains.

Our hypothesis is that the secondary resonance sets a stability threshold of $\chi_{\rm crit} \approx 1$, above which the chain is stable. Of the 30 stable systems, 29 have $\chi > 1$. However, the unstable systems have a broader distribution, clustering around $\chi \sim 2$. To quantify the boundary, we used a logistic regression (Figure 3.4) to model the probability of stability given only the $\log_{10}\chi$ of the chain. The fit suggests that the threshold is $\chi_{\rm crit} \sim 3$. That is, stability over 10^9 orbits seems to prefer wider spacing between synodic and libration frequencies than our criterion predicts.

Such a result is surprising in the context of our experiments in Section 3.3, which suggest that $\chi_{\rm crit}$ is near unity for $N \lesssim 6$ and *smaller* for higher-multiplicity systems. While fully understanding this discrepancy is outside the scope of our work, we can speculate on possible sources. Our resonant chains formed in Section 3.3 are especially "clean," that is, all two-body and three-body resonant angles librate with small amplitudes. In contrast, larger libration amplitudes in the Izidoro et al., 2021 systems could render them more vulnerable to higher-order secondary resonances that appear at $\chi > 1$. Another possible explanation is that modulation of the resonant frequencies and widths by secular interactions with other planets in the system causes χ to vary over long timescales (Tamayo et al., 2021).

As for the *observed* set of resonant chains, Figure 3.4 shows that they generally have $\chi \sim 30-100$, with the exception of TRAPPIST-1, for which $\chi \approx 3$. Finally, it is important to note that these simulations only capture the first 50 Myr, but instabilities can occur after billions of orbits (Petit et al., 2020b). Some systems recorded as 'stable' might actually be unstable with a longer integration time that is representative of the age of typical exoplanet systems.

3.5 Discussion

Inspired by the analytical study of resonant chains, we have identified a criterion to quantify the stability of planets locked in a chain of resonances in accordance with the Pichierri & Morbidelli, 2020 mechanism. We argue that the overlap between a fast resonant libration frequency and a slow difference of synodic frequencies leads to chaotic behavior and a dynamical instability. Our criterion predicts a maximum planet mass in a chain of N planets with $k{:}k-1$ resonances and closely agrees with numerical simulations for $k > 2$ and $N \lesssim 6$.

In addition, this mechanism explains the counterintuitive result found by Matsumoto & Ogihara, 2020 wherein an instability in a maximally-packed resonant chain can be triggered by decreasing the planet masses by 10%. Specifically, resonant chain formation occurs in a dissipative environment that suppresses the instability. During migration, the maximum libration frequency can approach, or even exceed, the slowest synodic frequencies, but the system settles into a local island of stability with $\chi < 1$. After the disk is removed and the masses are decreased, the libration frequencies change and the system enters the chaotic region between the island of stability and the $\chi = 1$ boundary. While initially discovered numerically, mass loss may in fact be a plausible candidate for the trigger of dynamical instabilities in packed resonant chains. Indeed, mass loss of this magnitude is physically reasonable as a result of photoevaporation (Owen, 2019). Furthermore, the highest libration frequency typically comes from the innermost resonance and hence depends only on the masses of the inner two planets. Those planets are most susceptible to photoevaporation by virtue of their proximity to the star.

Machine learning models have been especially successful in analyzing the stability of multi-planet systems. To compare our results to previous work, we used the state-of-the-art SPOCK model (Tamayo et al., 2020a) to predict the stability of the synthetic chains presented in Section 3.4. We set the probability threshold to be 0.5 and ran the model in two different ways. First, we use as input each system in its entirety from Izidoro et al., 2021, only excluding the planets below $0.1M_\oplus$. SPOCK correctly predicted the stability of 13 of the 30 stable systems and 42 of the 54 unstable ones. Second, we input each of the individual resonant chains identified in the systems of Izidoro et al., 2021, as described in Section 3.4, and use SPOCK to compute the probability of their stability. We treat those as independent random variates, and for each system we estimated the probability of stability of the whole system by computing the probability that every chain within it is stable. In that case, SPOCK correctly predicted the stability of 20 of the 30 stable systems and 31 of the 54 unstable ones. As a comparison, our one-dimensional logistic regression (Figure 3.4) achieves $25/30$ for stable systems and $40/54$ for unstable with the same probability threshold. Accordingly, the specific problem of resonant chain stability constitutes an instance where a careful analytical treatment is comparable to or surpasses general supervised machine learning techniques.

If it is indeed true as some have suggested that non-resonant systems of small planets are the products of instabilities, the mechanism of instability is of considerable importance. Previous suggestions include changes in the stellar J_2 moment (Spalding & Batygin, 2016), stellar or planetary mass loss (Matsumoto & Ogihara, 2020), or a simple overpacking of the system during the disk phase (Izidoro et al., 2017). Our work does not rule out any of these mechanisms, but clarifies the dynamics underpinning the onset of the instability. Future work should explore the consequences of each of these instability mechanisms to determine whether they leave signatures detectable in the planet population.

Chapter 4

A TIDAL ORIGIN FOR A THREE-BODY RESONANCE IN KEPLER-221

Goldberg, M. & Batygin, K. (July 2021). “A Tidal Origin for a Three-body Resonance in Kepler-221.” In: *The Astronomical Journal* 162, p. 16. ISSN: 0004-6256. DOI: `10.3847/1538-3881/abfb78`.

4.1 Introduction

The tally of extrasolar planets has dramatically increased over the past decade and a half. Transit and radial velocity surveys have uncovered hundreds of exoplanetary systems with multiple planets and architectures differing considerably from our Solar System. Accordingly, the census of extrasolar planets with orbital periods shorter than a year has come into unprecedented level of focus (Fabrycky et al., 2014).

Among the key overall results that has stemmed from the recent flurry of planetary detections has been a characterization of “conventional” orbital architecture displayed by close-in extrasolar planets. At face value, the properties of a representative short-period planetary system are easily summarized: typical planets have sizes that are a few times larger than that of the Earth, often occur in multiples, and occupy nearly planar, circular orbits that are separated by tens of mutual Hill radii (Hadden & Lithwick, 2014; Weiss et al., 2018; Millholland et al., 2017; Wang, 2017). Furthermore, most multi-planet systems exhibit long-term (~Gyr) dynamical stability (Tamayo et al., 2020a).

In exceptional cases, important additional insight into the orbital machinery of a given system can be gleaned from combined transit timing analysis and radial velocity measurements (Petigura et al., 2018; Petigura et al., 2020). Direct characterization aside, however, a thornier question concerns how orbital layouts of extrasolar planets arise in the first place. In this regard, a complete understanding of the physical processes that shape exoplanetary configurations remains elusive, and constitutes a topic of active research (see Raymond & Morbidelli, 2020 for a review). In fact, even the epoch at which the final orbital architecture is set is a subject of debate.

Within the context of “classical” models of planet formation, the present-day architecture of planetary systems was assumed to be inherited from the detailed structure of the protoplanetary disk from which the planets emerged (Cameron, 1988). Recent theoretical progress on the origin of the exoplanetary period distribution, as well as the early evolution of the solar system itself, however, indicates that violent, post-nebular dynamical instabilities may play an important role in sculpting the terminal outcome of the planet formation process (Tsiganis et al., 2005; Morbidelli, 2010; Izidoro et al., 2017; Esteves et al., 2020). Unfortunately, this markedly chaotic evolutionary framework renders a deterministic model that unambiguously connects the properties of the planets' natal disk with their present-day (observable) attributes an impossibility.

A somewhat rare exception to this rule of thumb are resonant chains—systems of planets locked into sequential mean-motion commensurabilities with one-another. Because resonant entrainment necessitates dissipative, extrinsically-driven evolution of planetary orbits, systems that exhibit resonant dynamics today are routinely interpreted as signposts of convergent orbital migration that was facilitated by their natal disks. In other words, resonant chains represent "pristine" orbital architectures, sculpted by the birth environment of the planets. Examples of such systems include GJ876, Kepler-80, Kepler-223, and TRAPPIST-1, and it is worth noting that dynamical origins of each of these systems have been extensively studied extensively within the literature (Rivera et al., 2010; MacDonald et al., 2016; Mills et al., 2016; Gillon et al., 2017; Agol et al., 2021, and references therein). Precise characterization of the resonant configuration has even been used to constrain the migration rate and order of capture into resonance (Delisle, 2017).

Even more unique within the current census of exoplanets is the orbital structure of the Kepler-221 system. Unlike the vast majority of known multi-planetary configurations, Kepler-221 is not devoid of orbital commensurability. Simultaneously, however, Kepler-221 is not a standard example of a resonant chain. Rather, it exhibits a three-body commensurability far away from any discernible two-body resonances. Understanding the genesis and long-term evolution of this remarkable aggregate of planets is the primary goal of this work. In particular, here we demonstrate that the current configuration of Kepler-221 is unlikely to have formed in-situ. Instead, it can be readily understood as a resonant chain that underwent long-range divergent migration as a consequence of persistent tidal damping. Moreover, we argue that tidal dissipation in this system almost certainly stems from obliquity tides, implying that the spin axes of at least one of the Kepler-221 planets are significantly misaligned with respect to the orbital plane.

The remainder of the chapter is organized as follows. In Section 4.2, we briefly review orbital resonances and introduce Kepler-221 in the context of other Kepler multiplanet systems. In Sections 4.3 and 4.4 we evaluate two potential mechanisms for forming the resonances in Kepler-221. Finally, in Section 4.5 we summarize our results, delineate the limitations of our work and discuss the value of future constraints.

4.2 Orbital Resonances

Orbital mean-motion resonances (MMRs) are defined by the libration (bounded oscillation) of a critical *resonant* angle. For a first-order (in eccentricity) two-body resonance, the resonant angle takes the form

$$\theta = p\lambda - (p+1)\lambda' + \varpi \tag{4.1}$$

where λ and λ' are the mean longitudes of the inner and outer body, respectively, ϖ is the longitude of pericenter for either of the bodies, and p is an integer. Because apsidal precession is typically much slower than orbital motion ($|\dot{\varpi}| \ll n$), the associated period ratio is $P'/P \sim (p+1)/p$. For systems with more than two planets, critical angles can be combined to yield three-body relations. For example, in the Kepler-223 system mentioned above, the angles

$$\phi_1 = \lambda_b + 2\lambda_c - \lambda_d \tag{4.2}$$

$$\phi_2 = \lambda_c - 3\lambda_d + 2\lambda_e \tag{4.3}$$

librate. Such relations are of considerable importance because transit timing variation (TTV) analyses of some resonant systems have shown that *only* these angles librate (Goździewski et al., 2016; Mills et al., 2016; MacDonald et al., 2016). The formation of these systems (where three-body angles librate but two-body angles do not) has perplexed previous studies and remains an unanswered question. The aforementioned works have generally relied on the possibility that TTV analyses lack sufficiently precise eccentricity vector data to demonstrate that two-body angles are librating, and that further data would show that they in fact are librating. However, the Kepler-221 system, the subject of this study, indicates that three-body resonances can be active very far from two-body resonances. Following Goździewski et al., 2016, we denote systems with librating three-body resonant angles, but no librating two-body resonant angles, *pure* three-body resonances.

Kepler-221 (also known as KOI-720) is a G-type star ($T_{\text{eff}} = 5255$K) in the Kepler field. The Kepler data reduction pipeline identified four planets with the parameters shown in Table 4.1. The innermost planet, b, has a radius near the radius gap between super-Earths and sub-Neptunes, whereas the outer three planets have radii in excess of $2R_{\oplus}$, placing them firmly in the sub-Neptune category (Fulton et al., 2017). The period ratios of adjacent planets, starting with c to b, are 2.035, 1.765, and 1.829. With the exception of b and c, which appear to be a few percent wide of a 2:1 resonance, none of the planet pairs lie near first- or second-order two-body commensurabilities. This masses of the planets, are, unfortunately, unconstrained.

Despite the lack of pronounced two-body resonances within the system, a three-body commensurability exists (Fabrycky et al., 2014). Specifically, the frequency

$$B = 2n_b - 5n_c + 3n_e \approx -0.000727 \pm 0.000440 \text{ degrees/day} \tag{4.4}$$

is exceptionally small, suggesting possible libration of the critical angle

$$\phi = 2\lambda_b - 5\lambda_c + 3\lambda_e. \tag{4.5}$$

Planet	Period (d)	Transit mid-point (BJD-2454900)	Radius ($R_\oplus$)	Impact parameter
b	2.795906 ± 0.000004	65.72929 ± 0.00084	1.71 ± 0.17	0.61 ± 0.24
c	5.690586 ± 0.000004	107.04865 ± 0.00037	2.93 ± 0.27	0.04 ± 0.16
d	10.041560 ± 0.000011	70.08456 ± 0.00060	2.73 ± 0.25	0.36 ± 0.20
e	18.369917 ± 0.000029	64.86048 ± 0.00087	2.63 ± 0.25	0.26 ± 0.22

Table 4.1: Observed transit parameters of the Kepler-221 system.

If true, the orbital clockwork exhibited by these planets would render Kepler-221 a genuinely unusual member of the Kepler planetary census, and entail remarkable constraints on its long-term tidal evolution.

Beyond a peculiar orbital architecture, Kepler-221 exhibits markers of exceptional youth within the Kepler sample. In particular, stellar lithium abundance is an age diagnostic because Li is rapidly consumed in fusion reactions relatively early in a star's lifecycle. While determining precise age from lithium features is difficult, Kepler-221's large lithium abundance is a strong indication that it is younger than the Hyades ($\sim$ 650 Myr) (Berger et al., 2018). Additionally, the California-Kepler Survey (Petigura et al., 2017) obtained a high-resolution optical spectrum of Kepler-221 using Keck-HIRES to measure bulk stellar properties. Based on an analysis of that spectrum using the technique of Isaacson & Fischer, 2010, the California Planet Search team (Andrew Howard, private communication) found a stellar activity metric of $\log R'\mathrm{HK} = -4.49$, implying a rough stellar age of $\sim$ 600 Myr comparable to the Hyades cluster (Mamajek & Hillenbrand, 2008). In contrast with this estimate, many studies of orbital evolution of Kepler planets through tidal dissipation assume Sun-like ages of 5 or 10 Gyr (Silburt & Rein, 2015; Lee et al., 2013; Millholland & Laughlin, 2019). As we will show below, this order-of-magnitude discrepancy in evolutionary timescale translates to strong constraints on tidal parameters and the dissipation mechanism of Kepler-221's planets.

Resonant libration in the Kepler-221 system?

Measuring the libration of the angle ϕ is challenging with the current data. Transiting exoplanet detections report the time of each inferior conjunction, that is, when the mean longitude $\lambda = \pi/2$. However, libration angles depend on mean longitudes at different points in the orbit. Even if the system is assumed to be coplanar, a global system fit requires 5 parameters per planet, for a total of 20 free parameters. Kepler-221 shows only weak TTVs, effectively precluding any chance to constrain planet masses and eccentricities. Therefore, actually determining whether any critical angle is librating for Kepler-221 is probably impossible with current measurements.

However, because there are many transits, the orbital frequencies *are* well-constrained and therefore the derivative $\dot{\phi} = B$ is also well-constrained. So, we appeal to the closeness of B to zero to argue

Object	Mass ($M_\oplus$)	Period (d)	Mean longitude (deg)
Star	0.95 $M_\odot$		
b	3.0	2.79584	176.7625
c	9.6	5.69023	67.8067
d	9.0	10.04346	7.3874
e	9.6	18.37103	168.9630

Table 4.2: Initial conditions used for simulations.

that the angle ϕ is likely librating. To demonstrate, we pick a particular set of initial conditions for Kepler-221 that is consistent with TTVs (Table 4.2). Because the true planet masses are unknown, we chose them arbitrarily, ensuring they agree with the probabilistic mass-radius relation of Chen & Kipping (2017). For definitiveness, we assume coplanar and initially circular orbits throughout. For all integration reported in this work, we use the `whfast` integrator in the `rebound` software package and set the timestep to between 1/15 and 1/12 of the period of the innermost orbit (Rein & Tamayo, 2015). This set of initial conditions produces libration of the critical angle ϕ around 180° (Figure 4.1). Furthermore, using the three-body resonance properties analytically calculated in Quillen, 2011, we find the resonance width in frequency (B) space to be ~ 0.0004 degrees/day, comparable to the measured value of B.

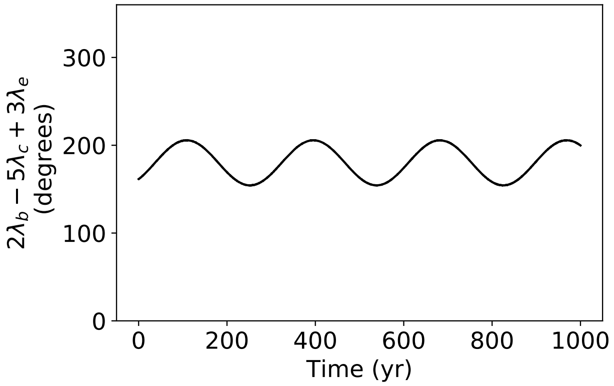

Figure 4.1: Libration of the three-body resonant angle in a particular configuration of Kepler-221 planets consistent with available data.

In principle, one could argue that given the large number of Kepler multiplanet systems and the number of possible coefficients on the critical angle, the slow evolution of the critical angle for Kepler-221 is coincidental. To test this, for each transiting exoplanet system with at least 3 planets, obtained from the Exoplanet Archive,[1] we computed the distance to resonance parameter

$$B = pn_1 - (p+q)n_2 + qn_3 \tag{4.6}$$

---

[1] `exoplanetarchive.ipac.caltech.edu`

System	$\|B\|$ (deg day^{-1})	$\|B\|/\langle n\rangle$ (deg)	B expression	# planets	Adjacent?	Resonant Chain?
TRAPPIST-1	0.000072	0.000070	$n_d - 2n_e + n_g$	7	No	Yes (Gillon et al., 2017)
Kepler-221	0.000727	0.000590	$2n_b - 5n_c + 3n_e$	4	No	?
TOI-178	0.000649	0.001447	$n_e - 3n_f + 2n_g$	6	Yes	Yes (Leleu et al., 2021a)
Kepler-80	0.006714	0.007537	$n_e - 2n_b + n_g$	6	No	Yes (MacDonald et al., 2016)
Kepler-60	0.005504	0.007814	$n_b - 2n_c + n_d$	3	Yes	Yes (Goździewski et al., 2016)
K2-138	0.008791	0.010918	$2n_d - 5n_e + 3n_f$	5	Yes	Yes (Christiansen et al., 2018)
K2-72	0.030943	0.039504	$5n_b - 9n_d + 4n_c$	4	Yes	Maybe (Crossfield et al., 2016)
Kepler-223	0.035062	0.054959	$n_b - 2n_c + n_d$	4	Yes	Yes (Mills et al., 2016)
Kepler-327	0.083137	0.060542	$3n_b - 8n_c + 5n_d$	3	Yes	?
Kepler-184	0.028801	0.077570	$n_b - 4n_c + 3n_d$	3	Yes	?

Table 4.3: The ten systems with frequencies B closest to zero, for all transiting planet systems; we show only the frequency nearest to zero for each system.

for all positive coprime integer values of p, q with $p+q < 10$, where n_1, n_2, n_3 are the mean motions for any three distinct planets in the system in ascending period order, resulting in approximately 18,000 individual frequencies. We then scale this frequency by the average of the mean motions $\langle n\rangle$ to get a dimensionless frequency $|B|/\langle n\rangle$. The values of $|B|/\langle n\rangle$ closest to zero are shown in Table 4.3 along with basic information about the system and whether the planet triplet is adjacent. TRAPPIST-1, TOI-178, Kepler-80, Kepler-60, K2-138, K2-72, and Kepler-223 are known resonant chain systems (Gillon et al., 2017; Leleu et al., 2021a; MacDonald et al., 2016; Goździewski et al., 2016; Christiansen et al., 2018; Migaszewski et al., 2012; Mills et al., 2016). The fact that $|B|/\langle n\rangle$ for Kepler-221 is characteristic of resonant chain values is indicative that its closeness to zero is not coincidental. We note also that the next smallest value of $B/\langle n\rangle$ for Kepler-221, $3n_c - 8n_d + 5n_e \approx 0.96$ degrees/day, is more than 3 orders of magnitude larger than the one given in Eq. 4.4. We conclude that no further commensurabilities exist in the system, and that planet d is not involved in the resonant dynamics.

As a separate check, we compared the distribution of all values of $|B|/\langle n\rangle$ with one obtained by bootstrapping randomly selected periods. Specifically, for each transiting system with N planets, we drew N planet periods randomly from the distribution of all planet periods, without replacement, and computed the new distance to resonance parameter as above. We repeated this bootstrapping process 10000 times. Figure 4.2 shows the distribution of the dimensionless parameter $|B|/\langle n\rangle$ for the bootstrapping test compared to the observed values. There appear to be two distributions: non-resonant planet triplets are uniformly distributed near zero, but a small number of planet triplets have exceptionally small values of $|B|/\langle n\rangle$. Kepler-221 appears to be part of the latter distribution. Its lowest value of $|B|/\langle n\rangle$ is larger than only 3×10^{-6} of the bootstrap distribution. Therefore, only 0.06 of the $\sim 18,000$ computed frequencies would be expected to be less than it. We thus conclude that Kepler-221 is unlikely to coincidentally lie at this commensurability, and note that there are no other systems with such a property that have not been previously identified as unique three-body resonant chains in the Kepler sample.

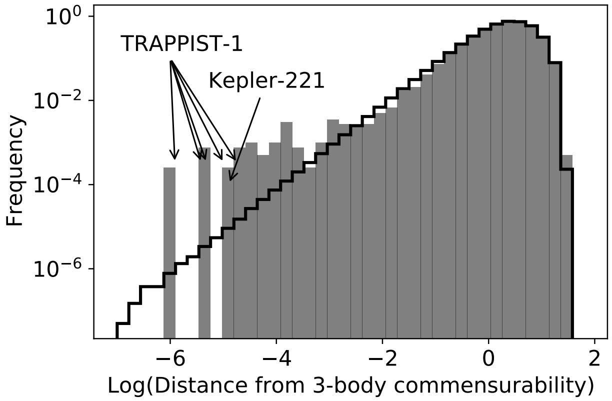

Figure 4.2: The distribution of the B parameter normalized by average mean motion, indicating closeness to resonance. The gray histogram is the distribution of all computed $B/\langle n \rangle$ dimensionless frequencies from the transiting multiplanet sample. The black line is the simulated distribution formed by reshuffling all planet periods.

4.3 In-situ Resonance Capture

If the planets of Kepler-221 are indeed entrained in a three-body resonance, an immediate question arises: how was this commensurability established? Resonances represent only a small fraction of the parameter space and are not expected to occur coincidentally. Instead, they are effective potential wells that act as attractors under convergent migration or other dissipative mechanisms (Papaloizou & Terquem, 2010). As migrating planets pass through orbital commensurability, the resonance can "capture," causing the planet pair to remain in resonance as migration continues (Henrard, 1982; Borderies & Goldreich, 1984). Provided sufficiently slow migration, resonance capture is highly effective, so much so that the dearth of resonances in the Kepler sample constitutes a problem (Adams et al., 2008; Izidoro et al., 2017). The case of two-body resonance capture is well-understood (Batygin, 2015). For pure three-body resonances, numerical simulations of migration and resonance capture of three-planet systems have found pure three-body resonances to be extremely rare or nonexistent (Gallardo et al., 2016; Charalambous et al., 2018).

Nevertheless, Kepler-221 might represent a pathological case, and we have attempted to simulate capture numerically. Starting with the parameters used for Figure 4.1, we displaced planet e slightly inside or outside of the resonance, and then applied semi-major axis migration towards the resonance. Even at the extremely slow migration rate of 10 Gyr e-folding time, far slower than protoplanetary disk-driven migration (Paardekooper et al., 2010), convergent and divergent migration are not sufficient to capture into a pure three-body resonance. The critical angle continues to circulate as the system passes through the resonance and exhibits the characteristic jump over the width of the resonance (Figure 4.3).

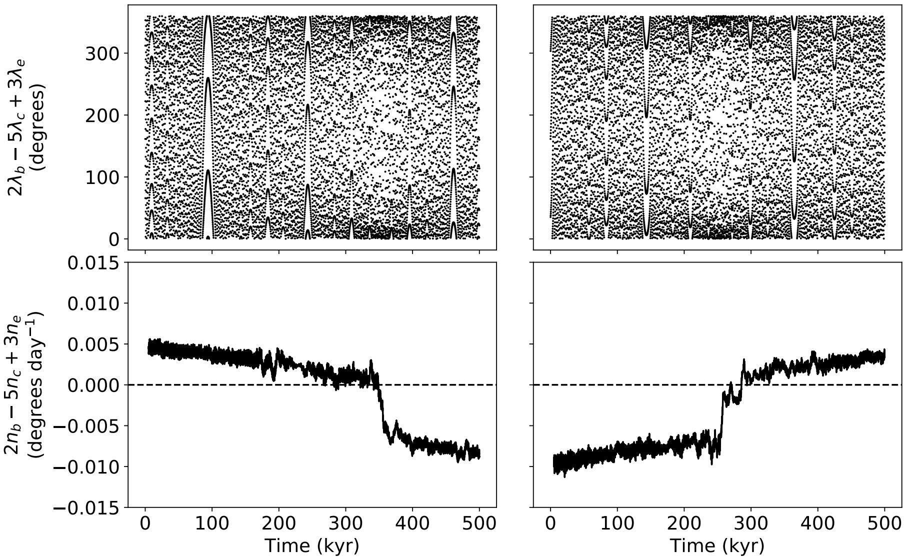

Figure 4.3: Encounters of the Kepler-221 planet with a pure three-body resonance by convergent (left) and divergent (right) migration of the outer planet e with 10 Gyr e-folding time. The top panels shows the circulation of the critical angle and the bottom panels show the frequency B defined in the text. In either case, the adiabatic limit is broken, and resonant capture fails.

We also considered the probability of resonance capture from the perspective of Hamiltonian perturbation theory (Appendix 4.6). Importantly, this analysis demonstrates that the resonance widths are sufficiently small that the migration rates required for adiabatic capture are far longer than the system's age, and even in the case of adiabaticity, the capture probability is negligible. We thus conclude that direct capture of planets b, c, and e into a three-body resonance in Kepler-221 is practically impossible.

4.4 Indirect Capture

The results of the previous section lead us naturally to consider indirect forms of capture. In particular, we consider the possibility that libration of the 3-body angle stems from simultaneous libration of 2-body angles facilitated by rapid circulation of ϖ_c. Although the planets in Kepler-221 lie far from exact two-body commensurabilities, previous work (Batygin & Morbidelli, 2013; Pichierri et al., 2019) has shown that libration of resonant angles can be maintained well outside the nominal resonant width, as long as eccentricities are very small. In particular, c and b have period ratio 2.035, wide of a 2:1 resonance, and e and c have period ratio 3.228. There are two choices of critical angle for the 2:1 eccentricity resonance and three for the 3:1 eccentricity resonance, depending on the coefficients of the arguments of periastron. However, if we choose the critical angle

$$\phi_1 = \lambda_b - 2\lambda_c + \varpi_c \tag{4.7}$$

for the 2:1 resonance and

$$\phi_2 = \lambda_c - 3\lambda_e + 2\varpi_c \tag{4.8}$$

for the 3:1 resonance, the linear combination $2\phi_1 - \phi_2$ leads to a cancellation of the arguments of periastron and recovers the three-body critical angle ϕ. In other words, if both two-body resonant angles librate with small amplitudes, the three-body angle will librate as well. In two-body resonances, dissipative evolution results in so-called "resonant repulsion" in which the period ratio increases as energy is liberated (Lithwick & Wu, 2012; Batygin & Morbidelli, 2013). If this mechanism also operates on a resonant chain with period ratios of 1:2:6, a strong damping mechanism could push the planets far wide of their resonances (Pichierri et al., 2019). If the three-body commensurability were also preserved, it could result in a system similar to Kepler-221.

The process of building a resonant chain, characterized by libration of specific harmonics, is sensitive to initial eccentricities and inclination, migration rates, order of assembly, efficiency of eccentricity damping, etc. Ideally, here would model it with an eye towards presenting a self-consistent migration to capture to divergence scenario for Kepler-221's architecture. However, we lack even basic information about the system, such as planet masses. With our estimates, quoted in Table 4.2, we were unable to model this complete evolutionary history of the system because our chosen parameters did not form a 1:2:6 resonant chain under convergent migration. Thus, rather than repeatedly turning knobs, we ask: can this process work in principle? For this, we turn to a simpler toy system using a pair of 2:1 resonances, inspired by the widely known example of a resonant chain in the Galilean satellites of Jupiter. In this case the relevant two-body libration angles are

$$\phi_1 = \lambda_b - 2\lambda_c + \varpi_c \tag{4.9}$$

$$\phi_2 = \lambda_c - 2\lambda_e + \varpi_c \tag{4.10}$$

and the three-body angle is

$$\phi = \phi_1 - \phi_2 = \lambda_b - 3\lambda_c + 2\lambda_e. \tag{4.11}$$

We choose a fiducial system, and allow it to form *some* resonant chain. Then, we study its evolution as an analogy.

To set up the simulation, three planets each of mass $10M_\oplus$ are added at period ratios of 2.02 around a $1M_\odot$ star, with an initial period of 2.8d for the inner planet. We turn on convergent migration for the outer planet with migration timescale 10^6 yr, and eccentricity damping with timescale 10^4 yr. Both effects are implemented with `reboundx` and the eccentricity damping conserves angular momentum (Tamayo et al., 2020b). At $t = 5 \times 10^4$ yr, when each of the three resonant angles ϕ_1, ϕ_2, ϕ are librating, semi-major axis damping is removed and only eccentricity damping is turned on, with $\tau_e = 100$ yr for all three planets. The configuration is integrated for 0.5 Myr, by the end of which the planet pairs are at period ratios of 2.05 and 2.12. All three angles continue to librate. However, given the distance from resonance, the two-body angles are only formally librating, a process that ensues only at very low eccentricities driven by extremely rapid perihelion precession; the two-body resonances in this case are in *forced equilibrium* (Delisle et al., 2012). The three-body commensurability is preserved as a consequence of this forced libration. Slower eccentricity damping, which is probably more realistic, could produce this configuration over longer timescales. Figure 4.4 shows the resultant divergent migration and maintenance of libration. Even though we have not modeled Kepler-221 exactly, we believe that it would behave in the same way, given appropriate initial conditions.

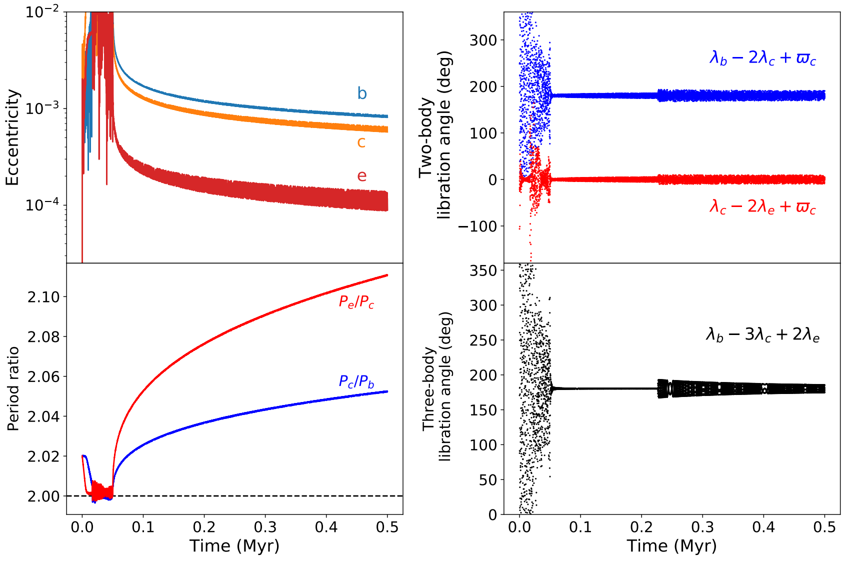

Figure 4.4: Toy model of formation of a Kepler-221-like system involving a pair of 2:1 resonances. Strong eccentricity damping is applied, which increases the period ratio far wide of the original resonances, nevertheless the three key resonance angles remain librating.

Simulations of the toy model above demonstrate that dissipative evolution is confined to the line of three-body commensurability and the orbits spread wide of the original two-body resonances, analogous to the situation for two-planet systems (Lithwick & Wu, 2012). To confirm this mechanism with Kepler-221, we started with the current observed configuration of the system (Table 4.2) and applied eccentricity damping with $\tau_e = 100$ yr. Because dissipative processes are irreversible, the system will not revert to its initial state but rather continue its evolution. The results of this damping simulation, shown in Figure 4.6, demonstrate that energy dissipation increases the period ratios of the resonant planets and preserves the three-body commensurability, even while the individual two-body resonant angles that compose it are not librating (recall that apparent libration far from the commensurability requires the system to lie exactly at the "resonant" focus; even a minute deviation from the global fixed point will result in apparent circulation).

Energy evolution of Kepler-221

The detailed evolutionary history of three-planet systems depends on many factors. However, we can understand it in relatively simple terms by noting that tidal dissipation removes energy but conserves angular momentum. Neglecting interaction terms of $O(m/M_\star)$ (Quillen, 2011), the total orbital energy is

$$E = -GM_\star \left(\frac{m_b}{2a_b} + \frac{m_c}{2a_c} + \frac{m_e}{2a_e} \right). \tag{4.12}$$

The total angular momentum, assuming coplanar and circular orbits, is

$$L = \sqrt{GM_\star} \left(m_b \sqrt{a_b} + m_c \sqrt{a_c} + m_e \sqrt{a_e} \right). \tag{4.13}$$

Angular momentum conservation provides a transformation from three-dimensional semi-major axis space (a_b, a_c, a_e) to two-parameter period ratio space $(n_b/n_c, n_c/n_e)$. Because each point in that parameter space corresponds to three semi-major axes, we can define the scalar function $E(n_b/n_c, n_c/n_e)$. Additionally, in period ratio space, commensurabilities (two- and three-body) become one-dimensional lines. These commensurabilities, as well as the evolution our fiducial model through period ratio space, is shown in Figure 4.5. The primary advantage of the above analysis is that is does not depend on the detailed nature of the energy dissipation. Nevertheless, we can conjecture plausible mechanisms and rule out others.

Tides on the planet generated by eccentric orbits have been shown to be insufficient at reproducing the Kepler population, within which there is an overpopulation of planet pairs $\sim 5\%$ wide of resonance (Lee et al., 2013; Silburt & Rein, 2015). Kepler-221 has been noted as a possible exception to this pattern, but this is because previous studies have classified planets with $R < 2R_\oplus$ as "Earth-like" and assigned optimistic values for the dissipation parameter k_2/Q of $1/100$ (Lee et al., 2013) and $1/40$ (Silburt & Rein, 2015), in addition to assuming a solar-like age of > 5 Gyr. Fortunately, we need not carry out the fully-fledged simulations of dissipation-driven orbital divergence, since the behavior of this process is understood specifically. Tidal dissipation has a characteristic power law growth in which the period ratio is the exact commensurability plus a term that grows as $(t/\tau_e)^{1/3}$. Using this prescription and confirming it with direct simulations, we evolved Kepler-221 including eccentricity damping with $\tau_e = 100$ yr for planet b and found that approximately 7000 cycles of τ_e must have elapsed to reach the present configuration. The damping

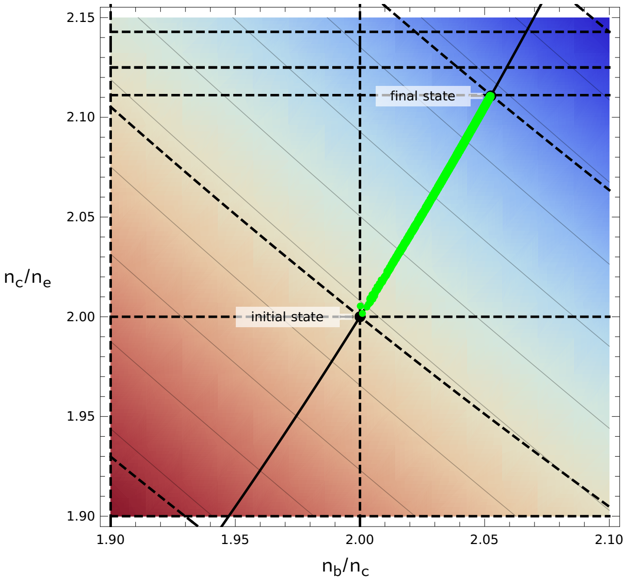

Figure 4.5: Period commensurabilities relevant to our fiducial model where a Kepler-221 analog is initialized in a 1:2:4 resonant chain. In these coordinates, resonances up to the tenth order between planets b and c are represented by vertical dashed lines, c and e by horizontal dashed lines, and b and e by downward-sloping dashed lines. The three-body relation $n_b - 3n_c + 2n_e = 0$ is shown by the upward-sloping black line. Green points show the simulated evolution from Figure 4.4. Thin gray contours and background shading illustrate the total orbital energy, assuming constant angular momentum; energy decreases to the upper right corner.

timescale associated with eccentricity tides is

$$\tau_e = \frac{2}{21 n_b} \frac{Q}{k_2} \frac{m_b}{M} \left(\frac{a_b}{R_p} \right)^5 \tag{4.14}$$

where k_2 is the Love number, Q is the tidal quality factor, R_p is the planet radius. Assuming an optimistic system age of 1 Gyr and the parameters in Table 4.2, we constrain $k_2/Q \gtrsim 1/3$, i.e., an order of magnitude more dissipative than Earth and any body in the Solar System (Murray & Dermott, 1999). Based upon this estimate, we strongly disfavor eccentricity tides as a likely mechanism for driving the long-term orbital divergence of Kepler-221's planets.

Thankfully, there are more efficient variants of tidal dissipation. One possibility is obliquity tides, which can be maintained over long timescales by a secular spin-orbit resonance and require mutual inclination (Millholland & Laughlin, 2019). Kepler-221 is an inclined system, with a minimum mutual inclination of $\sim 7^\circ$, making it an excellent candidate for damping by obliquity tides. We can estimate the dissipation provided by obliquity tides as a feasibility check. Assuming circular orbits, and equilibrium rotation, each planet removes energy at the rate

$$\frac{dE}{dt} = \frac{2 \sin^2 \epsilon}{1 + \cos^2 \epsilon} \frac{3n}{2} \frac{k_2}{Q} \left(\frac{GM^2}{R_p} \right) \left(\frac{R_p}{a} \right)^6 \tag{4.15}$$

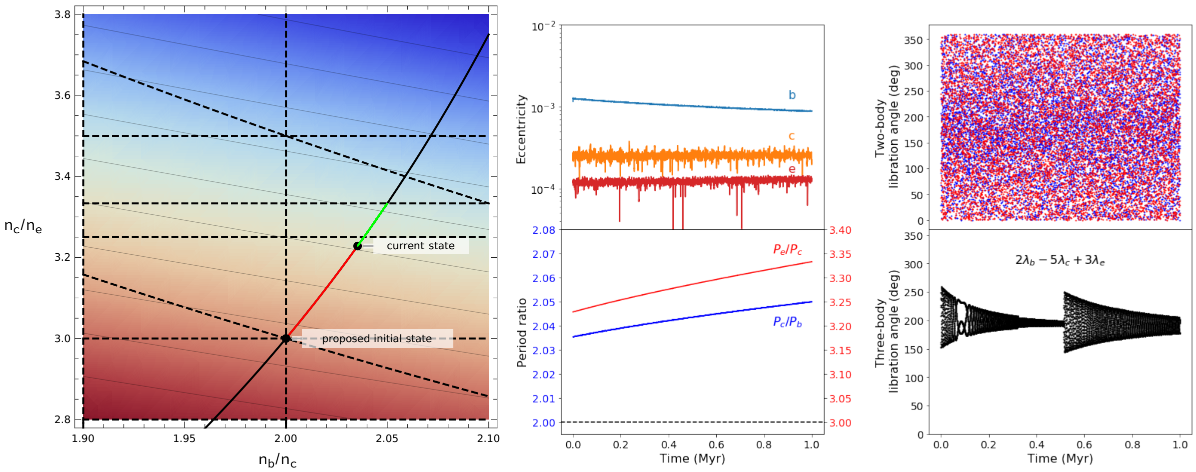

Figure 4.6: Evolution of the Kepler-221 system under eccentricity damping with e-folding time 100 yr acting on each planet, simulating energy dissipation at constant angular momentum. Left panel: period commensurabilities in period-ratio space, analogous to Figure 4.5. Here, the red line marks the evolution between the proposed initial state and the current state of Kepler-221 along the three-body resonance, and green points show the simulated continued evolution. Right panel: period ratios, eccentricity, and resonant angles during the simulated dissipation. The uniform scatter in the two-body resonance angles indicates circulation.

where ϵ is the obliquity of the planet (Millholland & Laughlin, 2019). For typical obliquities driven by the secular spin-orbit resonance the first factor is approximately unity. Taking our optimistic system age of 1 Gyr, the values of k_2/Q needed to damp the energy from the initial to final state are roughly $1/100,000$, $1/50,000$, and $1/100$ assuming damping by only b, c, or e, respectively. The first two values are plausible for super-Earths or sub-Neptunes (Morley et al., 2017; Puranam & Batygin, 2018), while the last is perhaps too high, although considerable uncertainties exist (Efroimsky & Lainey, 2007). Hence, the presence of either planet b or c in an excited obliquity state is sufficient to damp the system to its current state.

Note that in all of these situations, if the migrating planets encounter even a weak two-body resonance, the libration of the three-body angle may break. This is likely because as planets pass through resonance (but do not capture), they experience a jump in semi-major axis. Even a small jump is enough to escape the extremely narrow three-body libration width. For example, in one integration, ϕ began circulating when the outer planets passed through a period ratio of 10:3. The near-instantaneous increase in libration amplitude in Figure 4.6 is also likely due to an encounter with a very high order resonance. Therefore, a necessary condition for the initial and final state of a system like Kepler-221 is that there is no remotely strong intervening two-body resonance. An initial state corresponding to 2:1 and 3:1 resonances fulfills this criterion, as there are no two-body resonances of order ≤ 10 and no zeroth-order three-body resonances with $p, q \leq 10$ in between the 1:2:6 initial state and the current period ratios of Kepler-221 (Figure 4.6).

Radius Inflation

If indeed Kepler-221b is experiencing a large amount of tidal dissipation, the heat flux may affect the atmosphere. Here, we build a simplified atmospheric model to show that even a low-mass envelope can expand to a large size and cause a super-Earth type planet to lie within the radius gap. The model we aim to construct is merely illustrative. Thus, for definitions, we assume that the atmosphere is purely hydrogen, is in hydrostatic equilibrium, and obeys a polytropic equation of state, $P = k\rho^{1+\gamma}$ with $\gamma = 7/5$, implying a nearly fully convective envelope. We further assume the ideal gas law with an equilibrium temperature of 1120 K, computed with an albedo of 0.3. The energy transfer equation at the radiative-convective boundary R_{RCB} is

$$\frac{L}{4\pi R_{RCB}^2} = \frac{16}{3}\left(\frac{\sigma T^3}{\kappa \rho_{RCB}}\right)\frac{dT}{dr} \tag{4.16}$$

where L is the internal luminosity, σ is the Stefan-Boltzmann constant, κ is the opacity (for which we use 0.1 cm^2/g), and $dT/dr \approx g/c_P$ is the adiabatic lapse rate, where g is the surface gravity and $c_P \approx 7R/2$ is the specific heat capacity at constant pressure.

We then solve the hydrostatic equation for a variety of core masses and luminosities to obtain $\rho(r)$. Assuming the atmosphere sits atop a solid core of mass M_c, density 4 $\mathrm{g/cm}^3$, and radius R_c, the atmospheric mass is

$$M_{\text{env}} = \int_{R_c}^{1.7R_E} 4\pi\rho(r)r^2 dr. \tag{4.17}$$

The atmospheric mass relative to the mass of the core of the planet is shown in Figure 4.7. We assume the luminosity is greater than that due to the heat of formation,

$$L_{\min} \approx \frac{GM_{\text{env}}M_c}{(1.7R_E)^2\mathcal{T}} \tag{4.18}$$

where $\mathcal{T} \approx 600$ Myr is the age of the system. If the luminosity is indeed near 3×10^{13} W as we predict, envelope fractions as small as 10^{-4} or 10^{-5} would be sufficient to yield a total radius of $1.71R_E$.

One hypothesis to explain the radius gap is photoevaporation (Fulton et al., 2017). In this scenario, FUV flux in the early life of the star blows off the tenuously-held atmosphere, leaving behind bare cores. In the case of Kepler-221b, however, a truly bare core is unlikely. Outgassing (which is likely to be enhanced by internal heating) provides a continuous supply of gas which will promptly be inflated to a large radius. Estimating the degree of outgassing is outside the scope of this chapter because it depends strongly on the mass and composition of the planet, but we emphasize that an atmospheric mass of only $\sim 10^{-4}M_\oplus$ is sufficient.

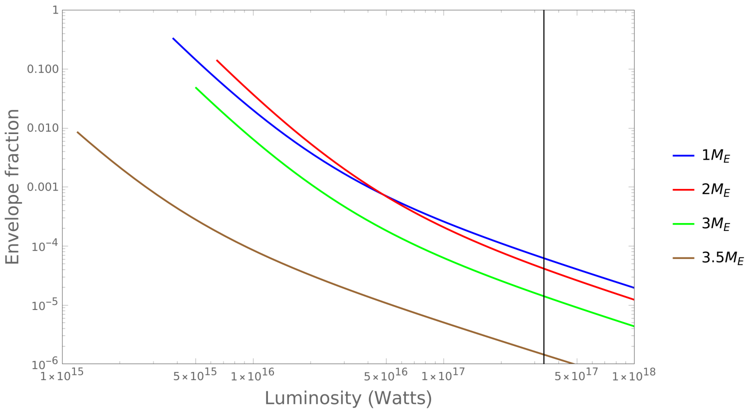

Figure 4.7: The mass fraction of the hydrogen envelope needed to produce a planet of radius $1.71R_E$ as a function of tidal luminosity, for four different core masses. Each line begins at the luminosity from the heat of formation; the black vertical line is the estimated tidal luminosity of Kepler-221b.

4.5 Discussion

In this work, we have considered the origins of the remarkable orbital architecture of Kepler-221, and have argued that a sensible evolutionary history for this system is one where the planets originated in a resonant chain and experienced long-range orbital divergence, thanks to the action of persistent tidal damping. Moreover, our analysis points specifically to obliquity tides as the primary dissipative process at play.

Although we have presented a general overview of a mechanism to produce Kepler-221, our model is incomplete. A detailed description would require knowledge of the planets' masses, which critically affect resonant dynamics, as well as mutual inclinations, which are necessary for the spin-orbit resonances that drive obliquity tides. We leave these issues to future work, as the system architecture comes into sharper focus.

Previous studies of the role of tidal dissipation in shaping multiplanet systems have discussed the statistical imprint of different dissipation mechanisms on planetary architectures. Typically, they assume that near resonant planet pairs began in exact commensurabilty and migrated outwards (Lee et al., 2013; Silburt & Rein, 2015; Millholland & Laughlin, 2019). While this picture can explain planet pairs wide of resonance (provided sufficient dissipation) it is possible that some of the planetary systems formed in place and found the resonant equilibrium through eccentricity damping (Pichierri et al., 2019). However, systems with complex overlapping resonances, and in particular Kepler-221, require convergent migration and assembly at exact commensurability before divergent migration driven by dissipation, and therefore provide stronger constraints on tidal mechanisms.

If tides in one of the planets is responsible for the energy dissipation in Kepler-221, and that dissipation is still occurring, it would provide a significant internal energy source for that planet and inflate its radius. Indeed, an unusual degree of dissipation could explain why planet b has a radius lying within the radius gap of Fulton et al., 2017, typically assumed to be carved by photoevaporation. Confirmation of this hypothesis would likely require precise mass measurements of Kepler-221b because the degree of inflation depends strongly on the envelope fraction of the planet (Millholland, 2019). Nevertheless, the model outlined in this work presents a testable framework for understanding the anomalous architecture of the Kepler-221 planetary system.

4.6 Appendix

Hamiltonian Capture Probability

A Hamiltonian prescription lends itself well to studying capture into mean-motion resonances via migration. The Hamiltonian for a pure three-body resonance was derived by Quillen, 2011. For details we direct the reader to that work, but we will simply copy the relevant formulae here. For generality, we use i, j, k as labels for the three planets. As mentioned in the main text, the relevant critical angle is

$$\phi = p\lambda_i - (p+q)\lambda_j + q\lambda_k \tag{4.19}$$

and its conjugate momentum is simply $J = \Lambda_i/p$, where $\Lambda_i = m_i\sqrt{GMa_i}$. The Hamiltonian is most simply expressed by defining $J \equiv J_0 + I$ and expanding about J_0. Then, it takes the form of a pendulum,

$$\mathcal{H}(I,\phi) = \frac{1}{2}AI^2 + BI + \epsilon_{pq}\cos\phi \tag{4.20}$$

where, as before,

$$B = pn_i - (p+q)n_j + qn_k, \tag{4.21}$$

and

$$A = -3\left(\frac{p^2}{m_i a_i^2} + \frac{(p+q)^2}{m_j a_j^2} + \frac{q^2}{m_k a_k^2}\right) \tag{4.22}$$

$$\begin{aligned}\epsilon_{pq} \approx \frac{m_i m_j m_k^3}{\Lambda_k^2}\Bigg[&\frac{3n_j^2}{2}\left(\frac{1}{2n_{ij}n_{jk}} + \frac{p}{qn_{ij}^2} + \frac{q}{pn_{jk}^2}\right) b_{1/2}^p(\alpha_{ij}) b_{1/2}^q(\alpha_{jk}) \\ &+ \left(\frac{n_j}{n_{jk}} + \frac{qn_j}{pn_{ij}}\right) b_{1/2}^q(\alpha_{jk})(1+\alpha_{ij}D_\alpha) b_{1/2}^p(\alpha_{ij}) \\ &+ \left(\frac{n_j}{n_{ij}} + \frac{pn_j}{qn_{jk}}\right) b_{1/2}^p(\alpha_{ij})\alpha_{jk}D_\alpha b_{1/2}^q(\alpha_{jk})\Bigg].\end{aligned} \tag{4.23}$$

Here, n_i, n_j, n_k are the mean motions, and $n_{ij} = n_i - n_j$ and $n_{jk} = n_j - n_k$. Also, $\alpha_{ij} = \frac{a_i}{a_j}$ and $\alpha_{jk} = \frac{a_j}{a_k}$, $b_{1/2}^p$ is the Laplace coefficient and D_α is the derivative with respect to α. We note that the exponential approximations for $b^p_{1/2}$ provided in Quillen, 2011 are not sufficient for Kepler-221 because the values of α_{ij} are too far from 1. Exact expressions involving elliptic integrals are tractable in this low-order case.

Some key properties of the resonance can now be estimated. The libration frequency is

$$\omega_{pq} \sim \sqrt{\epsilon_{pq} A} \tag{4.24}$$

and the width of the resonance in semi-major axis space is

$$\Delta a \sim \frac{4p}{m}\sqrt{\frac{2\epsilon_{pq} a}{A}} \propto ma \tag{4.25}$$

where m is the planet-star mass ratio. Note, in contrast, the width of a first-order two-body (eccentricity) resonance, such as the one introduced in Section 4.2, is $\Delta a \propto \sqrt{m}a$.

Resonance capture is much more likely if the migration is adiabatic. A reasonable criterion for this is that the timescale of migration across the resonance should exceed the timescale of libration. Consider a planet migrating with semi-major axis e-folding time τ_a. Then, the timescale for crossing the resonance is

$$\Delta t = \frac{\Delta a}{\dot{a}} = \frac{\tau_a \Delta a}{a}. \tag{4.26}$$

The adiabatic criterion is therefore

$$\frac{\Delta t}{P_{\text{lib}}} = \frac{\tau_a \Delta a \omega_{pq}}{2\pi a} \gg 1. \tag{4.27}$$

Figure 4.8 shows this criterion for estimated values of the Kepler-221 system. Typical migration rates within a protoplanetary disk are $\sim 10^5$ yr or less. Hence, the crossing of this three-body resonance in that scenario could not feasibly have happened adiabatically for the Kepler-221 system due to the narrowness of the resonance. There are mechanisms in which the planets could migrate much more slowly. Even then, the capture rates, as estimated from adiabatic capture theory (Henrard, 1982), are vanishingly low, as shown in Figure 4.9.

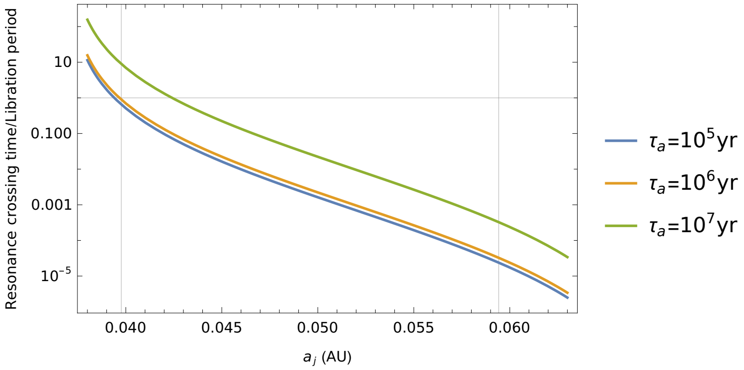

Figure 4.8: Adiabatic criterion (resonance crossing time/libration period) as a function of semi-major axis of the second planet in Kepler-221. The left vertical gray line marks a 5 Hill radius spacing, inside of which stability is unlikely. The right vertical gray line marks the current position of Kepler-221c.

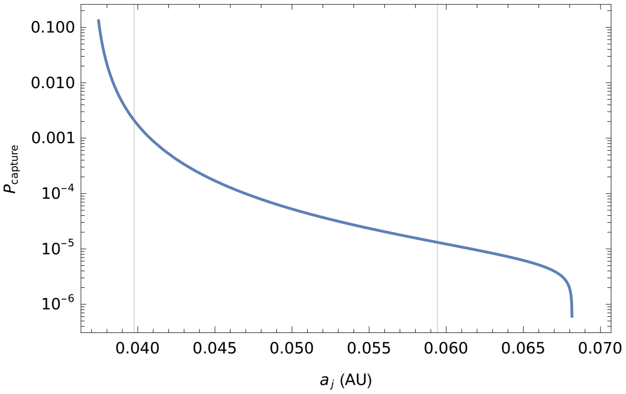

Figure 4.9: Probability of capture into a pure three-body resonance, assuming the adiabatic capture theory. Vertical gray lines mark the same as in Figure 4.8.

Chapter 5

DYNAMICS AND ORIGINS OF THE NEAR-RESONANT KEPLER PLANETS

Goldberg, M. & Batygin, K. (May 2023). “Dynamics and Origins of the Near-resonant Kepler Planets.” In: *The Astrophysical Journal* 948, p. 12. ISSN: 0004-637X. DOI: `10.3847/1538-4357/acc9ae`.

5.1 Introduction

The architectures of multiplanet systems hold crucial clues to their formation and evolution. Conditions of the protoplanetary disk leave deep imprints on individual and statistical properties of these planets and systems (Lee & Peale, 2002; Adams et al., 2008; Lee et al., 2013; Millholland, 2019). Although the process of planet formation itself remains difficult to observe directly, the galactic planetary census is now broad enough to employ as a population-level testing ground for models of planetary formation (Mordasini et al., 2015).

One distinct feature is mean-motion resonances: although most exoplanets are not near resonance, the small fraction that *are* resonant imply that dissipative processes play an important role in at least those systems (Batygin, 2015). This small degree of certainty in their formation makes it possible to build more robust models incorporating other physical processes. Notably, numerous physical effects have been invoked to explain the unexpected phenomenon in which adjacent exoplanets tend to lie slightly wide of, rather than exactly on, mean-motion resonances (Delisle et al., 2012; Fabrycky et al., 2014; Terquem & Papaloizou, 2019; Choksi & Chiang, 2020).

From a distinct point of view, near-resonant planets offer a unique opportunity to measure planetary masses and orbital elements normally invisible to transiting exoplanet surveys. When the ratio of orbital periods of adjacent planets is close to a ratio of small integers, planet-planet interactions are coherent and become amplified. The slight changes to the Keplerian orbits manifest as deviations from exact periodicity in the arrival of transits (Agol et al., 2005). Inverting the transit timing variation (TTV) signal to produce mass and orbital constraints is nontrivial and subject to several degeneracies (Lithwick et al., 2012; Hadden & Lithwick, 2016). Nevertheless, TTVs have routinely provided useful constraints on mass and orbits of small planets not amenable to radial velocity observations (Hadden & Lithwick, 2014; Agol et al., 2021).

Together, the special properties of near-resonant systems offer a unique opportunity to take precise measurements and use those constraints to reliably study their origin. Recently, studies of a small subset of resonant giant planets have produced possible histories of migration and constraints on the behavior of the inner disk (Hadden & Payne, 2020; Nesvorný et al., 2022). By extending this type of analysis to small planets and a much larger sample, we can test whether a given physical process acting in the late stage of planet formation could conceivably reproduce the current sample.

In Section 5.2, we review the basics of first-order mean-motion resonance from a Hamiltonian perspective. In Section 5.3, we summarize the key properties of TTVs and then analyze the resonant structure of the *Kepler* TTV sample. Section 5.4 tests four general models of the formation of near-resonant systems against our new constraints. We identify possible biases and possible future work in Section 5.5, and summarize our results in Section 5.6.

5.2 Mean-motion Resonance

We begin with a brief overview of the Hamiltonian formulation of a first-order mean-motion resonance. To first order in planet masses and eccentricities, the Hamiltonian for a pair of planets near a $k{:}k-1$ resonance is

$$\begin{aligned}\mathcal{H} = -\frac{\mathcal{G}M_*m_1}{2a_1} - \frac{\mathcal{G}M_*m_2}{2a_2} - \frac{\mathcal{G}m_1m_2}{a_2}\\ \times[fe_1\cos(k\lambda_2-(k-1)\lambda_1-\varpi_1)\\ +ge_2\cos(k\lambda_2-(k-1)\lambda_1-\varpi_2)]\end{aligned} \tag{5.1}$$

where m, a, e, λ, and ϖ are the planet mass, semi-major axis, eccentricity, mean longitude, and longitude of pericenter, respectively (Batygin, 2015). Additionally, $\mathcal{G}$ is the gravitational constant, M_* is the mass of the central star, and f and g are order-unity constants that depend on the resonant index (see, e.g., Deck et al., 2013). The two angles that appear as arguments of the cosines are referred to as "resonant angles," and we will refer to them as ϕ_1 and ϕ_2, respectively. After a series of rescalings and canonical transformations that identify three conserved quantities, Eq. 5.1 can be reduced to an integrable Hamiltonian with just one degree-of-freedom,

$$\tilde{\mathcal{H}} = 3(\delta+1)\tilde{\Psi} - \tilde{\Psi}^2 - 2\sqrt{2\tilde{\Psi}}\cos(\psi). \tag{5.2}$$

Here, ψ is the coordinate and $\tilde{\Psi}$ is its conjugate momentum. Specifically,

$$\psi = k\lambda_2 - (k-1)\lambda_1 - \hat{\varpi} \tag{5.3}$$

where $\hat{\varpi}$ is a generalized longitude of pericenter, most easily expressed using complex eccentricities (Hadden, 2019)[1]:

$$\hat{\varpi} = \mathrm{Arg}(fe_1e^{\iota\varpi_1} + ge_2e^{\iota\varpi_2}). \tag{5.4}$$

---

[1] One can also write this equation as $\tan\psi = \frac{fe_1\sin\phi_1+ge_2\sin\phi_2}{fe_1\cos\phi_1+ge_2\cos\phi_2}$ (Laune et al., 2022).

We will refer to ψ as the "mixed resonant angle." Finally, δ is a dimensionless constant that determines the topology of the Hamiltonian. Its form as derived in Batygin, 2015 is unwieldy but can be simplified dramatically in the compact orbits approximation, i.e., $k \approx k-1$, $a_1/a_2 \rightarrow 1$, $-f \approx g \approx 0.8k$ (Deck & Batygin, 2015). In that case, δ takes the form

$$\delta \approx -1 + \frac{1}{3}\left(\sigma^2 - \frac{2\Delta}{3k}\right)\left[\frac{15kM_*}{4(m_1+m_2)}\right]^{2/3} \tag{5.5}$$

where

$$\sigma^2 = e_1^2 + e_2^2 - 2e_1e_2\cos(\varpi_2 - \varpi_1) \tag{5.6}$$

is a generalized eccentricity and Δ is the normalized distance to exact resonance defined in terms of the inner and outer periods P_1 and P_2 (e.g., Lithwick et al., 2012),

$$\Delta = \frac{P_2}{P_1}\frac{k-1}{k} - 1. \tag{5.7}$$

Additionally, in this approximation the action takes the form

$$\tilde{\Psi} \approx \frac{1}{2}\sigma^2\left[\frac{15kM_*}{4(m_1+m_2)}\right]^{2/3} \tag{5.8}$$

and the generalized longitude of pericenter is

$$\hat{\varpi} \approx \mathrm{Arg}(e_1e^{\iota\varpi_1} - e_2e^{\iota\varpi_2}). \tag{5.9}$$

We will use the unapproximated forms of δ and $\hat{\varpi}$ unless indicated otherwise.

Hamiltonian 5.2 has one, two, or three equilibria, depending on δ. In all cases, there is a stable equilibrium point at $\psi = \pi$; this is the sole equilibrium for $\delta < 0$. At $\delta = 0$ another equilibrium appears, and for $\delta > 0$ it splits into a stable and unstable equilibrium, both of which have $\psi = 0$. The dynamical regime of the system can be categorized according to these fixed points. One regime is "libration," in which ψ oscillates around 0 or π in a bounded interval smaller than $[0, 2\pi]$. Inversely, "circulation" indicates that ψ eventually takes on every value from $[0, 2\pi]$. Libration and circulation of a resonant angle are sometimes taken to be equivalent to being "in resonance" and "nonresonant," respectively. However, resonance is in fact only *formally* defined when the Hamiltonian has a separatrix that divides resonant and nonresonant trajectories, which only occurs when $\delta > 0$ (Henrard & Lemaitre, 1983; Delisle et al., 2012). Correspondingly, true resonant dynamics only occur for libration of ψ around π when $\delta > 0$.

5.3 Transit Timing

Overview of TTVs

Transit timing variations (TTVs) have proven to be an especially powerful tool in investigating the dynamics of near-resonant planetary systems. TTVs have been widely used to characterize planetary systems beyond what is obtainable from strictly periodic transits alone and sample posterior distributions of planet masses, eccentricities, and other orbital elements (Agol et al., 2021, and references therein). In principle, one could use these samples to compute the posterior distributions of the resonant angles in Hamiltonian 5.1 for each system. In practice, however, the distributions of ϕ_1 and ϕ_2 are typically very broad and uninformative.

The reason for this limitation is that there are fundamental degeneracies in inverting TTV data. For example, the approximate first-harmonic TTV amplitude derived by Hadden & Lithwick, 2016 for the inner planet in a near-resonant pair is

$$\delta t_{\mathcal{F}} \sim \frac{m_2 P_1}{2\pi M_* |\Delta|} \cdot \max\left\{1, \frac{|\mathcal{Z}|}{|\Delta|}\right\} \tag{5.10}$$

where

$$\mathcal{Z} = \frac{f e_1 e^{\iota\varpi_1} + g e_2 e^{\iota\varpi_2}}{\sqrt{f^2 + g^2}} \tag{5.11}$$

is a combined complex eccentricity relevant to the dynamics.[2] Higher order TTV signals still depend on planet eccentricities only through the combination $\mathcal{Z}$ rather than the individual planet eccentricities (Hadden & Lithwick, 2016).[3] As a result, while $\mathcal{Z}$ is often well-constrained, ϖ_1 and ϖ_2 are rarely independently measured and the libration or circulation behavior of ϕ_1 and ϕ_2 cannot be determined (e.g., Petigura et al., 2018; Petigura et al., 2020). The analytical results of Hadden & Lithwick, 2016 only apply to near-resonant systems that are not actually in resonance. Nevertheless, Nesvorný & Vokrouhlický, 2016 find that TTVs for planets in resonance also depend only on $\mathcal{Z}$.

However, a precise measurement of $\mathcal{Z}$ *does* allow for a direct measurement of $\hat{\varpi}$, because, from Eq. 5.4, $\hat{\varpi} = \mathrm{Arg}\mathcal{Z}$. Thus, the dynamically relevant mixed resonant angle ψ can be calculated. Remarkably, while TTV data typically cannot determine the full planetary orbits, they can constrain the parameters of the mean-motion resonance. The ability of TTV data to precisely measure ψ has been used previously to study the resonant behavior in a few systems (Hadden & Lithwick, 2017; Petit et al., 2020a). Here, we apply it on a population level to study many near-resonant pairs in a uniform way.

Observed TTV Systems

Our sample is the near-resonant pairs of planets from *Kepler* studied by Hadden & Lithwick, 2017 and Jontof-Hutter et al., 2021. Each work ran N-body models to fit transit times of *Kepler* systems and derived the mass, orbital period, time of midtransit, and eccentricity vector of each planet

---

[2] Note that $|\mathcal{Z}| \approx \sigma/\sqrt{2}$ in the compact approximation.

[3] The exception is the 2:1 resonance, where the second-harmonic TTV can individually constrain eccentricities (Hadden & Lithwick, 2016).

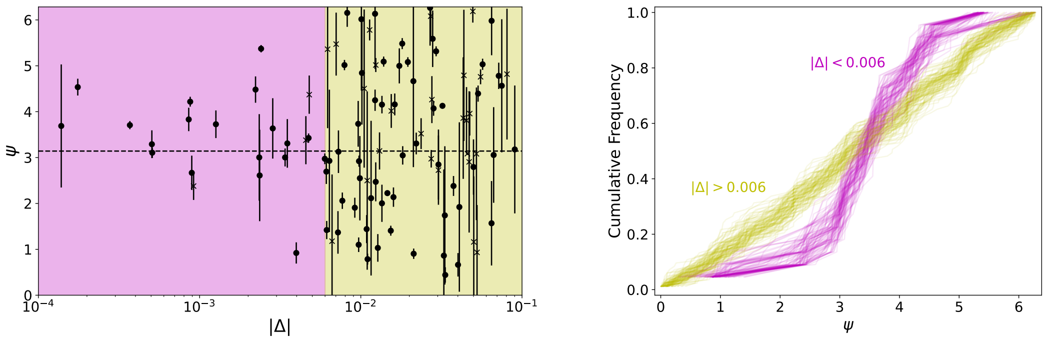

Figure 5.1: The osculating mixed resonant angle ψ for the 108 pairs of planets near first-order resonances characterized in Hadden & Lithwick, 2017 and Jontof-Hutter et al., 2021. Left: Distance from exact resonance Δ versus ψ. Dots mark pairs outside of exact resonance ($\Delta > 0$) and crosses mark pairs inside ($\Delta < 0$). Error bars are 1σ circular standard deviations. The resonant equilibrium at $\psi = \pi$ is shown with a horizontal dashed line. Right: Cumulative distributions of ψ for the systems nearest to resonance ($|\Delta| < 0.006$, in maroon), and the more distant systems ($|\Delta| > 0.006$, in yellow). In both cases, 100 CDFs are plotted by drawing from the posterior distribution of ψ for each planet pair.

(orbits are assumed to be planar). We use their Markov Chain Monte Carlo posterior distributions of those parameters. If a planet pair was fit by both works, we use the posteriors from Hadden & Lithwick, 2017. We remove planet pairs near second-order resonance (which have a different Hamiltonian) and pairs with $|\Delta| > 0.1$, leaving 105 unique planet pairs in the joint sample. Of these, 40 are near the 2:1 resonance, 37 are near the 3:2 resonance, and the rest are near higher-index first-order resonances. We use the default set of mass/eccentricity priors from Hadden & Lithwick, 2017 for the following analysis, but checked that the results are the same for their alternative "high mass" priors.

For each of these planet pairs, we compute the osculating value of ψ from the posterior distributions using Eqs. 5.3 and 5.4. The results are shown in Figure 5.1, where ψ has been plotted against $|\Delta|$. Uncertainties on ψ are computed using a circular standard deviation and are an average of ~ 3 times smaller than the uncertainties on ϕ_1 and ϕ_2. Figure 5.1 clearly shows two regimes: for $|\Delta| \lesssim 0.006$, ψ is clustered around π. For $|\Delta| \gtrsim 0.006$, ψ is uniformly distributed on $[0, 2\pi]$.[4]

To confirm that these are indeed distinct distributions and not the result of a small sample size or measurement uncertainty, we randomly drew one value of ψ from the posterior of each planet pair to construct two empirical cumulative distribution functions (CDFs) for pairs with $|\Delta| < 0.006$ and $|\Delta| > 0.006$. We then used the two-sample Kuiper test implemented by the `astropy` package

---

[4] The code for these and all following calculations is available at `https://github.com/goldbergmax/resonant-capture-simulation`.

to compute a false alarm probability (FAP) that these two samples were drawn from the same distribution. Repeating this process 10,000 times, we found that the median FAP was 0.0063. The right panel of Figure 5.1 is a representation of 100 of these empirical CDFs in each range of Δ. Although the CDFs of the planet pairs with $|\Delta| > 0.006$ seem to follow a uniform distribution, the pairs nearest to resonance show a clear kink in the distribution near π.

We noted in Section 5.2 that resonant trajectories are only formally defined if a separatrix exists, equivalent to $\delta > 0$. Is this the case for the systems in Figure 5.1? In the compact limit (see Section 5.2) and assuming the system is at the stable equilibrium, the condition for the existence of a separatrix is

$$\Delta < \Delta_{\text{crit}} \approx \frac{3}{2}\left(\frac{4}{15}\frac{m_1+m_2}{M_*}\right)^{2/3} k^{1/3}. \tag{5.12}$$

As a typical near-resonant *Kepler* system, we will assume $m_1 \approx m_2 \approx 10M_\oplus$, $M_* \approx M_\odot$, and $k \approx 3$. For this "fiducial" system, Eq. 5.12 gives $\Delta_{\text{crit}} \approx 0.001$. This boundary is narrower than the break seen in Figure 5.1, and indicates that the vast majority of our sample cannot strictly be resonant, regardless of ψ (Delisle et al., 2012). Interesting, clustering persists beyond Δ_{crit} up to ≈ 0.006, suggesting that libration exists in some formally nonresonant systems.

The resonant dynamics also induce a forced eccentricity on the pair of planets (Lithwick et al., 2012). That is, the stable equilibrium of Hamiltonian 5.2 implies a nonzero value of σ for $\Delta > 0$. By solving the equilibrium equation for the Hamiltonian in the compact limit, one obtains

$$\sigma_{\text{eq}} = \frac{4}{5\Delta}\frac{m_1+m_2}{M_*}. \tag{5.13}$$

A similar expression can be derived for the 2:1 resonance, and in that case the forced eccentricity is a factor of ~ 2 smaller than Eq. 5.13 (Lithwick et al., 2012).

Figure 5.2 shows the observed $|\mathcal{Z}|$ for the TTV sample compared to the forced eccentricity $|\mathcal{Z}_{\text{eq}}| \approx \sigma_{\text{eq}}/\sqrt{2}$. Some eccentricities are not robustly measured and the positive definite nature of $|\mathcal{Z}|$ can introduce a bias. Following Hadden & Lithwick, 2017, if the projection of the measured $\mathcal{Z}$ onto the median of its distribution is consistent with 0 at the 1σ level (true for about 25% of systems), we report only upper limits on $|\mathcal{Z}|$. The observed eccentricities exceed the equilibrium forced value in most cases, often by an order of magnitude, except when $|\Delta| \lesssim 0.006$. In the context of Hamiltonian 5.2, a free eccentricity exceeding the forced eccentricity implies that the $(\tilde{\Psi}, \psi)$ phase space trajectory circumnavigates the origin and hence ψ is in circulation. Random draws of ψ from a circulating population will be distributed almost uniformly. Thus, the distribution of ψ in Figure 5.1 is consistent with the observed $|\mathcal{Z}|$.

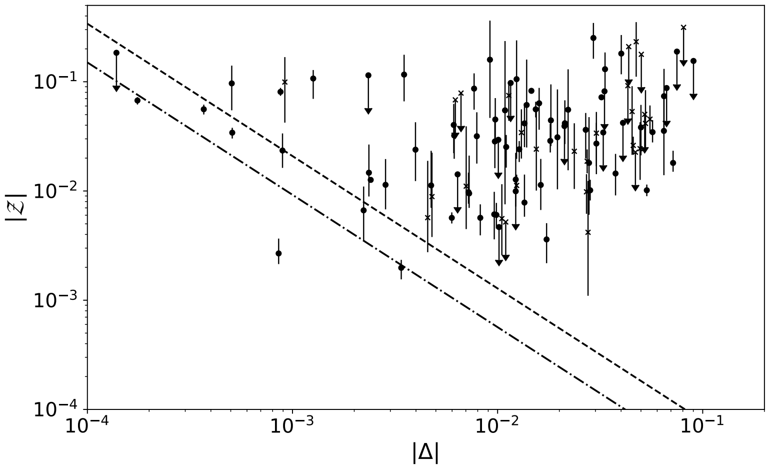

Figure 5.2: The norm of the generalized eccentricity $\mathcal{Z}$ as a function of distance from resonance Δ for the TTV systems. As in Figure 5.1, circles and crosses mark pairs outside and inside of the resonance, respectively. For well-measured eccentricities, error bars are 1σ uncertainties, otherwise 2σ upper limits are plotted. The dashed and dash-dotted lines are the equilibrium forced eccentricities in the compact limit and for the 2:1 resonance, respectively (Eq. 5.13).

Aside: Pitfalls of Determining Libration with Standard Resonant Angles

While we have demonstrated that the mixed resonant angle ψ is a valuable tool for studying near-resonant systems, it is worth emphasizing that considering only ϕ_1 and ϕ_2 as derived from TTV data can be deeply misleading. As an example, consider a coplanar pair of $10M_\oplus$ planets around a solar mass star with initial conditions $P_1 = 2$ d, $P_2 = 3$ d, $\lambda_1 = \lambda_2 = 0$, and complex eccentricities $e_1 = 0.02 \cdot e^{\iota 0}$, $e_2 = 0.02 \cdot e^{\iota \pi}$. By numerically integrating this sytem with `rebound`, we find that the 3:2 resonant angles ϕ_1, ϕ_2, ψ all librate with small amplitudes and the transit times vary by ~ 30 min over the resonant libration cycle (left column of Figure 5.3).

Now suppose we construct a similar system (represented by primed coordinates) where we translate the complex eccentricities by some complex number ξ so that $e_1' = e_1 + \xi$ and $e_2' = e_2 - (f/g)\xi$. All other orbital elements are left untouched. Hamiltonian 5.2 is invariant under such a transformation because $\tilde{\Psi}$ and ψ depend on the eccentricities only through a linear combination in which ξ cancels. Likewise, $|\mathcal{Z}|$ remains unchanged. The right panel of Figure 5.3 shows the evolution of the transformed system, where we have arbitrarily chosen $\xi = 0.1 \cdot e^{\iota\pi/2}$. As expected, ψ' librates and the TTV signal is nearly identical. However, ϕ_1' and ϕ_2' are now in circulation, so an analysis which only computed these angles would classify this system as "nonresonant." In general, TTV fits cannot distinguish between these two configurations (Leleu et al., 2021b) and therefore they frequently recover both librating and circulating solutions to the same data, even if ψ librates across nearly all of the allowed entire parameter space (Dai et al., 2023).

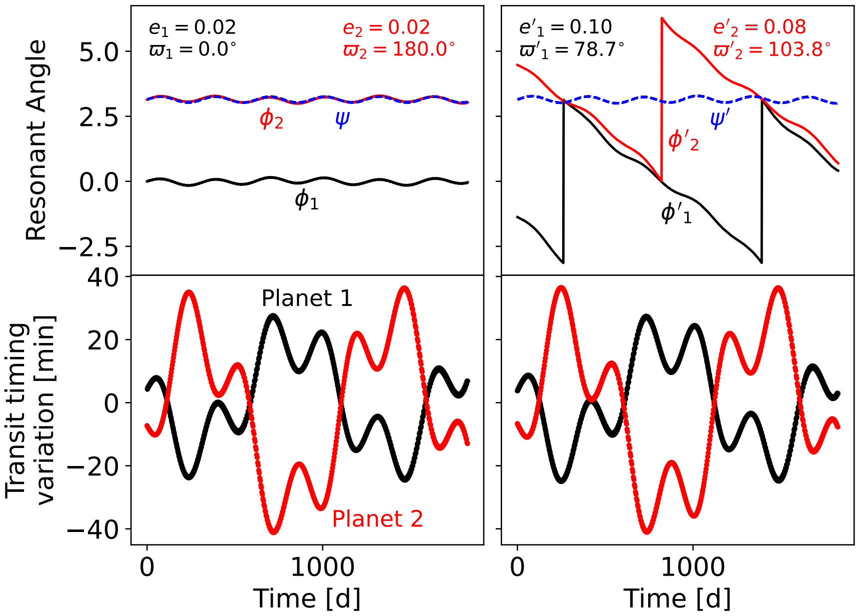

Figure 5.3: An example of the impact of two eccentricity configurations (left and right columns) on TTVs and inferred resonant angles. In the top row, the black and red lines are the standard resonant angles ϕ_1 and ϕ_2, respectively, while the dashed blue line is the mixed angle ψ. The bottom row shows the observed minus calculated transit times for the inner and outer planet in black and red. Without additional information, TTV fits cannot distinguish between the two cases and often recover solutions where ϕ_1 and ϕ_2 circulate even if the system is resonant.

For completeness, we note that there are some ways to distinguish between the systems in the left and right columns of Figure 5.3. Higher-order resonant terms and secular evolution depend on different combinations of the eccentricities, so higher-precision or longer baseline TTV measurements can break the degeneracy. The most eccentric solutions can also be eliminated via dynamical stability tests. Finally, transit durations can directly measure $e \sin \varpi$ for well-understood systems (Van Eylen & Albrecht, 2015). Photodynamical analyses that incorporate all of these strategies can provide excellent constraints on resonant behavior, for example in K2-19 (Petigura et al., 2020; Petit et al., 2020a). The problem can also be avoided altogether in systems of three or more planets by considering zeroth-order Laplace angles that depend only weakly on eccentricity (Siegel & Fabrycky, 2021).

5.4 Migration History of Near-Resonant Systems

Early on in the *Kepler* mission, an excess of planet pairs just outside of first-order resonances was identified (Lissauer et al., 2011; Fabrycky et al., 2014). The effect is most striking near the 2:1 and 3:2 commensurabilities, where there is a distinct peak at $\Delta \sim 1\%$ and a trough inside the exact

Model	Controlling Parameter	Parameter Range
Laminar disk	Damping ratio $K \equiv \tau_a/\tau_e$	$[10^2, 10^5]$
Turbulent disk	Stochastic force strength κ	$[10^{-7}, 10^{-5}]$
Tidal damping	Cumulative e damping timescales	$[10^{-1}, 10^2]$
Planetesimal damping	Planetesimal disk mass M_d	$[10^{-1}, 10^1]$ $M_\oplus$

Table 5.1: An overview of our population synthesis models and the parameters that control their evolution.

resonance (Weiss et al., 2022). There is considerable literature on this topic, and explanations of this unexpected feature have broadly fallen into two categories.

The first idea argues that the departure from resonance occurs during the migration phase within the gaseous disk. As a pair of planets capture into resonance in the protoplanetary nebula, the orbital periods reach an equilibrium value of Δ that is set by the disk properties (Terquem & Papaloizou, 2019). Various disk models and parametrizations have been found to match the distribution of period ratios wide of resonance (Choksi & Chiang, 2020).

The second idea argues alternatively that the distancing from resonance occurs after the disappearance of the protoplanetary disk. Early theoretical studies noted that a near-resonant pair of planets, under some form of energy dissipation that conserves angular momentum, will "repel," and the orbital period ratio will increase (Lithwick & Wu, 2012; Batygin & Morbidelli, 2013; Pichierri et al., 2019). Thus, an initial population near exact resonance that is subjected to energy dissipation (e.g., eccentricity damping) will naturally form the trough and peak inside and outside the resonance, respectively. Several sources of dissipation have been suggested, including tides due to orbital eccentricity (Delisle & Laskar, 2014), tides due to planetary obliquity (Millholland & Laughlin, 2019), and damping from leftover planetesimals, which can also drive divergent migration (Chatterjee & Ford, 2015).

We argue here that many of these models cannot explain the results of Section 5.3. The fundamental issue is that they invoke strong energy dissipation to grow Δ, a process that will invariably cause the systems to settle into their equilibrium with small free eccentricity and librating ψ. That configuration is robustly ruled out by our analysis of the TTV sample in Figures 5.1 and 5.2. To demonstrate this, we built four simplified population synthesis models based on published hypotheses for the *Kepler* near-resonant systems, summarized in Table 5.1. Of them, stochastic forces present during disk migration best replicate the trends observed in Section 5.3.

Laminar Disk Migration

Several authors (e.g., Choksi & Chiang, 2020; Charalambous et al., 2022) have invoked disk migration and capture into resonance as the dominant physical processes that produce the near resonant pairs. Typically, each planet is assigned a semi-major axis and eccentricity damping timescale, $\tau_{a,i} = a_i/\dot{a}_i$, and $\tau_{e,i} = e_i/\dot{e}_i$, respectively. In the case of convergent migration with eccentricity damping (i.e., $\tau_{e,i} < 0$ and $\tau_{a,1} > \tau_{a,2}$), at equilibrium the planets are wide of the resonance by

$$\Delta_{\rm eq} \approx 1.1 \, \frac{m_1 + m_2}{M_*} \sqrt{k \frac{\tau_{a,\rm rel}}{\tau_e}} \tag{5.14}$$

where $\tau_{a,\rm rel}^{-1} \equiv \tau_{a,1}^{-1} - \tau_{a,2}^{-1}$ (Terquem & Papaloizou, 2019). We have also made use of the compact orbits approximation (see Section 5.2) and assumed $\tau_e \equiv \tau_{e,1} = \tau_{e,2}$.

Equation 5.14 presents an immediate challenge. For our fiducial system and a distance of $\Delta = 0.01$, the ratio of timescales must be $\tau_a/\tau_e \sim 10^5$. However, standard disk models predict $K \equiv \tau_a/\tau_e \sim (h/r)^{-2} \sim 100 - 400$, where h/r is the disk aspect ratio (Papaloizou & Larwood, 2000). Various suggestions have been made that K could be higher, including flared disks (Ramos et al., 2017), torque-free inner disk edges (Xiang-Gruess & Papaloizou, 2015), and alternative planet-disk interaction prescriptions (Charalambous et al., 2022). Some authors have also explicitly incorporated self-consistent disk models and torque calculations, with similar results to increasing K (Migaszewski, 2015; Cui et al., 2021).

However, higher values of K are only more efficient at damping eccentricity and finding the equilibrium. To test this, we simulated resonant capture for our fiducial system numerically. For this and all following integrations, we used the hybrid `mercurius` integrator implemented in the `rebound` package and the `reboundx` extension for disk-induced forces (Rein & Tamayo, 2015; Rein et al., 2019; Tamayo et al., 2020a). We initialized the planets on circular orbits at $\Delta_{\rm init} = 0.05$, and set $\tau_e = -10^5$ for both planets in units of the inner orbital period. Only the outer planet was made to migrate with $\tau_a = K \cdot \tau_e$, where K was varied from 10^2 to 10^5. When the integration time reached approximately $\tau_a/10$, the resonance was captured, the disk was removed adiabatically by increasing τ_a and τ_e. The results are shown in Figure 5.4. Although the final pairs span a large range in Δ, the mixed resonant angle librates with small amplitude and hence clusters near $\psi = \pi$. Similarly, the eccentricities follow the forced eccentricity curve and depend directly on Δ. Neither result is consistent with the TTV observations, which show a distinct break at $\Delta \approx 0.006$ and nonzero free eccentricities for many systems.

Turbulent Disks

Real protoplanetary disks are expected to have turbulent inner regions, where the magneto-rotational instability operates (Nelson & Papaloizou, 2004; Flock et al., 2017). The associated density fluctuations lead to stochastic gravitational forcing on the planet not captured by simple migration and eccentricity damping timescales (Nelson & Papaloizou, 2004). Stochastic forcing has been invoked to explain the smooth period ratio distribution (Rein, 2012), large libration amplitudes of

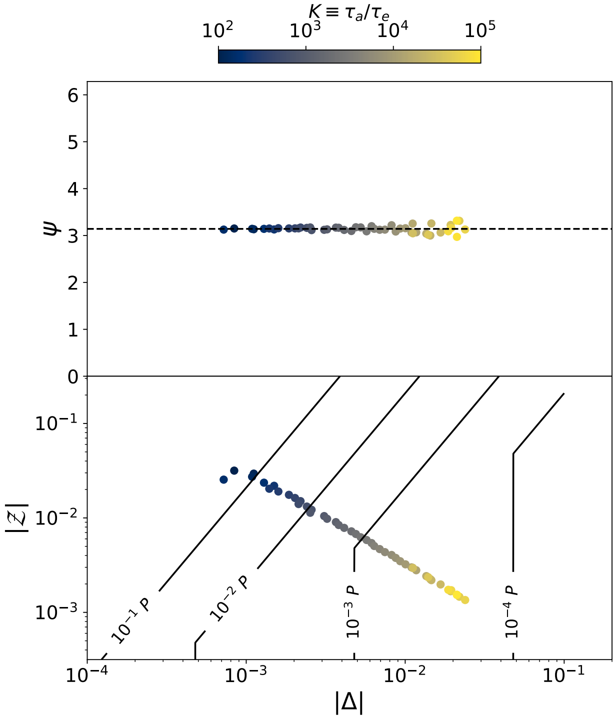

Figure 5.4: The results of the "laminar disk" population synthesis. The top panel shows $|\Delta|$ versus ψ, equivalent to Figure 5.1. The bottom panel shows $|\Delta|$ versus $|\mathcal{Z}|$, equivalent to Figure 5.2. Points are color coded by the ratio of semi-major axis to eccentricity damping timescales K. Contour lines and labels show the expected amplitude of transit timing variations (Eq. 5.10).

resonant planets (Nesvorný et al., 2022), and escape from resonance (Rein & Papaloizou, 2009; Batygin & Adams, 2017). Turbulent fluctuations have also been shown to be consistent with planet population synthesis models that include a phase of resonant capture (Izidoro et al., 2017).

The strength of turbulent forces in real disks is highly uncertain, so here we invoke a broad range of stochasticity. We implement stochastic forces with the `reboundx` package, in which the strength of the forces is parameterized by κ, the ratio of the stochastic force to the stellar gravitational force (Rein & Choksi, 2022). The forces themselves have an autocorrelation time equal to the planet orbital period. We ran 100 simulations of our fiducial system, with the same initial conditions as Section 5.4 but setting $K = 100$ and adding stochastic forces to both planets with a κ that varied uniformly in log space from 10^{-7} to 10^{-5}. Values of κ can also be related to the dimensionless disk viscosity α via diffusion coefficients (Rein, 2012; Batygin & Adams, 2017). Assuming a local disk surface density at 0.1 AU of 17000 g/cm^2 (Batygin & Adams, 2017), our range of κ approximately corresponds to a range in α of 10^{-5} to 10^{-1}. After 10^6 orbits of the inner planet, the disk forces were adiabatically removed and the system was integrated for another 5×10^5 inner orbits.

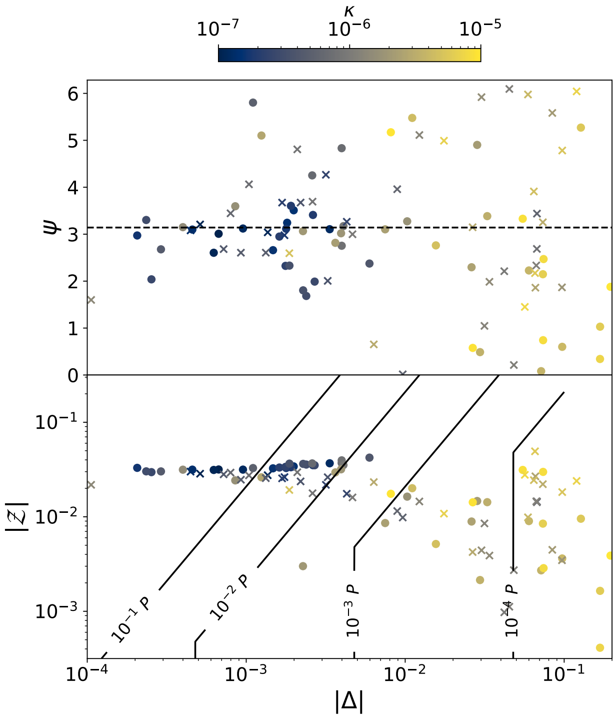

Figure 5.5: The same as Figure 5.4, but for the "turbulent disk" model. The points are color-coded by κ, the ratio of stochastic force to stellar gravitational force.

The results, plotted in Figure 5.5, are distinctly different than smooth disk migration (Figure 5.4) and qualitatively similar to the observed distribution. The final distance from resonance Δ is closely related to κ. Planets that experienced a small amount of turbulence remain in the resonance but have an excited libration amplitude. Inversely, planets for which $\kappa \gtrsim 10^{-6}$ escape the resonance entirely, and by virtue of their eccentricities being stochastically driven to ≈ 0.03, have a circulating resonant angle. We also ran another set of simulations fixing $K = 300$. The results were the same as Figure 5.5, except that there were fewer systems with $|\Delta| < 10^{-3}$ (as expected from Eq. 5.14). We experimented with longer integrations and found that systems with the largest values of κ typically escaped the 3:2 resonance and continued to migrate convergently, capturing into more compact first-order resonances. Because our model only considers proximity to the 3:2 resonance, these planets reached $\Delta < -0.1$ and thus were not considered in the final analysis. However, the systems that remained near the 3:2 resonance maintained the clustering trend seen in Figure 5.5 even in integrations that were three times longer.

Interestingly, this model of convergent migration with stochastic forcing naturally produces a population of planets with $\Delta \approx 0.01$ without invoking very large K or strong tidal dissipation. We note that the distribution of Δ in Figure 5.5 is controlled by the distribution of κ, which is log-uniform from 10^{-7} to 10^{-5} in our simulations. Hence the observed peak near $\Delta \approx 0.01$ could be a consequence of a corresponding peak in the distribution of κ, and thus in α. Within the formally resonant region, there appear to be too many systems with small but negative Δ, although these could conceivably be moved to positive Δ via a small degree of tidal damping without disrupting the distribution of ψ.

Tidal Damping

An alternative mechanism that has been invoked in the literature to explain the deviation from resonance is a dissipative force that acts after the protoplanetary disk is gone. In contrast to the case of disk migration, there is no equilibrium: as long as the force is present, the pair of planets will continue to diverge from exact resonance (Lithwick & Wu, 2012). A natural source of dissipation is tides raised on the planet by the star (Delisle & Laskar, 2014). There are major problems with this proposed solution however, including requiring anomalously small tidal quality factors (Lee et al., 2013), too high initial eccentricities (Silburt & Rein, 2015), and the lack of an expected signature of dependence on orbital separation (Choksi & Chiang, 2020). Tides strengthened by planetary obliquity (Millholland & Laughlin, 2019) may alleviate these issues somewhat, but not fully.

Regardless of the exact mechanism, tidal damping away from exact resonance involves considerable energy dissipation. To test the effect of this, we ran 200 integrations with 10 $M_\oplus$ planets near the 3:2 resonance. The initial eccentricities were 0.01 and ϖ was drawn randomly from a uniform distribution. For each simulation, we set the eccentricity dissipation timescale for each planet to $\{10^4, 10^5, 10^6, 10^7\}$ inner orbital periods and initial Δ uniformly from $[-0.05, 0.05]$. The simulations were run for 10^6 inner orbital periods, so that some systems experienced many damping timescales and others did not finish a single one.

The results of these integrations are shown in Figure 5.6. When tidal timescales are much longer than the integration duration, Δ does not change much and ψ remains in circulation. Inversely, when many tidal timescales elapse, the region of very small $|\Delta|$ is cleared out and ψ settles at an equilibrium value. Specifically, highly damped systems that end with $\Delta < 0$ go to the $\psi = 0$ equilibrium while those that end with $\Delta > 0$ go to the $\psi = \pi$ equilibrium. Neither trend agrees with the near-uniform distribution of ψ seen for the $|\Delta| > 0.006$ systems in Section 5.3.

Planetesimal Interactions

Other authors have suggested that a planetesimal disk, made of material that did not coalesce into planets, is responsible for damping and/or migration away from resonance (Chatterjee & Ford, 2015; Ghosh & Chatterjee, 2023). To reproduce the overpopulation of planet pairs wide of resonance, they place a population of planetesimals in orbit around a resonant pair of planets, and the resulting gravitational interactions increase Δ with a dependence on the local mass of material in the planetesimal disk. While the stochastic nature of planetesimal interactions can increase the

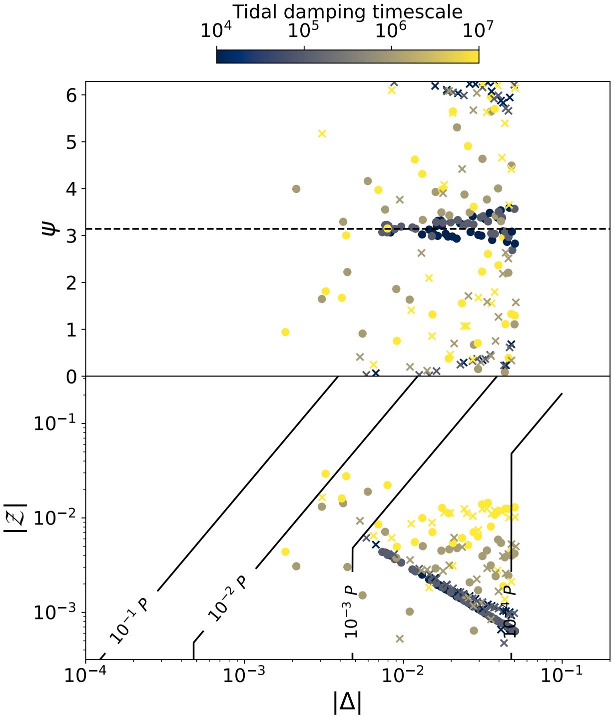

Figure 5.6: The same as Figure 5.4 but for the "Tidal damping" model. Points are color-coded by the timescale of eccentricity damping. In contrast to the other three models, the initial value of Δ was drawn uniformly from $[-0.05, 0.05]$.

phase space area somewhat, the broad effect is to act as an energy sink and damp the planet's eccentricity through dynamical friction.

To investigate this further, we ran a set of simulations that included a planetesimal disk, similar to the setup of Chatterjee & Ford, 2015; Ghosh & Chatterjee, 2023. To initialize the simulations, we applied gas-driven migration and eccentricity damping timescales as in Section 5.4 with $K = 100$ and removed the gas disk adiabatically. Once the gas was completely removed, we instantaneously added a planetesimal disk of 1000 equal-mass particles with total mass M_d. We varied M_d across 100 simulations log-uniformly from 10^{-1} to 10^{1} $M_\oplus$. The planetesimals were placed randomly at radii such that their surface density scales as $\Sigma(r) \propto r^{-2}$, the approximate steady state distribution for radially-drifting dust (Youdin & Chiang, 2004; Armitage, 2020). Following Ghosh & Chatterjee, 2023, we set the inner and outer edges of the disk to be the 1:3 and 3:1 resonances of the inner and outer planets, respectively. The eccentricities and inclinations (in radians) of the planetesimals were drawn uniformly from $[0, 0.01]$ to match the self-consistent simulations of Chatterjee & Ford, 2015. The remaining angular orbital elements were drawn uniformly from $[0, 2\pi]$. These integrations were run for 2×10^6 inner orbits. Planetesimals which passed within $1 R_\odot$ of the central star or $2 R_\oplus$ of either planet were merged with the nearby body while conserving linear momentum.

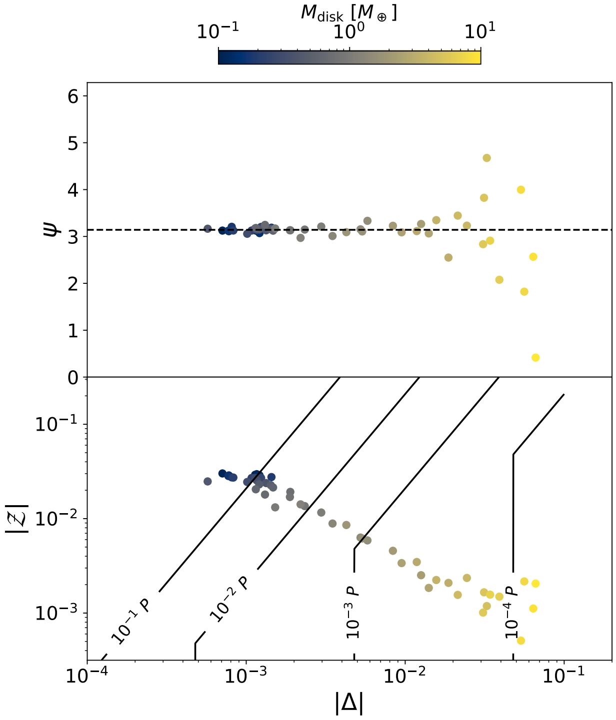

Figure 5.7: Same as Figure 5.4, but for the "Planetesimal disk" model. The points are color-coded by $M_{\rm disk}$, the total mass of planetesimals.

The results of this final suite of simulations are shown in Figure 5.7. Broadly, the systems remain near the resonant equilibrium like in the laminar disk model, except for a large increase in libration amplitude for $\Delta \gtrsim 0.05$. Though qualitatively similar to the break at $\Delta \approx 0.006$ in Figure 5.1, this break is nearly an order of magnitude more distant from exact resonance. Additionally, the final eccentricities are small and depend strongly on Δ, a trend not seen in the data (Figure 5.2). We note that Ghosh & Chatterjee, 2023 highlight the importance of a mixture model in which some systems begin not in resonance; these systems only experience limited eccentricity damping during the planetesimal migration phase and retain circulating resonant angles. Nevertheless, the dominant population within the peak around $\Delta \approx 0.01$ will be planet pairs that capture into resonance in the gas disk and will be highly damped after planetesimal interactions.

The planetesimal damping model also presents problems from the standpoint of model testing. While the planet formation process is certainly not 100% efficient, the true quantity and distribution of unaccreted material is complex, highly uncertain, and dependent on dust and planet migration as well as detailed disk structure (Hansen & Murray, 2012; Drążkowska et al., 2016; Raymond & Morbidelli, 2020). Furthermore, the model seems to require a degree of fine-tuning: planets that begin migrating through a disk 'run away' as long as material is present (see Ormel et al., 2012).

When integrated long enough, many initial conditions bring planets to $\Delta \sim 0.1$ rather than the observed peak at $\Delta \approx 0.01 - 0.02$ (Ghosh & Chatterjee, 2023).

5.5 Discussion

Dependence on multiplicity and resonant index

Many of the near-resonant systems within the *Kepler* sample are planet pairs, and for simplicity, we have assumed in our formation models that there are only two planets in the system and that they begin near the 3:2 resonance. The canonical transformation that replaces ϕ_1 and ϕ_2 with ψ in the first-order resonant term is not strictly valid for 3 or more planets. Additionally, the compact orbits approximation is acceptable for $k \geq 3$ but breaks down for $k = 2$, approximately $1/3$ of our sample.

To evaluate the dependence of our observational results on transit multiplicity, we split the sample into two subsamples of systems: one where only two transiting planets were detected and one where more than two were seen. Both subsamples show the libration-circulation break seen at $|\Delta| \approx 0.006$. However, there is a noticeable dearth of two-planet systems very close to commensurability. The eight systems with smallest $|\Delta|$ have three or more transiting planets, despite two-planet systems making up 41 of the 105 planet pairs. For resonant index, we performed a similar exercise by splitting the sample into two subsamples with $k = 2$ and $k \geq 3$. Of the 22 systems with $|\Delta| < 0.006$, only 2 are associated with the 2:1 resonance, despite that resonance accounting for 40 of the 105 planet pairs. A possible explanation for these trends is that low disk turbulence, relative to the migration rate, skips capture into the 2:1 resonance and delivers systems deep (i.e. small $|\Delta|$) into higher-index resonances. On the other hand, high turbulence may disrupt the most compact systems, leaving only circulating systems near the 2:1 resonance. We encourage more work on this topic.

Limitations of our work

Our analysis does not take into account the effects of sampling bias. Importantly, Hadden & Lithwick, 2017 and Jontof-Hutter et al., 2021 do not model systems with weak or undetectable TTVs. This choice preferentially discards lower-mass planets, pairs more distant from resonance, and pairs with small free eccentricity (Hadden & Lithwick, 2016). Our results should be robust to the first two effects because we do not directly model the distributions of planetary masses or Δ. The final effect suggests that some nearly circular systems might be missing from Figure 5.2 at higher Δ. However, Eq. 5.10 indicates that the dependence on eccentricity is only important for $|\mathcal{Z}| \gtrsim |\Delta|$. Thus, highly damped systems at $\Delta \sim 0.01$ would be observable if they existed, but they are not seen in Figure 5.2.

An additional sytematic bias in the models of Hadden & Lithwick, 2017 and Jontof-Hutter et al., 2021 is that they only consider the TTV contributions from known, transiting planets. Unseen planets may induce a TTV signal that is interpreted as coming from one of the transiting planets, biasing the measured ψ and $|\mathcal{Z}|$.

Eccentricity Excitation or Damping?
In general, it is not obvious what sets the eccentricities of planets in multiplanet systems. Transit timing and transit duration measurements have independently agreed that typical eccentricities in multi-planet systems are small but nonzero (Hadden & Lithwick, 2017; Van Eylen et al., 2019). There is no evidence of correlation between eccentricity and any system properties except multiplicity (Van Eylen et al., 2019; He et al., 2020). Eccentricities must be bounded below by self-excitation (even for initially circular orbits) and above by orbit-crossing and stability limits. Remarkably, the observed census of planetary systems falls in between these two regimes: planets are neither dynamically cold, nor do they reside right at the stability boundary (Yee et al., 2021). Therefore, planet formation scenarios that rely on strong damping must eventually include a source of eccentricity excitation; alternatively, scenarios that invoke dynamical sculpting as the dominant process require damping. Ultimately, the full story of planet formation must incorporate a competition between mechanisms of eccentricity damping and excitation.

5.6 Conclusion

In this work, we have reanalyzed the near-resonant planetary systems characterized with transit timing variations from *Kepler*. We show that despite fundamental limitations in TTV interpretation, the resonant behavior of these systems can be probed in detail. Planet pairs very close to exact resonance ($|\Delta| < 0.006$) have a librating mixed resonant angle, but those in the peak $\sim 1\%$ wide of resonance are predominantly circulating. This result is difficult to reconcile with several hypotheses which argue that dissipative processes place pairs of planets wide of resonance, keeping them in a stable quasi-equilibrium state. Stochastic forces during migration, meant to simulate density variations in a turbulent gaseous disk, offer a promising explanation for the qualitative features of the sample.

Future work should use a more thorough modeling effort that consider a mixture of resonant and non-resonant systems. Recent theories of planet formation have argued that near-universal dynamical instabilities successfully reproduce the observed mostly smooth period ratio distribution (Izidoro et al., 2017). In such a model, some planet pairs are ‘near-resonant’ only coincidentally (reaching that state after the dissipation of the protoplanetary disk) and not as the consequence of resonant capture or damping. The actual fraction of systems that never experienced a post-gas instability in the overall sample is unclear: Izidoro et al., 2021 suggest that no more than 5%

remain stable and resonant, but it remains to be seen whether those results are consistent with the overabundance of three-body libration seen in the *Kepler* sample (Goldberg & Batygin, 2021; Cerioni et al., 2022). While basic modeling of the peaks in the period ratio distribution has had some success (e.g., Choksi & Chiang, 2020; Ghosh & Chatterjee, 2023), the results of this work illuminate a novel and stringent constraint that must be accounted for in a complete model of planet formation.

Chapter 6

TOI-1136 IS A YOUNG, COPLANAR, ALIGNED PLANETARY SYSTEM IN A PRISTINE RESONANT CHAIN

Dai, F., Masuda, K., Beard, C., et al. (Feb. 2023). "TOI-1136 Is a Young, Coplanar, Aligned Planetary System in a Pristine Resonant Chain." In: *The Astronomical Journal* 165, p. 33. ISSN: 0004-6256. DOI: `10.3847/1538-3881/aca327`.

6.1 Introduction

During the protoplanetary disk lifetime, gravitational interactions between the gaseous disk and embedded planets imparts a torque onto the planets. The resulting orbital migration can lock pairs of planets into mean-motion resonance (MMR) if the migration is convergent and sufficiently slow that the resonant encounter is adiabatic (Cresswell & Nelson, 2006; Cresswell & Nelson, 2008; Batygin, 2015). This process can be extended to capture multiple planets in a chain of resonance (see Kley & Nelson, 2012, and references therein). Different studies using adiabatic perturbation theory (Henrard, 1982; Batygin, 2015), modified N-body integration (e.g., Lee & Peale, 2002; Terquem & Papaloizou, 2007) and hydrodynamic simulations (e.g., Kley et al., 2005; Ogihara & Ida, 2009; Cresswell & Nelson, 2008; Ataiee & Kley, 2020) all came to the same conclusion that convergent disk migration consistently generates compact, first-order resonant chains of planets. The detection of $\sim$ 10 resonant chains to date is compelling evidence that this migration-capture paradigm is a realistic model, at least in those systems. In fact, this process of resonant capture is considered to be so effective and robust that it is difficult to understand why only a few percent of *Kepler* multi-planet systems are near first-order MMR (Fabrycky et al., 2014).

Planetesimal scattering (Chatterjee & Ford, 2015), tidal dissipation (Lithwick & Wu, 2012; Batygin & Morbidelli, 2013), secular chaos (Petrovich et al., 2019), and orbital instability (Pu & Wu, 2015; Izidoro et al., 2021; Goldberg & Batygin, 2022) are some of the possible mechanisms for breaking migration-induced resonances as planetary systems mature. Some of these processes may take as long as billions of years to manifest. One might expect, therefore, that when the Kepler multi-planet systems were younger, they were also closer to resonance or truly resonant. In this chapter, we present a young system that is deep in resonance. TOI-1136 has a resonant chain of at least 6 transiting planets, all of which display TTVs. The planets' orbital period ratios deviate from perfect integer period ratio by 10^{-4}. With an age of only 700 Myr, TOI-1136 may still record a pristine orbital architecture produced by convergent disk migration, before subsequent dynamical evolution has had the chance to disrupt the resonance.

The chapter, adapted from excerpts of Dai et al. (2023) with some additional analysis, is organized as follows. Section 6.2 briefly outlines analysis of the photometric and spectroscopic data. Section 6.3 investigates the resonant configuration of TOI-1136, while Section 6.4 concerns disk environments that could form the system. Sections 6.5 and 6.6 considers the implications for the formation and evolution of TOI-1136 in relation to other multi-planet systems, including TRAPPIST-1.

6.2 Observations

TOI-1136 (TIC 142276270) is a G5 star that was observed by the TESS mission (Ricker et al., 2014) in Sectors 14, 15, 21, 22, 41, and 48 from Jul 18 2019 to Feb 25 2022. Analysis of the data by the TESS team and ExoFOP[1] identified six transiting planets on orbits of 4.2, 6.3, 12.5, 18.8, 26.3, and 39.5 days. We also obtained high-resolution spectra with HIRES on the Keck I telescope to robustly measure stellar parameters and Adaptive Optics images with the Gemini Near-Infrared Imager to rule out nearby stellar companions. Finally, a Rossiter-McLaughlin measurement of planet d confirmed that the orbital plane was well-aligned with the stellar spin axis. Details of the analysis are provided in Dai et al., 2023.

Importantly, TOI-1136 is an unusually young planet host. Several lines of evidence, including gyrochronology, Ca II H&K activity, and lithium abundance suggest an age of 700 ± 100 Myr. TOI-1136 thus presents an opportunity to study a planetary system that may be less evolved than typical *Kepler* and TESS systems.

The six observed planets of TOI-1136 lie close to mean-motion resonances. The period ratios of adjacent planets are very nearly 3:2, 2:1, 3:2, 7:5, and 3:2, suggestive of a resonant chain architecture. The proximity to resonance, described by the dimensionless parameter Δ (see Eq. 2.3) is extremely small: $\Delta \sim 10^{-4}$ for all planet pairs. We conducted a thorough analysis of the resonant structure of TOI-1136, described below.

Each planet displayed large TTVs, which were measured by fitting a transit model (Kreidberg, 2015) to the light curve. As a result of the extreme proximity to mean-motion resonance, the well-known analytic formulae for near-resonant TTVs (Lithwick et al., 2012) do not apply. Although analytic expressions have also been derived for resonant TTVs (Nesvorný & Vokrouhlický, 2016), they may not completely capture the complex behavior of the resonant chain. Instead, we modeled the observed TTVs with full N-body integrations of the orbits and sampled the posterior distribution of orbital parameters using Hamiltonian Monte Carlo (Betancourt, 2017).

---

[1] `https://exofop.ipac.caltech.edu`

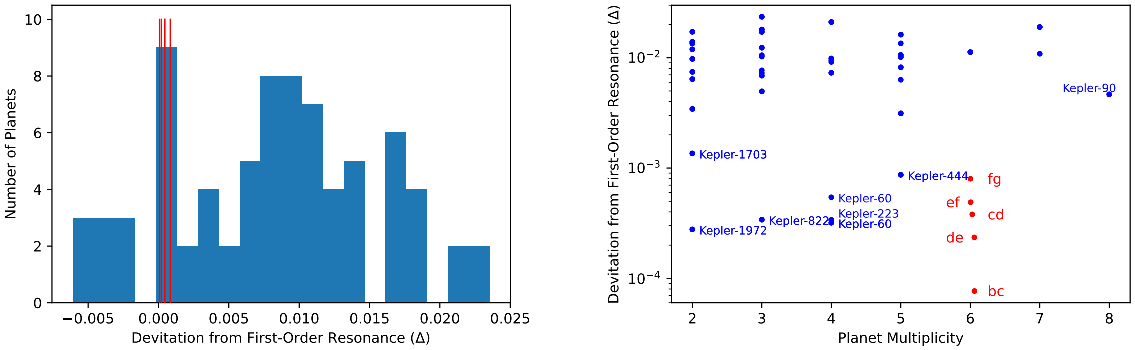

Figure 6.1: The deviation from first order MMR ($\Delta \equiv \frac{P_{out}/P_{in}}{p/q} - 1$) in TOI-1136 (red symbols) and the vetted *Kepler* multi-planet sample (blue symbols, Petigura et al., 2017). Most near-resonant *Kepler* multi-planets have a Δ of $\sim 1\%$ from perfect integer ratio. TOI-1136 joins a small number of systems deep in resonance with a $\Delta \lesssim 10^{-3}$. Many other planets with similarly low Δ also have a resonant chain of planets.

6.3 Mean-Motion Resonance in TOI-1136

The hallmark of true MMR is the libration of the relevant resonant angles. For a planetary system near resonance, one can decompose the Hamiltonian into the Keplerian, resonant, and secular terms (Murray & Dermott, 1999). The generalized coordinate for the resonant interaction is the resonant angle. For two-planet systems, the resonant angle ϕ takes the form:

$$\phi_{12} = q\lambda_1 - p\lambda_2 + (p-q)\varpi_{1,2} \tag{6.1}$$

where λ is the mean longitude, ϖ is the longitude of the pericenter, and p and q are positive co-prime integers. Following D'Alembert's rule, $\varpi_{1,2}$ can be an integer combination of ϖ_1 and ϖ_2 such that the sum of the coefficients is $p-q$. The strength of the MMR is proportional to $e^{|p-q|}$. For a system in true 2-body MMR, ϕ_{12} typically librates around a libration center with limited amplitude, as opposed to circulating between 0 to 2π.

It is thus tempting to compute the time evolution of the relevant resonant angles for each planet pair in TOI-1136. However, our initial attempts to do so were not promising. Many dynamically-stable TTV solutions showed circulation or highly irregular behavior of the resonant angles. This represented a major discrepancy because TOI-1136 clearly has a resonant chain architecture and all planet pairs are very close to mean-motion commensurabilities. Figure 5.1 demonstrates that even systems an order of magnitude further from exact resonances are universally librating.

The origin of the issue ended up being exactly the degeneracy described in Section 5.3. Sparse TTV coverage allows a broad range of eccentricities in the posterior distribution, which only marginally

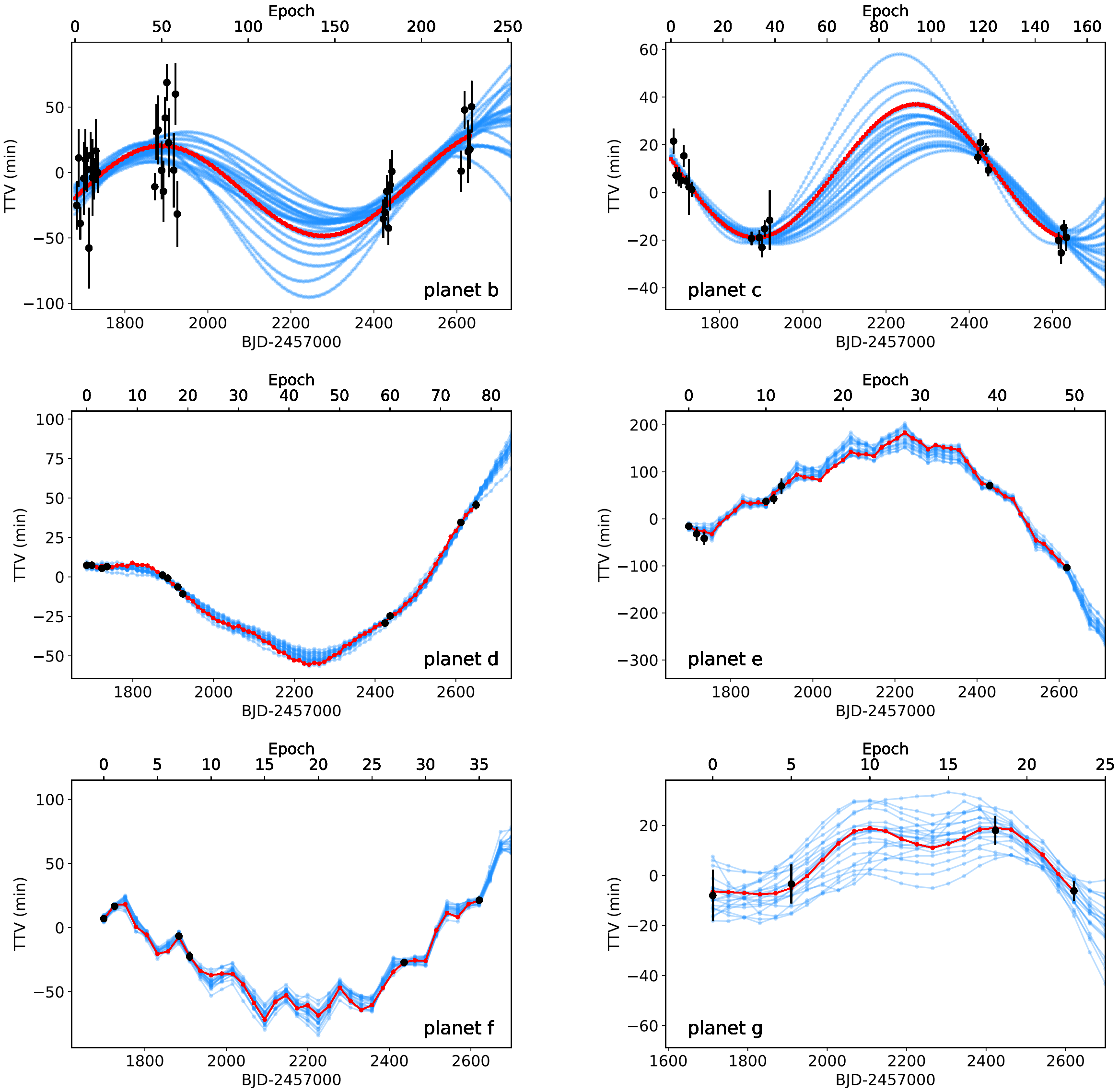

Figure 6.2: The observed transit timing variations of the planets in TOI-1136, the best fit TTV model (red curve), and 20 dynamically stable posterior samples (blue curves). All data came from TESS observations except for the last transit of planet d, which came from our RM measurement. TTVs from neighboring planets are anti-correlated. The super-periods are estimated to be $\gtrsim$ 10000 days, which is much longer than the current observational baseline. Instead, the TTVs are driven by the libration of the resonant angles (Nesvorný & Vokrouhlický, 2016).

affect the dynamics but dramatically change the resonant angles through ϖ (see also Petit et al., 2020b). Chapter 5 suggests the solution is to consider the mixed resonant angles that are obtained during a dimension-reducing canonical transformation (Sessin & Ferraz-Mello, 1984; Batygin, 2015). Specifically, we calculate

$$\psi = p\lambda_2 - (p-q)\lambda_1 - q\hat{\varpi} \tag{6.2}$$

where $\hat{\varpi}$ is a generalized longitude of pericenter:

$$\hat{\varpi} = \mathrm{Arg}(fe_1e^{\iota\varpi_1} + ge_2e^{\iota\varpi_2}) \tag{6.3}$$

and f and g are order-unity constants that depend on the index and order of the resonance. While Sessin & Ferraz-Mello, 1984 and Batygin, 2015 only considered this construction for first-order resonances, Hadden, 2019 demonstrated that it remains appropriate for higher-order resonances given suitable choices of f and g.[2]

Examination of the mixed resonant angles immediately resolves the discrepancy. The two-body mixed angles are unambiguously in libration (Figure 6.4) with the possible exception of the 7:5 resonance between e and f, which shows circulation in 9% of the stable TTV solution. TOI-1136 is therefore a *bona fide* resonant chain, joining the small but growing ranks of systems in this pristine configuration. Notably, TOI-1136 is the sole example of a resonant chain with a librating higher-order resonance.[3]

When more than two planets are involved in MMR, one can also obtain resonant angles independent of ϖ. By simply subtract the 2-body resonant angles (Eq. 6.1) of neighboring pairs, ϖ cancels and the resulting angle is well-constrained by transit data. For a concrete example, consider TOI-1136 b, c, and d:

$$\phi_{\mathrm{bc}} = 2\lambda_b - 3\lambda_c + \varpi_c \tag{6.4}$$

$$\phi_{\mathrm{cd}} = \lambda_c - 2\lambda_d + \varpi_c \tag{6.5}$$

$$\phi_{\mathrm{bcd}} = \phi_{\mathrm{bc}} - \phi_{\mathrm{cd}} = 2\lambda_b - 4\lambda_c + 2\lambda_d. \tag{6.6}$$

A perceptive reader might point out that the coefficients are no longer co-prime and that we should divide by 2. We chose not to do so following the suggestion of Siegel & Fabrycky (2021). The benefit of keeping the original coefficients is that the libration centers of the 3-body angles are now near 180° in this formulation.

In Table 6.1, we list the various resonant angles for TOI-1136. Before describing the results, we highlight an effect that can shift the libration centers. For a chain of planets in resonance, their

---

[2] In the case of the 7:5 resonance between TOI-1136 e and f, $f = -2.81$ and $g = 3.37$.

[3] TRAPPIST-1 b/c and c/d are near the 8:5 and 5:3 resonances, respectively, but it is unclear whether either is actually active (see Section 6.5).

mutual interactions change the topology of the Hamiltonian, especially when there is a non-adjacent first-order MMR. New libration centers can emerge that are shifted away from 180° (e.g., Delisle, 2017). A system can be captured in one of the possible libration centers depending on the order of which planets are captured into resonance (Delisle, 2017). For example, Kepler-223 is in a 3:4:6:8 resonant chain (Mills et al., 2016). The bd pair (6:3≡2:1) and the ce pair (8:4≡2:1) are both examples of non-adjacent first-order MMR. The 3-body libration centers were hence shifted to 168° and 130° in that system (Siegel & Fabrycky, 2021). Delisle (2017) suggested that the observed configuration is perhaps most consistent with Kepler-223 c and d having been captured into MMR before e and b. Fortunately (or sadly), there is no non-adjacent first-order MMR in TOI-1136, so one need not worry about (or cannot take advantage of) this effect.

We integrated the stable TTV solutions forward in time for 50000 days with `rebound` and recorded the various resonant angles of TOI-1136 listed in Table 6.1. We identified systems in which the resonant angles are clearly circulating (ϕ varied by much more than 2π). Then, to identify the librating solutions, we calculated the mean of the resonant angles during this 50000-day period. We also computed the libration amplitude using the formula in Siegel & Fabrycky (2021) and Millholland et al. (2018),

$$A = \sqrt{\frac{2}{N}\sum\left(\phi - \langle\phi\rangle\right)^2} \tag{6.7}$$

where $\langle\phi\rangle$ is mean of the resonant angle and N is the number of resonant angles sampled. If the libration of the resonant angle is sinusoidal in shape and sampled regularly in time, then A corresponds to the amplitude of that sinusoid. We adopted a generous definition of libration: a system is in libration if the amplitude is less than 90°. We can see in Table 6.1 that most libration amplitudes are much smaller than this threshold.

Figure 6.4 summarizes the relationships between the various resonant angles and the fraction of librating solutions for each angle. We found that the various resonant angles involving only first-order resonance have a high probability of libration in our stable TTV solutions. The fraction is close to unity for the 2-body angles, and steadily drops as we move up the resonance ladder from 2-body resonance to multi-body resonance. The inner triple bcd (ϕ_{bcd}) has a 99% probability of being a resonant chain. Moreover, the libration centers are almost always near 0 or 180° (Table 6.1) as found by Siegel & Fabrycky (2021). The only exceptions are the resonant angles involving planets c and d (2:1 MMR). Beauge (1994) showed that the topology of the phase space of the 2-body 2:1, 3:1, n:1 MMR permits two libration centers that are shifted from 180°. The shifts increase with orbital eccentricity. A planetary system may adopt one of these libration centers, or chaotically shift between them if the libration amplitude is large enough. This was confirmed in our convergent disk migration simulations (Section 6.4 and the first panel of Figure 6.3): resonant angles involving TOI-1136 c and d are shifted from 180° by asymmetric libration.

Resonant Angle	Fraction in Libration	Libration Center	Libration Amplitude
2-body Resonant Angles			
$\phi_{\mathrm{bc}} = 2\lambda_b - 3\lambda_c + \hat{\varpi}_{bc}$	100%	179.1±1.5 °	9.6±1.5 °
$\phi_{\mathrm{cd}} = \lambda_c - 2\lambda_d + \hat{\varpi}_{cd}$	100%	176.7±6.8 °	14.6±6.6 °
$\phi_{\mathrm{de}} = 2\lambda_d - 3\lambda_e + \hat{\varpi}_{de}$	100%	180.5±1.5 °	17.3±7.7 °
$\phi_{\mathrm{ef}} = 5\lambda_e - 7\lambda_f + 2\hat{\varpi}_{ef}$	91%	182.1±7.4°	36±13°
$\phi_{\mathrm{fg}} = 2\lambda_f - 3\lambda_g + \hat{\varpi}_{fg}$	100%	180.3±1.0 °	19±15 °
3-body Resonant Angles			
$\phi_{\mathrm{bcd}} = 2\lambda_b - 4\lambda_c + 2\lambda_d$	99%	196±15 °	19±9 °
$\phi_{\mathrm{cde}} = 1\lambda_c - 4\lambda_d + 3\lambda_e$	93%	163±30 °	45±22 °
$\phi_{\mathrm{def}} = 4\lambda_d - 11\lambda_e + 7\lambda_f$	51%	173±37°	64±13°
$\phi_{\mathrm{efg}} = 5\lambda_e - 11\lambda_f + 6\lambda_g$	58%	143±51 °	69±19 °

Table 6.1: Resonant Angles in Stable TTV Posterior.

In contrast to the first-order MMRs, the resonant angles that involve the only second-order MMR (planet e and f, 7:5) have somewhat reduced probabilities of libration. Second-order MMR, by nature, is much weaker and much more localized in phase space than first-order MMR (Murray & Dermott, 1999). In about 9% of our TTV solution, the second-order resonant angle ϕ_{ef} alternates between circulation and libration (Figure 6.3 lower panel). Alternation between libration and circulation is a hallmark of chaos and has been previously identified in Kepler-36 (Carter et al., 2012) and several *Kepler* systems (Hadden & Lithwick, 2017). However, we strongly suspect that e and f are indeed in a 7:5 second-order MMR. In our stable TTV solutions, planets e and f do have a ~91% chance of being in 2-body libration. The observed orbital period ratio differs from 7:5 by only $4.5 \pm 1.6 \times 10^{-4}$; it seems very unlikely to be coincidental. Our current TTV solutions of TOI-1136 are often chaotic on short timescales, with some Lyapunov times of the order 10^5 days. Again, we suspect that with the current TTV data, we have not located the true island of stability in phase space.

6.4 The Disk that Formed TOI-1136

The unique architecture of TOI-1136 allows us to place stringent constraints on TOI-1136's formation environment. We first discuss qualitative predictions of the initial conditions and disk parameters, and then use numerical simulations to confirm them and develop quantitative constraints.

Planet pairs in TOI-1136 are unusually close to exact resonance, even among resonant chains (Figure 6.1). Proximity to resonance following resonant capture is directly related to the ratio of eccentricity damping to migration in the protoplanetary disk (Terquem & Papaloizou, 2019). The approximate formula Eq. 5.14 suggests that, for $\Delta \sim 10^{-4}$, the ratio of eccentricity damping to migration, defined as $K \equiv \tau_a/\tau_e$, is $K \sim 100$. As in Chapter 5, we can directly relate K to disk

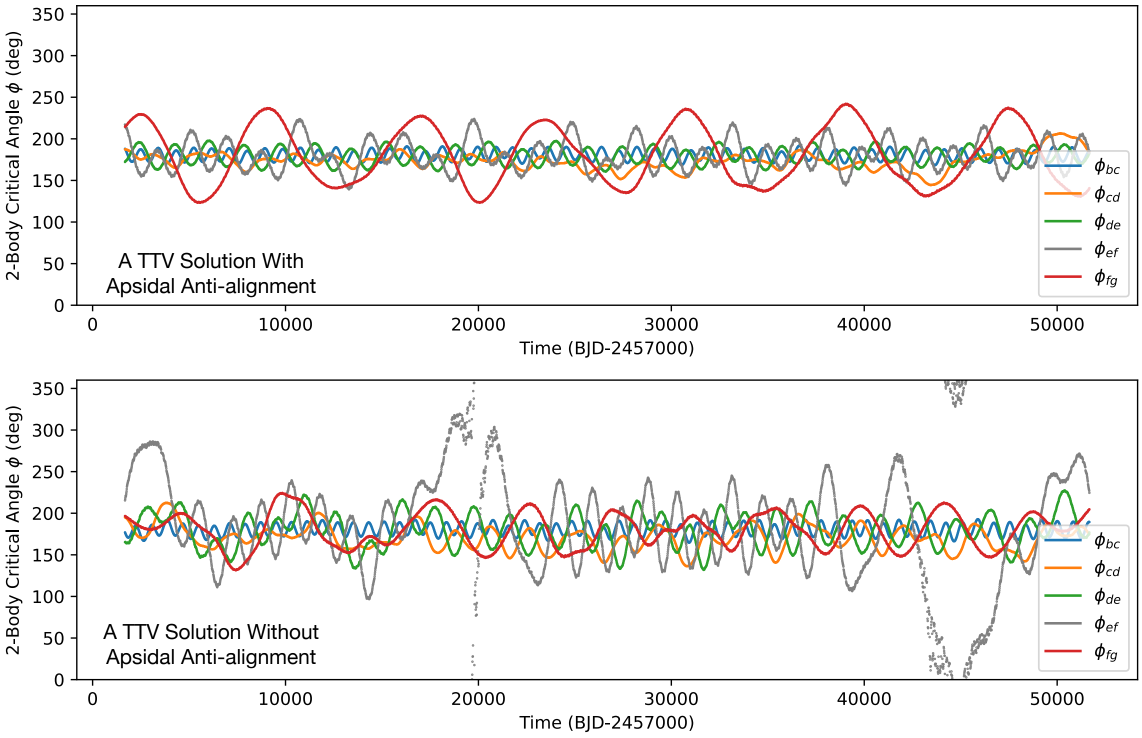

Figure 6.3: Evolution of the two-body resonant angles in two of our TTV solutions. A classical prediction of convergent disk migration (e.g., Batygin, 2015) is that neighboring planets should have anti-aligned pericenters (except the Asymmetric Libration of cd in 2:1 MMR, see text). A significant fraction of our TTV solutions conform to this prediction. The evolution of 2-body resonant angles of these solutions librate near 180° over the next 50000 days (top panel). However, other TTV solutions are far from apsidal anti-alignment. Planet e and f (7:5 second-order resonance) in these solutions often show chaotic behavior where their 2-body resonant angle ϕ_{ef} can oscillate between a state of libration and circulation.

structure; specifically, $K \sim (h/r)^{-2}$ where h/r is the disk scale height. The implied $h/r \sim 0.1$ is reasonably consistent with models of the inner disk (Flock et al., 2017; Zhu et al., 2023). The small values of Δ also severely restrict the amount of tidal dissipation experienced by the planets, which acts to increase Δ. Although TOI-1136 is a young system with little time to tidally evolve, this places it in stark contrast to Kepler-221, which has achieved an extreme degree of tidal evolution in a similar timespan (Chapter 4).

The second-order 7:5 resonance between planets e and f is likewise highly informative. For one, e and f most likely started with an initial period ratio between 1.4 and 1.5 in order to avoid capture into the nearby, much stronger 3:2 first-order MMR. Xu & Lai (2017) identified several other conditions for the successful capture and stability of a second-order MMR. In contrast to first-order resonances, which exist at any eccentricity, higher-order resonances have zero width for circular

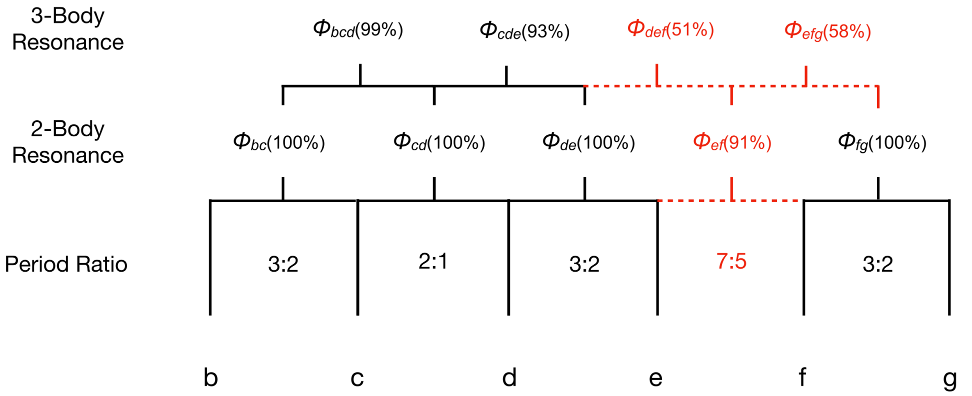

Figure 6.4: The ladder of the resonant angles involving increasingly more planets. We recorded the resonant angles (Table 6.1) in the stable TTV solutions for 50000 days. The fraction of the TTV posterior sample in which the specific resonant angle librates is shown in the bracket. The resonant angles that involve the second-order resonance of planet e and f (7:5 MMR) have a reduced probability of libration.

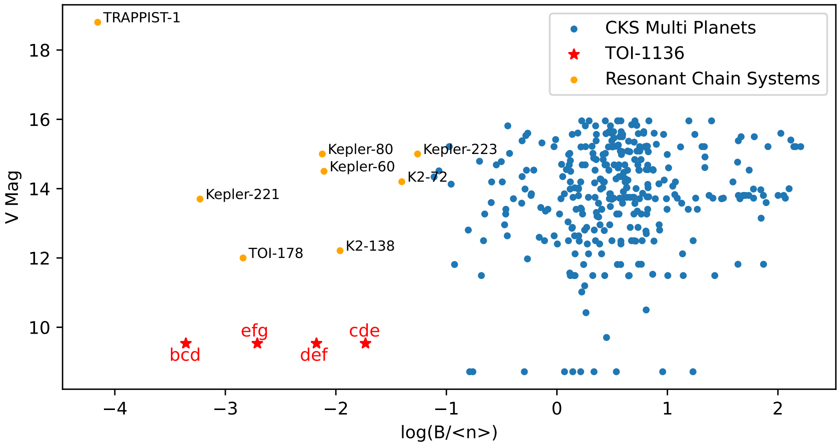

Figure 6.5: B is another metric for identifying resonant chain systems: $B = |pn_1 - (p+q)n_2 + qn_3|$, where n_i is the mean motion, p and q are co-prime integers (Goldberg & Batygin, 2021). For non-resonant systems, B is uniformly distributed but, but in resonant systems where a generalized Laplce angle is librating, the time derivative of the angle B should be very small. Plotted here is B normalized by the average mean motion $\langle n \rangle$ of the *Kepler* multi-planet systems (blue), TOI-1136 (red), and other known resonant chains (orange). B values in TOI-1136 are similarly low as the other resonant-chain systems. TOI-1136 is by far the most observable resonant-chain system with a V-band magnitude of 9.5.

orbits.[4] Eccentricity damping in the disk must thus be weak enough to allow e and f to maintain nonzero eccentricity, especially after resonant capture. This condition is equivalent to requiring a small K, reassuringly consistent with the requirement from the small Δ. Second-order resonances are also weaker than first-order ones in general and hence the resonant region is narrower. To ensure the resonant encounter is adiabatic, migration must be slow enough to cross the resonance width on a longer timescale than the resonant libration (Batygin, 2015). The disk must therefore have a relatively low surface density, which sets the overall migration rate. Finally, preservation of a weak resonance implies a low turbulence in the disk, because gravitational kicks from turbulent eddies can break resonance (Adams et al., 2008; Paardekooper et al., 2013; Batygin & Adams, 2017).

We performed a suite of simulations of disk migration to confirm these predictions and place quantitative constraints on the conditions in which the observed MMRs of TOI-1136 could form. We experimented with three prescriptions of initial conditions and planet-disk interactions. In all cases an inner edge of the disk was placed at 0.05 AU to trap the innermost planet at that location (Masset et al., 2006) and planet masses were drawn from the TTV posterior distribution. In the first case, we initialized the planets 2–5% outside of their current locations and applied Type-I migration forces to all of the planets. Migration and eccentricity damping rates were varied by selecting disk surface densities and aspect ratios. In the second case, only the outermost planet is allowed to migrate, the same scenario employed by Tamayo et al. (2017) to form TRAPPIST-1, and all of the planets experience eccentricity damping. Tunable parameters in this case are the migration rate of planet g and the ratio of the eccentricity damping rate to the migration rate. The third prescription applies the same forces as the first, but initializes the planets beyond 1 AU to simulate a long-range migration scenario.

The results are summarized in Figure 6.6. We consider a simulation successful if all six planets get locked into their observed MMR with no more than 0.1% deviation; and the respective 2-body and 3-body resonant angles are all librating. The most common failure mode is that the planets e and f skip the weaker second-order 7:5 MMR and gets locked in the nearby stronger first-order MMR (4:3 and 3:2, see third row of Figure 6.6). Our simulations disfavored the third prescription: long-scale (from 1AU to 0.05AU) Type-I migration. None of 200 simulations with this prescription managed to form a system like TOI-1136. If the planets experienced long-scale migration, their migration rate must be high enough so that they can arrive at the observed 0.05AU separation before the disk dissipates, but such fast migration can easily skip the 7:5 resonance (Xu & Lai, 2017). Even in

---

[4] This can be understood geometrically. The order of a resonance is also the number of planet-planet conjunctions, where the mutual gravitational force is strongest, per resonant cycle. The net force summed over all conjunctions is always strong when there is only one conjunction. At order two or more, the conjunctions are evenly spaced and the net force cancels out for circular and coplanar orbits. Only nonzero eccentricity or inclination can break the symmetry and generate a true resonant interaction.

some realizations where planet e and f initially get captured into 7:5 MMR, 1AU to 0.05AU is such a long journey that perturbations form the other planets eventually disrupted the weak 7:5 MMR.

Our two short-scale (0.1AU) migration prescriptions both abundantly produce TOI-1136 analogs (Figure 6.6). However the second prescription, migrating only the outermost planet, seems less likely. To form analogs of TOI-1136, the second prescription often requires slower migration with timescales of several Myr that often exceeds typical disk lifetime (second row of Figure 6.6). Our simulations only rarely deposit planet b and c to the observed 10^{-4} level from perfect resonance (bottom row of Figure 6.6).

Our first prescription, short-scale Type-I migration on all planets with a disk edge, seems to be the more likely scenario. As shown in Figure 6.6, the first prescription can produce systems like TOI-1136 (including 7:5 MMR) even with rapid Type-I migration of $\tau_a = 10^4 - 10^6$yr. This is thanks to the inner edge of the protoplanetary disk which slows down and even reverses the effective migration (Masset et al., 2006). The disk edge stalls the inner planets at the edge and thereby allows planets further out to catch up and join the resonant chain (Izidoro et al., 2017). Within the limitations of Type-I migration prescription of Cresswell & Nelson (2006), Paardekooper et al. (2023), and Pichierri et al. (2018), our successful disk migration simulations correspond to a protoplanetary disk no denser than $\sim$ 1000 g cm^{-2} at 1AU (Figure 6.7). This is comparable but lower than the surface density of the MMSN ($\approx$ 1700 g cm^{-2}; Hayashi, 1981). As expected, a smaller $K \equiv \tau_a/\tau_e$, or slower damping of orbital eccentricity, is needed to achieve the observed large e and small deviation from MMR (Figure 6.6 and Figure 6.1). To reproduce the observed $\Delta \sim 10^{-4}$ (gray area in Figure 6.6), K has to be smaller than about 100.

In comparison, Hühn et al. (2021) used a very similar prescription of disk migration with an inner disk edge to constrain the formation of Kepler-223, which only contains first-order MMR (Mills et al., 2016). Hühn et al. (2021) noted that Kepler-223 could form from convergent disk migration with a wider range of disk properties: the disk surface density can be a few times denser than the MMSN but still lock all planets of Kepler-223 into a resonant chain.

6.5 Comparison with TRAPPIST-1

Given several similarities and differences between TOI-1136 and the resonant chain TRAPPIST-1, it is worth discussing how these systems compare and how we can relate the system architectures to post-disk evolution. TRAPPIST-1 is a very low-mass star ($0.09M_\odot$) with seven detected planets. The planets have masses ranging from 0.5 to $1.5M_\oplus$, but the small stellar mass results in planet-to-star mass ratios similar to TOI-1136 (Agol et al., 2021). Importantly, TRAPPIST-1 also has hints of higher-order resonance: the pairwise period ratios are nearly 8:5, 5:3, 3:2, 3:2, 4:3, and 3:2

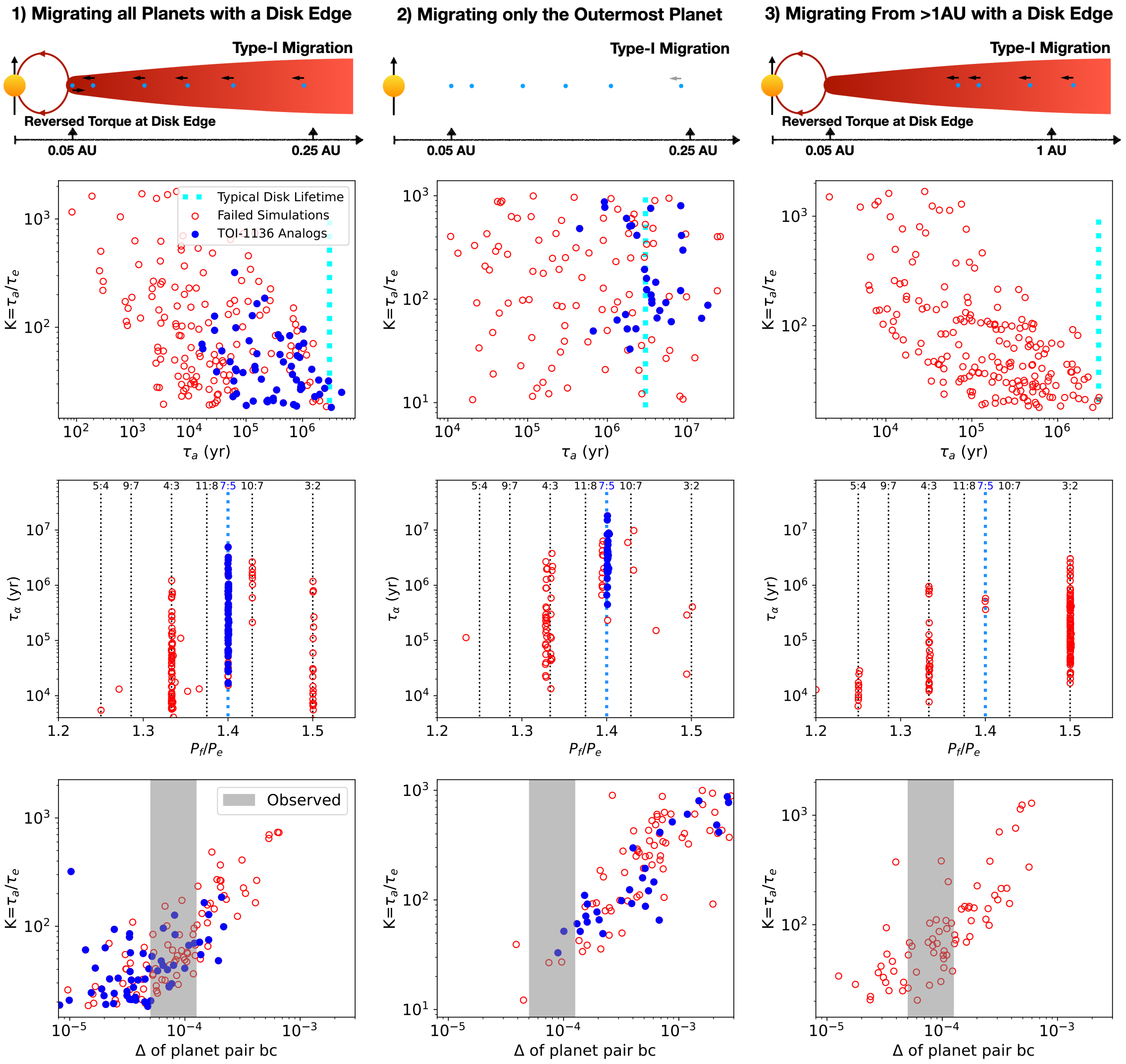

Figure 6.6: Summary of our disk migration simulations (Section 6.4). We experimented with three prescriptions of disk migration: 1) Type-I migration to all planets simultaneously with a disk edge (left column). 2) Type-I migration to only the outermost planet. 3) Similar to Case 1 except that the planets migrated from beyond 1AU as opposed to 0.1 AU (right column). The top row shows the schematics for each mode of migration. The second row shows the results of the simulation in terms of migration timescales in τ_a and $K \equiv \tau_a/\tau_e$ compared with the typical disk lifetime (~3Myr for sun-like stars, Andrews, 2020). The blue filled symbols are simulations that formed analogs of TOI-1136 where planets are in their observed resonances. The red hollow symbols are systems that have failed (usually e and f skipped 7:5 and became locked in a nearby first-order MMR). The third row shows the final orbital period ratio between planet e and f. The fourth row shows the depth of MMR produced in Δ at the end of the simulations. The gray area indicates the observed Δ between planet b and c. In general, the first prescription: short-scale (from 0.1AU) disk migration with a disk edge is the most robust at producing systems of TOI-1136. It can deposit systems deeper in MMR with $\Delta \lesssim 10^{-4}$ as was observed in TOI-1136. The migration process could be completed quickly within typical disk lifetime.

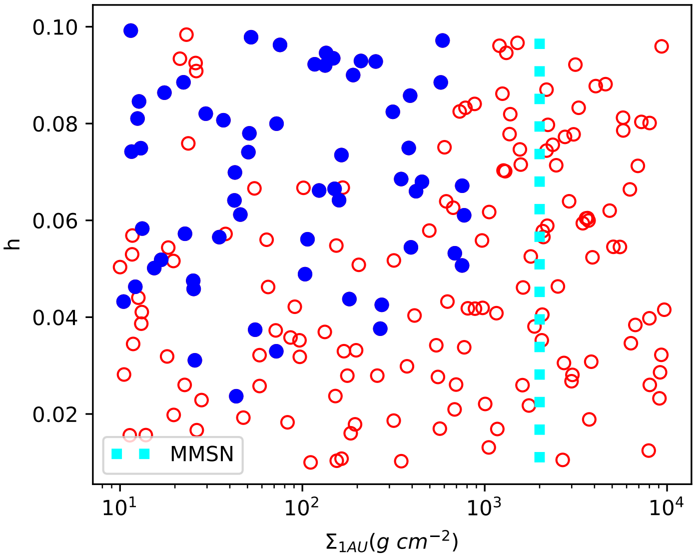

Figure 6.7: Properties of the protoplanetary disk that formed TOI-1136: the total disk surface density and the scale height (h/r) of our disk migration simulation. The successful simulations (blue solid symbols) suggest that the TOI-1136 likely had a lower total surface density ($\Sigma_{\text{total, 1AU}} \lesssim 1000\text{g cm}^{-2}$) than the Minimum-mass Solar Nebula (Hayashi, 1981). The slower migration in a lower density disk facilitated capture into the 7:5 second-order resonance.

(Luger et al., 2017). All of the three-body angles, with coefficients expected from subtracting the pairwise resonances (see Section 4.4) are librating with small amplitude.

The behavior of the two-body angles has not been reported in the literature, but the experience of TOI-1136 suggests that it may be possible to discern their libration. We integrated samples from the posterior distribution of planet masses and orbital elements of (Agol et al., 2021) with the `whfast` integrate in `rebound` for 50 years (Rein & Tamayo, 2015). In contrast to TOI-1136 and K2-19 (Petigura et al., 2020; Petit et al., 2020a), TRAPPIST-1 has excellent TTV coverage and should not suffer from the same eccentricity degeneracies. Nevertheless, the mixed two-body resonant angles are still dynamically relevant, so we compute these for the six pairwise resonances. A typical draw from the posterior is shown in Figure 6.8. The angle for the 8:5 resonance is circulating, while the 5:3 angle is librating with large (~ 90°) amplitude. The angles for the first-order resonance in the outer chain are all librating with small amplitude. The libration centers and amplitudes are given in Table 6.2.

The three-body angles of TRAPPIST-1 have extremely small libration amplitudes, nearly an order of magnitude smaller than those of TOI-1136 (Table 6.1). The higher-order resonances of TRAPPIST-1 are circulating and librating with large amplitude, respectively, whereas the second-

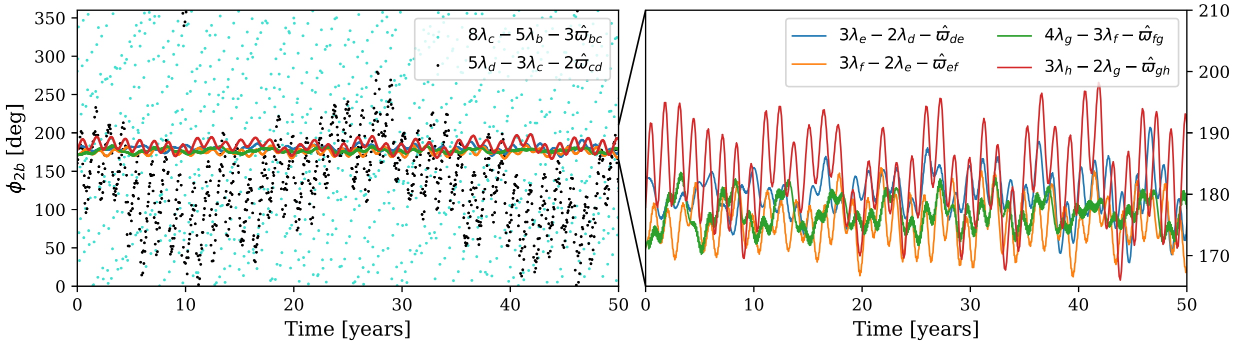

Figure 6.8: Two-body resonant angle evolution for a typical TTV solution of TRAPPIST-1 from Agol et al. (2021). The right panel is a zoomed in version of the left panel omitting ϕ_{bc} and ϕ_{cd}. Note the different axis scales between the panels.

Angle	Libration center	Libration amplitude
Two-body resonant angles		
$\phi_{bc} = 8\lambda_c - 5\lambda_b - 3\hat{\varpi}_{bc}$	*Circulating*	*Circulating*
$\phi_{cd} = 5\lambda_d - 3\lambda_c - 2\hat{\varpi}_{cd}$	143.82° ± 5.71°	88.60° ± 16.80°
$\phi_{de} = 3\lambda_e - 2\lambda_d - \hat{\varpi}_{de}$	180.06° ± 0.03°	7.46° ± 1.79°
$\phi_{ef} = 3\lambda_f - 2\lambda_e - \hat{\varpi}_{ef}$	175.54° ± 0.04°	6.36° ± 0.79°
$\phi_{fg} = 4\lambda_g - 3\lambda_f - \hat{\varpi}_{fg}$	176.87° ± 0.05°	7.30° ± 0.13°
$\phi_{gh} = 3\lambda_h - 2\lambda_g - \hat{\varpi}_{gh}$	182.90° ± 0.07°	14.38° ± 4.91°
Three-body resonant angles		
$\phi_{bcd} = 2\lambda_b - 5\lambda_c + 3\lambda_d$	195.51° ± 0.43°	11.68° ± 0.32°
$\phi_{cde} = \lambda_c - 3\lambda_d + 2\lambda_e$	315.25° ± 0.91°	20.09° ± 0.83°
$\phi_{def} = 2\lambda_d - 5\lambda_e + 3\lambda_f$	150.86° ± 0.16°	8.54° ± 0.18°
$\phi_{efg} = \lambda_e - 3\lambda_f + 2\lambda_g$	78.70° ± 0.04°	3.05° ± 0.04°
$\phi_{fgh} = \lambda_f - 2\lambda_g + \lambda_h$	180.16° ± 0.02°	2.84° ± 0.07°

Table 6.2: Resonant angles in TRAPPIST-1, calculated using the posterior of Agol et al. (2021). The two-body angles for the first-order resonances, as well as all of the three-body angles, are librating with small amplitudes. The two-body angles for the 8:5 and 5:3 resonances are circulating and librating with a large amplitude, respectively

order resonance in TOI-1136 is librating with smaller amplitude. To an extent, these differences may be a consequence of measurement uncertainties: if the posterior distribution is larger in parameter space than the region enclosed by the true trajectory (which is indeed very small for a near-equilibrium system), the inferred libration amplitude will be too large (Jensen & Millholland, 2022).

Nevertheless, if we assume that measurement uncertainty is not the dominant effect, we can draw some conclusions from this variation between the two systems. Capture into MMR due to Type I migration requires libration of the two-body resonant angle to ensure the planets can distribute the disk torques and migrate together. The three-body resonances, appearing at higher order in mass, are more of a consequence of adjacent MMRs rather than drivers of the dynamics themselves, at least in the protoplanetary disk (Quillen, 2011, Chapter 4). Post-disk evolution is very different. Weaker effects, including tidal dissipation and planetesimal scattering, often preserve the three-body libration even if the two-body angles no longer librate. These two facts together suggest that while the architecture of TOI-1136 is mostly untouched from the disk phase, TRAPPIST-1 has undergone considerable post-disk evolution to achieve its current resonant architecture.[5] Even more telling is that the three-body angle for TRAPPIST-1 bcd is also compatible with 3:2 resonances between both pairs, implying that the current state is the product of Kepler-221-like evolution along the three-body commensurability (Chapter 4).

6.6 Discussion

TOI-1136 joins a handful of known planetary systems with a resonant chain: GJ 876 (Rivera et al., 2010; Millholland et al., 2018), TRAPPIST-1 (Gillon et al., 2017; Luger et al., 2017; Agol et al., 2021), TOI-178 (Leleu et al., 2021a), Kepler-80 (MacDonald et al., 2016), Kepler-60 (Goździewski et al., 2016), K2-138 (Christiansen et al., 2018), Kepler-223 (Mills et al., 2016), and Kepler-221 (Goldberg & Batygin, 2021). The orbital periods of adjacent planets in TOI-1136 lie extremely close ($\Delta \sim 10^{-4}$) to MMR, a property shared only with other resonant chain systems such as Kepler-60 (Goździewski et al., 2016; Jontof-Hutter et al., 2016) and Kepler-223 (Mills et al., 2016). Our TTV analysis demonstrates that most, if not all, of the 2- and 3-body resonant angles are librating (near their theoretically predicted values) and the dynamics of the system are driven by mean-motion resonant interactions.

TOI-1136 is the first known resonant chain with a second-order MMR between neighboring first-order MMR. Several other systems have unconfirmed second-order resonances: Kepler-29 b and c have a period ratio that deviates from a 9:7 MMR at a 10^{-4} level (Fabrycky et al., 2012; Jontof-Hutter et al., 2016), however existing TTV could not determine if the system is in resonance (Migaszewski

---

[5] To be more precise, TRAPPIST-1 is not consistent with the standard Type I paradigm of migration and eccentricity damping of each planet from a smooth disk. See Pichierri et al., in prep.

et al., 2017; Vissapragada et al., 2020). TOI-178 b is near a second-order 5:3 MMR with planet c (Leleu et al., 2021a). However, the period ratio is shorter than expected if the system was resonant (1.95 day vs. 1.91 day). Leleu et al. (2021a) suspected that tidal dissipation might have broken planet b away from resonance. In TRAPPIST-1, the inner three planets are close to third-order (8:5) and second-order (5:3) MMR; the 5:3 angle appears to librate with large amplitude (Section 6.5). TOI-1136 is a very rare case — possibly unique among the known systems — a resonant chain with a second-order MMR between first-order resonances.

TOI-1136 is the second known resonant-chain system with a well-established age as young as a few hundred million years. The other system is Kepler-221, with an age of about 600 Myr (Chapter 4). The rest of the resonant-chain systems are at least several Gyr old or have no precise age estimates. TOI-1136 and Kepler-221 seem to have had disparate evolution tracks despite similar ages. In Kepler-221, although the pairwise orbital period ratios (2.02 and 3.23) are farther from commensurability than in TOI-1136, the 3-body resonant angle changes so slowly (small B, Figure 6.5) that it is most likely librating. The interpretation offered in Chapter 4 is that Kepler-221 underwent rapid tidal resonant repulsion, possibly with the help of obliquity tides. Chapter 4 estimated a total of $7000\tau_e$ must have elapsed so that the system reached the current state of 10% off resonance. On the other hand, TOI-1136 has barely moved from perfect orbital period commensurability. One possible explanation is that the conditions for capturing planets into a Cassini state (Millholland & Laughlin, 2019) were simply not available for TOI-1136. Its resonant repulsion has to proceed with the much slower eccentricity tides. Based on the preceding argument, Kepler-223 (not to be confused with Kepler-221, Mills et al., 2016) may represent the future of TOI-1136. Kepler-223 is about 6 Gyr old, and its four transiting planets are likely in a 4-body resonant chain that only involves first-order MMR. Despite its 6-Gyr age, Kepler-223 seems to have avoided giant impact collisions, resonant repulsion, and planetesimal scattering, any of which could have induced deviations from MMR. Its orbital period ratios are still deep in resonance (1.3336, 1.5015, and 1.3339).

TOI-1136 probably still preserves a "pristine" orbital architecture from convergent disk migration. It may be a precursor of many of the *Kepler* near-resonant multi-planets before dynamical evolution eventually dislodged the planets from perfect resonance over Gyr timescale. No spectroscopic, AO, visual, or comoving stellar companion was detected for TOI-1136. The low stellar obliquity, coupled with the coplanarity, and dynamical fragility of a resonant chain of planets, point to the formation of TOI-1136 in an isolated disk with no stellar fly-by, disk warp or significant axial asymmetry.

Our disk migration simulations favor Type-I migration with an inner disk edge for TOI-1136. The edge helps to halt the migration the planets and converts divergent encounters into convergent ones.

To lock the ef pair into a 7:5 second-order MMR, the disk has to be less dense than than the MMSN and only weakly damp eccentricity. Resonant repulsion simulations further indicate that TOI-1136 has undergone minimum tidal dissipation since its formation.

Fast forwarding to a ∼5-Gyr-old mature planetary system, multiple evolutionary paths are possible for TOI-1136. If it only experiences negligible dynamical evolution, it may remain deeply resonant, comparable to the 6-Gyr-old Kepler-223 (Mills et al., 2016). If tides or planetesimal scattering are important, it will undergo mild resonant repulsion and join the population of near-resonant (Δ = 1-2%), multi-planet *Kepler* systems (e.g., Jontof-Hutter et al., 2016; Hadden & Lithwick, 2017). K2-138 (Christiansen et al., 2018) is a clear example of this architecture, hosting 5 planets near 3:2 resonance with $\Delta = 1 - 3\%$. Finally, if the future dynamical evolution of TOI-1136 is more violent, orbital instability and giant impact collision (Izidoro et al., 2017; Goldberg & Batygin, 2022) may totally disrupt the resonance in TOI-1136. It will then end up as the sort of non-resonant planetary system that dominates the mature *Kepler* multi-planet sample.

Chapter 7

CHAOTIC TIDES AS A SOLUTION TO THE HYPERION PROBLEM

7.1 Introduction

Much like miniature planetary systems, the regular satellites of Saturn are expected to have originated on nearly coplanar and circular orbits within the circumplanetary disk or the planet's rings. Since their formation, tidal dissipation within Saturn has caused the moons to migrate outwards and encounter mean-motion resonances with each other. In some cases, pairs of moons captured into these mean-motion resonances and remain there today, while in others there is indirect evidence of the excitation caused by resonant encounters. As such, resonant dynamics offer a unique window into the system's evolutionary past. In the tightly packed inner saturnian system (i.e., interior to Titan), a complex web of resonances sets strict constraints on the relative migration of each moon (Ćuk et al., 2016a; Ćuk & El Moutamid, 2023). In contrast with the well-understood dynamical history of the inner moons, the Titan–Hyperion system is strikingly enigmatic and one of the most remarkable mysteries of Solar System dynamics.

Hyperion, the only satellite in the large gap between Titan and Iapetus, is trapped in an exterior 4:3 mean-motion resonance with Titan. The origins of this orbital configuration have historically been attributed to an outwardly evolving Titan capturing Hyperion into commensurability (Colombo et al., 1974). This scenario is accompanied by specific consequences: preservation of the adiabatic invariant (Henrard, 1982) implies that, assuming no dissipation within Hyperion, Titan must migrate 4% in semi-major axis post-capture (Ćuk et al., 2013) and thus the tidal Q of Saturn must be $Q_{♄} < 1500$.[1]

There are, however, contradicting constraints on Titan's migration from Iapetus, the outermost regular satellite of Saturn. Iapetus lies just 0.4% inside the 5:1 mean-motion resonance with Titan, implying a recent but significant dynamical interaction between the moons. During the 5:1 resonant encounter, the eccentricity and inclination of Iapetus evolve chaotically and Titan's migration must be rapid enough to avoid ejecting Iapetus (Ćuk et al., 2013; Polycarpe et al., 2018). Evidently, the preservation of Iapetus necessitates rapid migration of Titan, while Hyperion's resonance demands slow, short-range migration.

Hyperion's rotational properties are equally remarkable, and constitute a unique example of stochastic rotation in the Solar System. Wisdom et al., 1984 predicted that it would be in a chaotically

---

[1] However, too much migration of Titan is problematic: if Saturn has especially strong dissipation ($Q_{♄} < 500$), Titan and Hyperion would have started wide of the 3:2 resonance and captured into the wrong resonance.

tumbling state before its rotation was directly observed. They argued that given its moderate eccentricity ($e \approx 0.1$) and highly elongated shape (seen in Voyager 2 images), regular rotation in the synchronous (1:1) or 3:2 spin-orbit state is impossible. Instead, a chaotic zone surrounds the 1:1 and 2:1 spin-orbit resonances and Hyperion's spin vector evolves over timescales of a few orbital periods. In addition, Wisdom et al., 1984 demonstrated that much of the parameter space is attitude unstable, so that an initial small obliquity is quickly amplified and rotation inevitably occurs on all three axes. Early ground-based light curve observations by Klavetter, 1989 confirmed non-periodic rotation and suggested rotation at roughly the synchronous rate.

Despite the remarkable predictive power of Wisdom et al., 1984's calculations, images and light curves taken during the Voyager 2 and Cassini visits to the saturnian system demonstrated that Hyperion was rotating much faster than expected: roughly 4.2 times the synchronous rate (Thomas et al., 1995; Harbison et al., 2011). Rotation mostly occurs around the longest axis and is quasi-regular. Nevertheless, the wobble and precession are indeed clearly chaotic, with typical Lyapunov times of several orbital periods, as measured by Black et al. (1995) and Harbison et al. (2011). Using numerical simulations, Black et al., 1995 showed that this state was not an unexpected outcome—initialized near the synchronous state, Hyperion would irregularly alternate between slower chaotic tumbling and more rapid quasi-regular rotation, the latter being the state actually observed by Klavetter (1989) and Harbison et al. (2011).

In light of the discrepancies between the predicted rotational behavior of Hyperion and its observed state, as well as an unclear relationship between the Titan migration rate and the Titan-Hyperion mean-motion resonance, a complete understanding of the Hyperion problem remains elusive. Previous work has generally considered the rotation to be solely a *consequence* of the orbit and neglected the impact of dissipation within Hyperion on its orbital evolution. We argue that tidal dissipation within Hyperion is non-negligible due to its rapid rotation, and in fact mediates its orbital eccentricity growth despite resonant forcing from Titan's migration. As a result, several fine-tuning problems are avoided and the tidal quality factor of Hyperion can be estimated. We begin in Section 7.2 by studying the chaotic and quasi-regular rotation of Hyperion and calculating the resulting tidal dissipation. Then, in Section 7.3, we use this new picture of dissipation within Hyperion to set constraints on the range and rate of Titan's outward migration. Finally, Section 7.4 discusses the implications of this proposed dynamical history of Hyperion.

7.2 Rotational Dynamics of Hyperion

Numerical procedure

To investigate its rotational dynamics, we numerically modeled the spin and orientation of Hyperion under the effect of Saturn's gravity. The satellite is assumed to be in a fixed elliptical orbit around

Saturn with eccentricity e and true anomaly f. The units are chosen such that the semi-major axis a is unity, the orbital period is 2π, and $GM_♄ = 1$, where $M_♄$ is the mass of Saturn. Hyperion is modeled as an ellipsoid with principal moments of inertia $A < B < C$ and its spin is represented by ω_a, ω_b, and ω_c, the projections of the spin vector on the principal axes, so that the total spin rate is $|\omega| = \sqrt{\omega_a^2 + \omega_b^2 + \omega_c^2}$. The spins evolve according to Euler's equations,

$$\dot{\omega}_a = \frac{B-C}{A}\left(\omega_b\omega_c - \frac{3}{r^3}\beta\gamma\right) \tag{7.1}$$

$$\dot{\omega}_b = \frac{C-A}{B}\left(\omega_c\omega_a - \frac{3}{r^3}\gamma\alpha\right) \tag{7.2}$$

$$\dot{\omega}_c = \frac{A-B}{C}\left(\omega_a\omega_b - \frac{3}{r^3}\alpha\beta\right) \tag{7.3}$$

in which the external torque is provided by the gradient of the gravitational field of Saturn (Murray & Dermott, 1999). Here, r is the instantaneous Hyperion–Saturn distance and α, β, and γ are the direction cosines between the principal axes and the direction of Saturn.

To represent the orientation of Hyperion, we use the quaternion formalism, which avoids the coordinate singularities that appear when using Euler angles (Mel'nikov, 2020). The four quaternion components λ_0, λ_1, λ_2, and λ_3 are normalized and evolve according to (Arribas et al., 2006)

$$\dot{\lambda}_0 = \frac{1}{2}(-\lambda_1\omega_a - \lambda_2\omega_b - \lambda_3\omega_c) \tag{7.4}$$

$$\dot{\lambda}_1 = \frac{1}{2}(\lambda_0\omega_a - \lambda_3\omega_b + \lambda_2\omega_c) \tag{7.5}$$

$$\dot{\lambda}_2 = \frac{1}{2}(\lambda_3\omega_a + \lambda_0\omega_b - \lambda_1\omega_c) \tag{7.6}$$

$$\dot{\lambda}_3 = \frac{1}{2}(-\lambda_2\omega_a + \lambda_1\omega_b + \lambda_0\omega_c). \tag{7.7}$$

The direction cosines are given by

$$\alpha = (\lambda_0^2 + \lambda_1^2 - \lambda_2^2 - \lambda_3^2)\cos f + 2(\lambda_0\lambda_3 + \lambda_1\lambda_2)\sin f \tag{7.8}$$

$$\beta = 2(\lambda_1\lambda_2 - \lambda_0\lambda_3)\cos f + (\lambda_0^2 - \lambda_1^2 + \lambda_2^2 - \lambda_3^2)\sin f \tag{7.9}$$

$$\gamma = 2(\lambda_0\lambda_2 + \lambda_1\lambda_3)\cos f + 2(-\lambda_0\lambda_1 + \lambda_2\lambda_3)\sin f. \tag{7.10}$$

We use the moment of inertia parameters $A = 0.314$, $B = 0.474$, $C = 0.542$ estimated by Harbison et al., 2011 from a Cassini shape model. We then numerically integrate Eqs. 7.1–7.7 with a fifth-order Radau IIA method using relative and absolute tolerances of 10^{-6} and 10^{-10}, respectively. We ran 10 integrations for 3×10^6 orbits with orbital eccentricities ranging uniformly in log-space from 0.01 to 0.631. Each was started at synchronous rotation ($|\omega| = 1$) but with an obliquity of 1° to induce tumbling (Black et al., 1995). Although wobble damping (Burns & Safronov, 1973;

Wisdom, 1987) may be relevant on such long timescales, the purpose of these simulations is to determine the range of typical rotational dynamics; long integrations are more likely to capture rare behavior and less likely to be trapped in “small tributaries of the chaotic zone,” as noticed by Wisdom (1987). For comparison, we also integrated the rotation of Hyperion from its observed state on 2005–06–10 for 10^3 orbits, using the orientation and spin vectors reported by Harbison et al., 2011.

Rotational evolution of Hyperion

One example of the longer integrations is shown in Figure 7.1, where we have chosen $e = 0.1$. Hyperion begins in a chaotic tumbling state, shaded in orange on the plot, but intermittently passes through quasi-regular states, shaded in blue. As noted by Black et al., 1995, quasi-regular states are typically associated with rotation primarily on axes a or c (b is not stable owing to the intermediate axis theorem). The right panel of Figure 7.1 shows the distribution of angular speeds in these two regimes. Chaotic tumbling is smoothly distributed across all values of $|\omega| \lesssim 5$. However, quasi-regular rotation is faster and dominated by peaks at discrete values of $|\omega|$ that correspond to half-integer spin-orbit resonances. At higher $|\omega|$, the peaks lie slightly wide of exact resonance. In particular, the state of Hyperion in 2005 (shaded in gray) matches the highest peak, which appears to be associated with the $9/2$ resonance.

The clustering behavior near spin-orbit resonance is probably a consequence of the resonant “sticking” effect (Karney, 1983; Meiss, 1992; Shevchenko, 1999). In the vicinity of the separatrix that bounds large resonant islands, there are numerous small islands of secondary resonances. Chaotic trajectories which wander near the separatrix may be caught in one of these islands, which necessarily lie in proximity to the resonance. The trajectory will then evolve very slowly through action space and the rotation will be in a quasi-regular state for an extended duration.

Simulations at other eccentricities were qualitatively similar to the $e = 0.1$ case. Alternation between chaotic tumbling and quasi-regular rotation near spin-orbit resonances was observed at all the eccentricities we tested. The tumbling state accounted for 30–60% of the total duration, with no clear dependence of that fraction on eccentricity.

However, the typical rotation speed in the long integrations shows a strong dependence on orbital eccentricity (Wisdom, 1987; Quillen et al., 2020). Denoting the time average of $|\omega|$ as $\langle\omega\rangle$, the typical $\langle\omega\rangle$ was much higher for higher e during both chaotic tumbling and quasi-regular rotation. Figure 7.2 shows the $\langle\omega\rangle$ as a function of eccentricity for the long simulations. We also computed the mean $\langle\omega\rangle$ during the chaotic tumbling only, by removing the times with quasi-regular motion as in Figure 7.1. Both are fit well by an exponential dependence on e. Without removing quasi-regular motion, we find $\langle\omega\rangle \approx 2.59 \times 1.42^{e/0.1}$. Considering chaotic tumbling only, we obtain

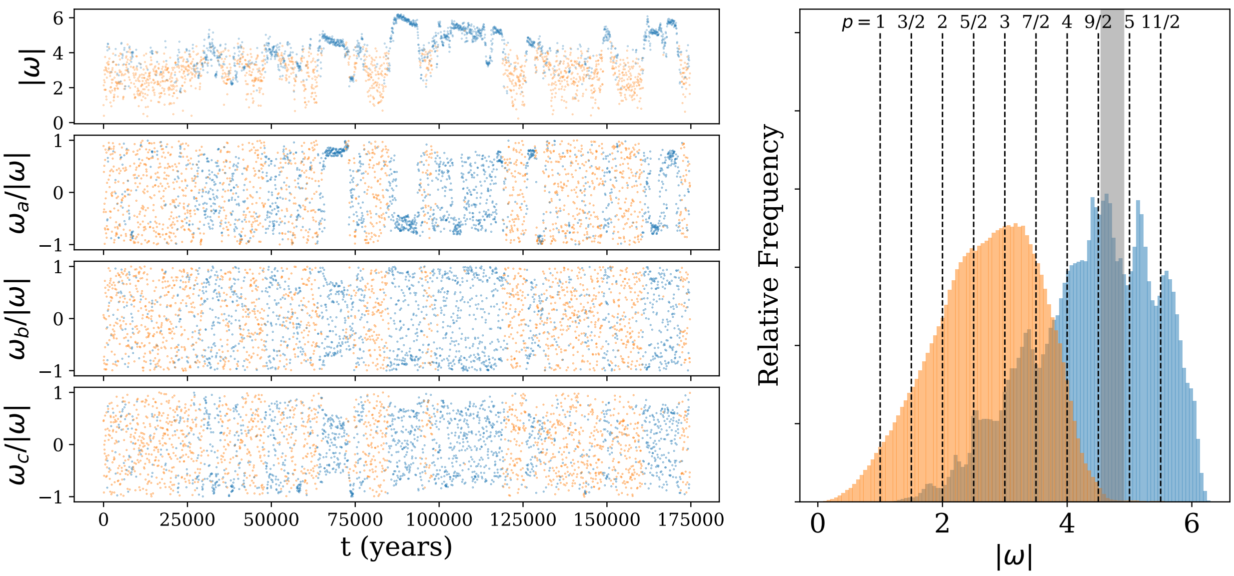

Figure 7.1: A typical integration of the rotational equations of Hyperion for 3×10^6 orbits, starting from a nearly synchronous state and a realistic orbital eccentricity of 0.1. Left: Spin vector magnitude and projections onto each principal axis. Chaotic tumbling (shaded orange) intermittently gives way to quasi-regular rotation (blue). Right: the distribution of $|\omega|$ in each state. The two distributions are shown to scale relative to each other. Dashed vertical lines mark spin-orbit resonances. The shaded gray region is the 2σ range of Hyperion's rotation speed in its observed state in 2005.

$\langle \omega \rangle \approx 2.03 \times 1.38^{e/0.1}$. Finally, for reasons that will become apparent in Section 7.2, we fit the fourth root of the time average of $|\omega|^4$ as a function of e in the same way, finding $\langle \omega^4 \rangle^{1/4} \approx 2.88 \times 1.37^{e/0.1}$ and $\langle \omega^4 \rangle^{1/4} \approx 2.27 \times 1.38^{e/0.1}$ for all rotation and chaotic tumbling, respectively.

Analytical rotation model

To qualitatively understand the eccentricity dependence of $\langle \omega \rangle$ seen in our simulations, it is instructive to consider a simplified one-dimensional model of Hyperion's spin, even though its rotation is fully three-dimensional. This simplification ignores the obliquity and spin precession of Hyperion, but can be studied analytically in much more detail. Following Wisdom et al., 1984, assume the satellite's spin axis is perpendicular to its orbital plane. The orientation of the satellite in the inertial frame is given by θ. Then, θ evolves according to

$$\frac{d^2\theta}{dt^2} + \frac{\omega_0^2}{2r^3} \sin 2(\theta - f) = 0 \tag{7.11}$$

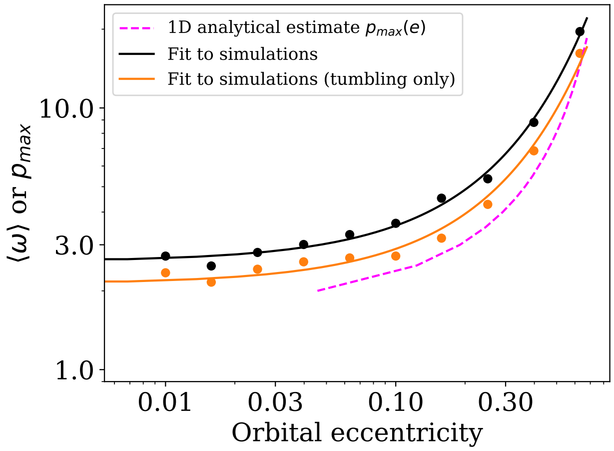

Figure 7.2: Average rotation speed of Hyperion as a function of its orbital eccentricity. Black dots are the full long integrations and the black line is an fit with an exponential dependence on eccentricity. Orange is the same but considering only the chaotic tumbling state, removing the quasi-regular rotation (see Figure 7.1). The magenta curve is the analytical estimate of p_{max} from solving Eq. 7.14. The analytic solution, despite being offset from the numerical results by a factor of ~ 2, captures the qualitative behavior of $\langle\omega\rangle$ as a function of e.

where $\omega_0^2 = 3(B - A)/C$ (Goldreich & Peale, 1966). Equation 7.11 is unwieldy because r and f are complicated functions of time. However, it can be expanded via a Fourier series into

$$\frac{d^2\theta}{dt^2} + \frac{\omega_0^2}{2} \sum_{p=-\infty}^{\infty} H(p, e) \sin(2\theta - 2pt) = 0 \tag{7.12}$$

where p is a half-integer and the $H(p, e)$ are coefficients given by

$$H(p, e) = \frac{1}{2\pi} \int_0^{2\pi} \frac{1}{r^3} \cos(2pt - 2f)dt, \tag{7.13}$$

which, for $e \ll 1$ and $p \lesssim 5$ is of order $H(p, e) \sim 2^{2p-1} e^{2p-2}$ (Dobrovolskis, 1995). As is well-known (Goldreich & Peale, 1966), Equation 7.12 points at the existence of a discrete set of spin-orbit resonances in which $d\theta/dt \approx p$. For example, the 3:2 spin-orbit state of Mercury corresponds to $p = 3/2$, or three rotations (in the inertial frame) for every two orbits (Goldreich & Peale, 1966). The half-width of the spin-orbit resonance in frequency space is $\omega_0\sqrt{H(p, e)}$, increasing with e and decreasing with p. According to the resonance overlap criterion (Chirikov, 1979), chaotic behavior arises when neighboring resonances, (whose widths can be calculated to leading order as if they were unperturbed by each other), would overlap. Thus, chaos will appear around the p and $p + 1/2$ resonances if

$$\omega_0\sqrt{H(p, e)} + \omega_0\sqrt{H(p + 1/2, e)} \gtrsim \frac{1}{2}. \tag{7.14}$$

Wisdom et al., 1984 use Eq. 7.14 and the two widest resonances, $p = 1$ and $p = 3/2$, to generate a general condition for the existence of a broad chaotic region and argue that Hyperion must be in it.

Turning this argument around, we can also ask, for a given e and ω_0, what is the highest $p_{\max}$ for which resonances overlap such that there is a chaotic sea surrounding the $p_{\max}$ and $p_{\max} + 1/2$ resonances? Because of the dependence of $H(p, e)$ on p, the chaotic sea will also extend for at least $1 \leq p \leq p_{\max} + 1/2$, and a trajectory initialized near $p = 1$ will eventually explore up to $p_{\max}$ ergodically. We solve Eq. 7.14 numerically for e by selecting a $p_{\max}$ and taking $\omega_0 = 0.94$, corresponding to the values of (A, B, C) we used in the 3D simulations. The result is shown as the magenta curve in Figure 7.2. The expression for $H(p, e)$ ensures that the size of the chaotic sea, and thus $p_{\max}$, grow steeply with e (Wisdom, 1987). Our analytical model closely matches the steep dependence on e found in the numerical simulations, although the 1D model consistently underestimates $\langle\omega\rangle$. Evidently, the chaotic region is larger in 3D, and thus emerges at a smaller eccentricity for a given p. Indeed, the notion that the onset of chaos occurs earlier in systems with more degrees of freedom is qualitatively expected (see, e.g., Morbidelli, 2002).

The steep dependence of Hyperion's rotation on its orbital eccentricity has an important consequence. Hyperion's eccentricity is resonantly excited by an outwardly migrating Titan, and in the absence of additional forces, increases monotonically. Hence, we expect that the spin rate of Hyperion has *grown* over time, in contrast to most bodies in the Solar System.

Tidal dissipation

Some of the energy of the time-varying tidal torque is dissipated within Hyperion. The two main effects of the dissipation are despinning and eccentricity damping. The despinning timescale at the present orbit is roughly of the order the age of the Solar System (Wisdom et al., 1984). The eccentricity damping timescale is usually much larger than the despinning timescale and has therefore been ignored for Hyperion. We will examine this in more detail.

For a synchronously rotating satellite with low eccentricity, the eccentricity damping rate is given by

$$\tau_{e,\mathrm{sync}}^{-1} \equiv -\frac{1}{e}\frac{de}{dt} = \frac{21}{2}\frac{k_{2,\mathrm{H}}}{Q_{\mathrm{H}}}\frac{M_{♄}}{M_{\mathrm{H}}}\left(\frac{R_{\mathrm{H}}}{a_{\mathrm{H}}}\right)^5 n_{\mathrm{H}} \tag{7.15}$$

where $k_{2,\mathrm{H}}$ is the tidal Love number of Hyperion, Q_{H} is its tidal quality factor, R_{H} is the average radius of Hyperion, and M_{H}, a_{H} and n_{H} are the mass, semi-major axis and mean motion of Hyperion, respectively (Goldreich & Soter, 1966). While the exact values of $k_{2,\mathrm{H}}$ and Q_{H} are unknown, Hyperion is believed to be a rubble pile with high internal porosity (Thomas et al., 2007). Goldreich & Sari, 2009 suggest that for such an object, $k_{2,\mathrm{H}} \lesssim 1 \times 10^{-3}$ and $Q_{\mathrm{H}} \lesssim 100$. Assuming $k_{2,\mathrm{H}}$ is at the upper bound, $R_{\mathrm{H}} = 150$ km, $M_{♄}/M_{\mathrm{H}} = 1.0 \times 10^8$, and Hyperion's current period of 21.28 d, we obtain

$$\tau_{e,\mathrm{sync}} \approx 8 \times 10^{13} \left(\frac{Q_\mathrm{H}}{100} \right) \mathrm{yr}, \tag{7.16}$$

much longer than the age of the Solar System.

However, Hyperion is manifestly *not* rotating synchronously. In non-synchronous rotation, the entirety of the tide is raised and lowered during one cycle, greatly enhancing the dissipation of energy. Burns & Safronov, 1973 argue that the energy dissipated in a non-synchronous rotator per orbit is, to an order of magnitude,

$$\Delta E \sim \frac{|\omega|^4 R_\mathrm{H}^5}{G} \frac{k_{2,\mathrm{H}}}{Q_\mathrm{H}} \tag{7.17}$$

where we have written the equation in terms of $k_{2,\mathrm{H}}$ rather than the rigidity (Goldreich & Sari, 2009). Energy dissipated during chaotic tumbling should be at least comparable to, if not much larger than this estimate (Wisdom, 1987; Brasser, 2020). Because angular momentum is conserved, this dissipation must drive circularization of the orbit, and thus the eccentricity damping rate for Hyperion's irregular rotation, $\tau_{e,\mathrm{H}}^{-1}$ will be enhanced over the synchronous rate by roughly

$$\frac{\tau_{e,\mathrm{H}}^{-1}}{\tau_{e,\mathrm{sync}}^{-1}} \sim \frac{1}{e_\mathrm{H}^2} \frac{\langle \omega^4 \rangle}{n_\mathrm{H}^4}. \tag{7.18}$$

For current values of Hyperion, $e \approx 0.1$ and $\langle \omega^4 \rangle^{1/4} / n_\mathrm{H} \approx 4$ and the enhancement is $\sim 2 \times 10^4$. Quillen et al. (2020) performed simulations of a viscoelastic model of the Martian satellites Phobos and Deimos and confirmed that the energy dissipation rate during episodes of rapid tumbling was larger than the dissipation during synchronous rotation by 3 to 5 orders of magnitude. In their case, the process is naturally quenched as the eccentricity is damped, rotation slows, and the satellites capture into a synchronous state. In contrast, Hyperion's eccentricity is continuously excited by a resonant interaction with Titan (Section 7.3) and rapid rotation does not cease.

With the enhancement from rapid rotation, the expected eccentricity damping timescale of Hyperion is now $\tau_{e,\mathrm{H}} \sim 4 \times 10^9$ yr, of order the age of the Solar System. While this estimate should not be taken to be exact (see Wisdom, 1987) because of order-unity constants dropped by Burns & Safronov, 1973, the result is that circularization of Hyperion's orbit can no longer be ignored despite its considerable distance from Saturn. In addition, because of the exponential dependence of $|\omega|$ on e, the damping timescale varies considerably with e, in contrast to the synchronous timescale, which is independent of e. This is the critical piece coupling Hyperion's rotation to its orbital history.

7.3 Orbital Dynamics of the Titan–Hyperion System

The presence of the 4:3 mean-motion resonance between Hyperion and Titan is usually interpreted as resulting from the outward migration of Titan (Colombo et al., 1974; Ćuk et al., 2013). The resonance has a libration amplitude of 36°, with a forced eccentricity of 0.1, and one possible explanation for this state is the expansion of Titan's orbit by 4% since the initial encounter with the resonance (Ćuk et al., 2013).

In light of the orbital coupling discussed above, however, it is critical to exmaine alternative scenarios. Much in the same manner as the Moon recedes from the Earth due to tides raised on the ocean, Titan migrates outward because it raises a tidal bulge on Saturn. As Saturn rotates faster than Titan orbits, the tidal bulge transfers angular momentum from Saturn's rotation to Titan's orbit. The rate of expansion of Titan's orbit is given by

$$\tau_{a,\mathrm{Ti}}^{-1} = -\frac{1}{a_{\mathrm{Ti}}}\frac{da_{\mathrm{Ti}}}{dt} = -\frac{3k_{2,♄}}{Q_♄(n_{\mathrm{Ti}})}\frac{M_{\mathrm{Ti}}}{M_♄}\left(\frac{R_♄}{a}\right)^5 n_{\mathrm{Ti}} \tag{7.19}$$

where $Q_♄(n)$ is the tidal quality factor of Saturn at forcing frequency n and $k_{2,♄}$ is the Love number of Saturn, which we take to be 0.382 (Lainey et al., 2020; Jacobson, 2022). The sign convention, consistent with Equation 7.15, means that $\tau_{a,\mathrm{Ti}} < 0$ corresponds to outward migration. Quantitative predictions for $Q_♄$ are challenging and highly dependent on Saturn's internal structure (Ogilvie & Lin, 2004). Observationally, $Q_♄(n)$ can be measured by observations of outward migration of the inner saturnian moons (Lainey et al., 2012). Interestingly, recent works have shown that $Q_♄$ is not the same for each of Saturn's moons, with Rhea especially having higher tidal dissipation (Lainey et al., 2017). Indeed, some tidal theories predict that $Q_♄$ should depend on the forcing frequency n, in some cases quite sensitively (Ogilvie & Lin, 2004; Fuller et al., 2016; Terquem, 2021). Therefore, the tidal quality factor relevant for Titan's migration cannot be assumed to be the same as the one measured for another of Saturn's moons.

Recently, two groups have reported conflicting measurements of outward migration of Titan. Lainey et al., 2020 used astrometry and Cassini radio tracking to obtain $Q_♄(n_{\mathrm{Ti}}) = 124^{+26}_{-19}$ (3σ uncertainties) corresponding to a migration timescale of $\tau_{a,\mathrm{Ti}} \approx 10\,\mathrm{Gyr}$. They interpret this result as consistent with the resonant locking model, in which satellites couple to inertial modes within Saturn and migrate outwards as the interior of Saturn evolves over the lifetime of the Solar System. Long-range migration enabled by the resonant locking mechanism is also consistent with the expectation that Titan formed at or migrated to the inner edge of the circumplanetary disk, near a period of $\sim$ 3 d (Batygin et al., 2023). However, such rapid migration is disputed by Jacobson, 2022, who uses a large corpus of tracking, astrometric, and other data to obtain $Q_♄(n_{\mathrm{Ti}}) = 1224 \pm 119$ (1σ uncertainties), or $\tau_{a,\mathrm{Ti}} \approx 100\,\mathrm{Gyr}$, an order of magnitude slower than Lainey et al., 2020.

The capture and evolution of Hyperion in its mean-motion resonance with Titan depends on the specifics of Titan's outward migration. For completeness, we consider two cases below: one in which Titan's migration is consistent with the results of Lainey et al., 2020, and one in which it is consistent with the results of Jacobson, 2022.

Analytical Results

To leading order, the mean motion and eccentricity of Titan and Hyperion near the 4:3 mean-motion resonance evolve according to (e.g., Terquem & Papaloizou, 2019)

$$\dot{n}_{\rm Ti} = \frac{3n_{\rm Ti}}{2\tau_{a,{\rm Ti}}} + \frac{3n_{\rm Ti}e_{\rm Ti}^2}{\tau_{e,{\rm Ti}}} \tag{7.20}$$

$$\dot{n}_{\rm H} = 12n_{\rm H}^2\frac{M_{\rm Ti}}{M_♄}(e_{\rm Ti}f_1\sin\phi_1 + e_{\rm H}f_2'\sin\phi_2) + \frac{3n_{\rm H}e_{\rm H}^2}{\tau_{e,{\rm H}}} \tag{7.21}$$

$$\dot{e}_{\rm Ti} = -\frac{e_{\rm Ti}}{\tau_{e,{\rm Ti}}} \tag{7.22}$$

$$\dot{e}_{\rm H} = -n_{\rm H}\frac{M_{\rm Ti}}{M_♄}f_2'\sin\phi_2 - \frac{e_{\rm H}}{\tau_{e,{\rm H}}} \tag{7.23}$$

where we have assumed that Hyperion's mass and tidal migration rate are negligible. Here, $\phi_1 = 4\lambda_{\rm H} - 3\lambda_{\rm Ti} - \varpi_{\rm Ti}$ and $\phi_2 = 4\lambda_{\rm H} - 3\lambda_{\rm Ti} - \varpi_{\rm H}$ are the critical resonant angles and f_1 and f_2' are order unity constants. To reduce these equations further, we note that the capture into resonance of Hyperion implies that $\dot{n}_{\rm Ti}/n_{\rm Ti} = \dot{n}_{\rm H}/n_{\rm H}$. Additionally, because Titan's pericenter precession is dominated by Saturn's J_2, ϕ_1 circulates and the time average of $\sin\phi_1$ is zero. We thus obtain

$$4\dot{e}_{\rm H}e_{\rm H} = -3e_{\rm H}^2\tau_{e,{\rm H}}^{-1} - \left(\frac{1}{2}\tau_{a,{\rm Ti}}^{-1} + e_{\rm Ti}^2\tau_{e,{\rm Ti}}^{-1}\right) \tag{7.24}$$

which, despite being simpler, must still be integrated numerically because of the distance and eccentricity dependence of the migration and damping timescales. Nevertheless, the competing effects of eccentricity excitation and damping suggest that we can compute an equilibrium eccentricity that Hyperion will tend towards. Setting $\dot{e}_{\rm H} = 0$, we find

$$e_{\rm eq,H}^2 = -\frac{1}{3}\left(\frac{1}{2}\tau_{a,{\rm Ti}}^{-1} + e_{\rm Ti}^2\tau_{e,{\rm Ti}}^{-1}\right)\tau_{e,{\rm H}}. \tag{7.25}$$

Because $e_{\rm Ti} \ll 1$ and for typical tidal processes, $|\tau_e| \sim |\tau_a|$, the second term in the brackets can be neglected. Recalling Eq. 7.18, the equilibrium eccentricity can be translated into an equation for the equilibrium rotation rate of Hyperion,

$$\frac{\langle\omega^4\rangle}{n_{\rm H}^4} \approx -\frac{1}{6}\frac{\tau_{e,{\rm sync}}}{\tau_{a,{\rm Ti}}}. \tag{7.26}$$

With the expected damping of Hyperion (Section 7.2) and the current rotation rate of Hyperion (averaged over the secular eccentricity cycle and the two rotation regimes), $\langle\omega^4\rangle^{1/4}/n_{\rm H} \approx 4$, we find, assuming Hyperion is at its equilibrium eccentricity,

$$Q_{\rm H} \approx 20\left(\frac{|\tau_{a,{\rm Ti}}|}{10^{10}\,{\rm yr}}\right). \tag{7.27}$$

Thus, if Hyperion is at its equilibrium eccentricity, the Lainey et al., 2020 Titan migration measurement implies $Q_\mathrm{H} \sim 20$, while the Jacobson, 2022 value implies $Q_\mathrm{H} \sim 200$. As we will see below, more accurate estimates of Q_H are larger because Hyperion does not typically reach the equilibrium eccentricity.

Numerical results

As a means of testing our analytical theory, we ran a suite of N-body simulations modeling the outward migration of Titan and tidal dissipation of Hyperion resulting from its rapid chaotic tumbling. Previous work has coupled rotational and orbital integrations to study the spin-orbit evolution of irregular satellites (Ćuk et al., 2016b; Quillen et al., 2017; Quillen et al., 2020; Agrusa et al., 2021; Quillen et al., 2022). However, our objective is to demonstrate the feasibility of resonant capture under enhanced tidal damping. Accordingly, we do not repeat the rotational simulations but instead model tidal dissipation with an eccentricity damping term estimated using the results of Section 7.2. Our numerical integrations use the `whfast` symplectic integrator in the `rebound` N-body package (Rein & Tamayo, 2015). The integrator timestep was chosen to be $1/20$ the initial orbital period of Titan. Additional forces for migration and eccentricity damping were incorporated with `reboundx` (Tamayo et al., 2020b). The integration includes the Sun and the J_2 moment of Saturn, to which is added the averaged orbits of the satellites interior to Titan. At each timestep, we compute the eccentricity damping of Hyperion using its instantaneous eccentricity, e_H. To accomplish this, we estimate the average rotation speed, $\langle\omega^4\rangle^{1/4} \approx 2.88\times1.37^{e_\mathrm{H}/0.1}$ (Section 7.2), and then use Eqs. 7.15 and 7.18 to determine the enhanced eccentricity damping timescale, $\tau_{e,\mathrm{H}}$. We also compute the migration rate and eccentricity damping rate of Titan at each timestep according to the prescriptions specified in the following sections. Then, during each "kick" step of the `whfast` algorithm, we apply an additional force to each satellite of

$$\boldsymbol{a}_\mathrm{damp,Ti} = -2\frac{(\boldsymbol{v}_\mathrm{Ti}\cdot\boldsymbol{r}_\mathrm{Ti})\boldsymbol{r}_\mathrm{Ti}}{(\boldsymbol{r}_\mathrm{Ti}\cdot\boldsymbol{r}_\mathrm{Ti})\tau_{e,\mathrm{Ti}}} - \frac{\boldsymbol{v}_\mathrm{Ti}}{2\tau_{a,\mathrm{Ti}}} \tag{7.28}$$

$$\boldsymbol{a}_\mathrm{damp,H} = -2\frac{(\boldsymbol{v}_\mathrm{H}\cdot\boldsymbol{r}_\mathrm{H})\boldsymbol{r}_\mathrm{H}}{(\boldsymbol{r}_\mathrm{H}\cdot\boldsymbol{r}_\mathrm{H})\tau_{e,\mathrm{H}}} \tag{7.29}$$

where $\boldsymbol{r}_i$ and $\boldsymbol{v}_i$ are the radius and velocity vector of the particle relative to Saturn, respectively (Papaloizou & Larwood, 2000).

The simulation initial conditions were chosen to be compatible with available constraints. Although the age of Hyperion is not known precisely, its low orbital inclination implies that it, or its parent object, formed in the circumplanetary disk. High crater densities are also consistent with the notion that Hyperion is quite old (Plescia & Boyce, 1983; Bottke et al., 2023). We thus ran the simulations over a timespan of 4.5 Gyr. Hyperion was placed exterior to Titan with an initial period ratio of 1.35 in order to avoid capture into the wrong resonance. The initial eccentricity was varied between

0 and 0.05 and the initial inclination was set to 0 relative to Saturn's equator. The other orbital angles were randomized uniformly.

It is important to note that the measurements of Lainey et al., 2020 and Jacobson, 2022 are only of Titan's current migration rate (baselines of $\approx 150\,\mathrm{yr}$) and are not necessarily representative of the previous behavior of Titan. Accordingly, we attempt to construct a reasonable migration history of Titan in each case and include that in the simulation as described below. To ensure feasible computational times, we sped up integrations by dividing the migration timescale of Titan and the eccentricity damping timescales of Titan and Hyperion by a common factor of 10^4. We do not expect this to impact our results because the accelerated migration and damping timescales still greatly exceed the other dynamical timescales in this problem (which are $\lesssim 100\,\mathrm{yr}$), ensuring that adiabaticity during the resonant encounter is preserved.

Rapid Titan Migration

First, we assume to be true the results of Lainey et al., 2020, who find $\tau_{a,\mathrm{Ti}} \approx -10\,\mathrm{Gyr}$ and argue that Titan is in a 'resonant lock' with an internal mode of Saturn (Fuller et al., 2016). In such a regime, the migration of Titan is set by the interior evolution of Saturn, which unfolds roughly on the timescale of its age. Following Lainey et al., 2020, we hypothesize

$$\tau_{a,\mathrm{Ti}}^{-1} \approx -\frac{B}{t} \tag{7.30}$$

where, to match the current $\tau_{a,Ti}$ measurement, $B \sim 1/3$. This equation has the solution

$$a_{\mathrm{lock}}(t) = a_0 \left(\frac{t}{t_0}\right)^B \tag{7.31}$$

where a_0 is Titan's current semi-major axis and t_0 is Saturn's age. Of course, Eq. 7.31 cannot be strictly true, because $a_{\mathrm{lock}}(0) = 0$. Instead, a likely scenario is that Titan formed at an initial semi-major axis a_i and remained there until some time t_{lock}, upon which point it caught into the resonant lock and Eq. 7.31 applies. Although t_{lock} (equivalently a_i) is unknown, we find that our results do not depend significantly on its value.

As initial conditions, we choose $t_{\mathrm{lock}} = 1, 2$ or 3 Gyr, which correspond to an initial Titan semi-major axis of $12.28, 15.47$, and $17.71 R_{♄}$, respectively, and an initial Titan eccentricity of 0.04. Titan migration occurs when $t > t_{\mathrm{lock}}$, and we set the migration timescale to $\tau_{a,\mathrm{Ti}} = -3t$ according to Eq. 7.30. The true eccentricity damping timescale of Titan is unknown, but is expected to be of the same order as the migration timescale (Fuller et al., 2016). Accordingly, we set $\tau_{e,\mathrm{Ti}} = \tau_{a,\mathrm{Ti}}$, so that Titan's final eccentricity is closed to its observed value of 0.029.

The simulations consistently capture Hyperion into the observed 4:3 resonant configuration with $e_H \approx 0.1$ if $Q_{\mathrm{H}} \approx 40$. The final eccentricity does not depend strongly on t_{lock}. Figure 7.3 shows two

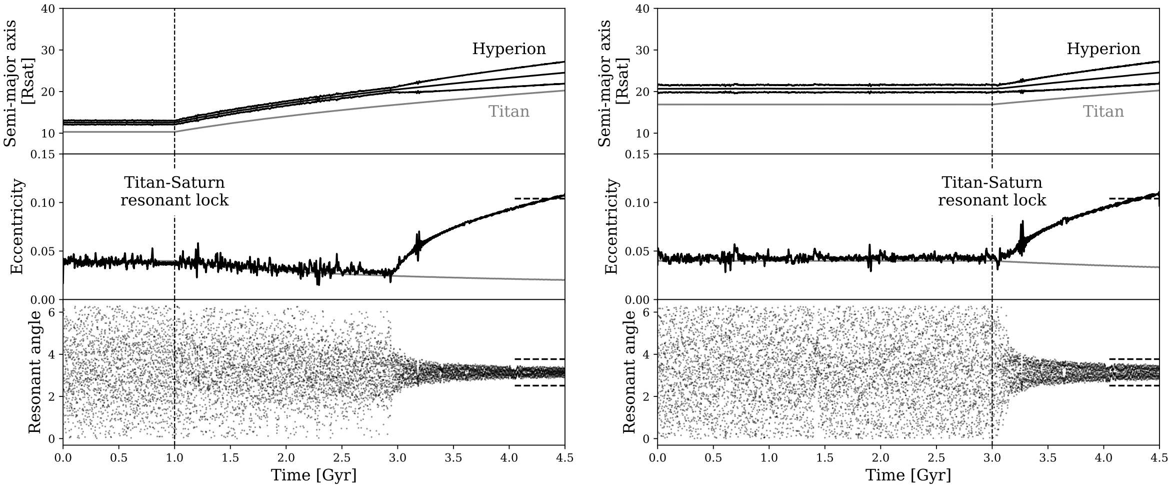

Figure 7.3: Capture of Hyperion into 4:3 resonance with Titan in the migration-by-resonant locking model. In both panels we have assumed $Q_{\mathrm{H}} = 40$, on the left $t_{\mathrm{lock}} = 1\,\mathrm{Gyr}$ and on the right $t_{\mathrm{lock}} = 3\,\mathrm{Gyr}$. The resonant angle plotted in the bottom panel is $\phi_2 = 4\lambda_{\mathrm{H}} - 3\lambda_{\mathrm{Ti}} - \varpi_{\mathrm{H}}$. Dashed lines in the bottom two rows show the measured values of Hyperion's (forced) eccentricity and libration angle range.

of these integrations where we have used $Q_{\mathrm{H}} = 40$ and $t_{\mathrm{lock}} = 1\,\mathrm{Gyr}$ (left panel) and $t_{\mathrm{lock}} = 3\,\mathrm{Gyr}$ (right panel). In both cases, Hyperion successfully captures into the 4:3 mean-motion resonance with Titan after Titan begins migrating outward. Initially, Hyperion's eccentricity is suppressed to Titan's eccentricity, to which it is secularly coupled, by the dissipation resulting from chaotic tumbling. Once Hyperion reaches a sufficient semi-major axis, the resonant excitation from Titan becomes stronger than the tidal damping and Hyperion becomes more eccentric. By the end of the simulation, Hyperion has reached an eccentricity close its present value of 0.1. The amplitude of libration of the resonant angle is significant, even if somewhat smaller than what is observed.

Critically, this model of Hyperion's capture into resonance is not compatible with long-range Titan migration if damping in Hyperion is ignored. In such an undamped scenario, to prevent Hyperion from having too large of an eccentricity, Titan must only migrate 4% in semi-major axis (i.e., $t_{\mathrm{lock}} \approx 4.0\,\mathrm{Gyr}$) after the 4:3 capture. If, however, Titan migrated more than 11% from its initial location (i.e., $t_{\mathrm{lock}} \lesssim 3.2\,\mathrm{Gyr}$), Titan and Hyperion would have started wide of, and then encountered, the 3:2 resonance. The encounter is adiabatic (Batygin, 2015) and capture into the 3:2 is almost guaranteed, unless the eccentricity of Hyperion is very large.[2] Once in the wrong resonance, Hyperion will grow in eccentricity and eventually be ejected, never entering the 4:3 resonance. Thus, at face value, any model in which Titan and Hyperion cross first-order resonances

---

[2] Colombo et al., 1974 argue, using a backwards integration, that Hyperion would have avoided capture into the 2:1 and 3:2 resonances, but their reasoning is flawed. Because resonant encounters in the backwards integration are divergent, permanent capture into resonance is impossible regardless of migration speed (Henrard, 1982).

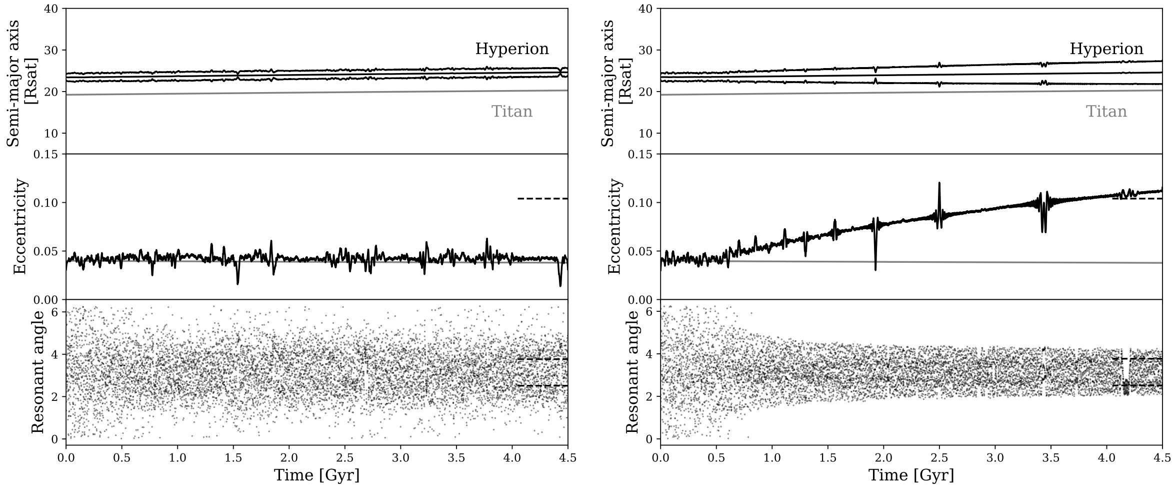

Figure 7.4: Capture of Hyperion into 4:3 resonance with Titan in the equilibrium tides model where $Q_{♄} = 1200$. On the left panel we have assumed $Q_{\mathrm{H}} = 100$, and on the right $Q_{\mathrm{H}} = \infty$, corresponding to no damping in Hyperion. Dashed lines in the bottom two rows show the measured values of Hyperion's (forced) eccentricity and libration angle range.

adiabatically requires that Hyperion and Titan must have started inside of the 3:2 resonance. However, incorporating tidal dissipation in Hyperion removes the fine-tuning restriction that the resonant lock-driven migration of Titan can only have begun recently.

Slower Titan Migration

Now, we consider the measurement of Jacobson (2022), who find $Q_{♄}(n_{\mathrm{Ti}}) = 1224 \pm 119$, or $\tau_{a,\mathrm{Ti}} \approx -100\,\mathrm{Gyr}$. Before proceeding, we remark that in the context of this measurement, it is not obvious what the source of dissipation with Saturn would be. Ćuk & El Moutamid, 2023 argue that $Q_{♄} \approx 1200$ is the frequency-independent dissipation within Saturn and that the Jacobson, 2022 measurement would imply that Titan is experiencing equilibrium tides outside a resonant lock. However, the migration of Tethys implies $Q_{♄} \approx 7000$ (Lainey et al., 2020) and it is not clear how one moon could experience tidal dissipation in Saturn weaker than equilibrium. In the absence of a clear guide, we take $Q_{♄} = 1200$ and assume $Q_{♄}$ is constant over time and forcing frequency. Integrating Eq. 7.19 from $t = 0$ to $t = 4.5\,\mathrm{Gyr}$, we find that with these assumptions, Titan's orbit has expanded by 6.1% over the age of the Solar System, so avoiding capture of Hyperion into the 3:2 resonance is not a concern.

We ran another suite of simulations with this model of slower Titan migration. Titan was initialized with an initial semi-major axis of $19.2R_{♄}$ and eccentricity of 0.04. Migration of Titan was computed with Eq. 7.19 and eccentricity damping was assumed, as in Section 7.3, to be $\tau_{e,\mathrm{Ti}} = \tau_{a,\mathrm{Ti}}$. The strength of dissipation in Saturn was set to $Q_{♄}/k_{2,♄} = 3000$, so that after 4.5 Gyr Titan would reach its current semi-major axis. Hyperion was initialized with several period ratios between the 4:3 and 3:2 resonance with Titan, and several eccentricities from 0 to 0.05.

Figure 7.4 shows two simulations of capture in this model of Titan migration, with $Q_{\mathrm{H}} = 100$ (left panel) and $Q_{\mathrm{H}} = \infty$ (right panel). The first value is generally expected for rocky bodies (Goldreich & Sari, 2009; Brasser, 2020) and puts Hyperion in the regime where tidal dissipation in Hyperion dominates over resonant excitation of eccentricity from Titan's slower migration. Hyperion remains secularly coupled to Titan and the resonant angle circulates. Conversely, $Q_{\mathrm{H}} = \infty$ corresponds to no dissipation in Hyperion and is equivalent to the tidal capture hypothesis of Colombo et al., 1974 and Ćuk et al., 2013. In this case, Hyperion reaches its present eccentricity and libration angle amplitude at the end of the simulation. Using the range of parameters in our simulation suite, we find that Hyperion only reaches its current eccentricity of 0.1 if $Q_{\mathrm{H}} \gtrsim 1000$.

Figures 7.3 and 7.4 demonstrate that slower Titan migration demands much weaker tidal dissipation in Hyperion. In the rapid migration scenario (Figure 7.3), eccentricity pumping from resonant excitation is roughly comparable to damping from tidal dissipation for $Q_{\mathrm{H}} \sim 100$, allowing the eccentricity to gradually grow to its present value. In contrast, resonant excitation from a slowly migrating Titan (Figure 7.4) is dwarfed by tidal dissipation unless Q_{H} is quite large.

This sort of weak dissipation in Hyperion is not physically implausible. Nimmo & Matsuyama, 2019 argue that in rocky rubble pile asteroids, energy losses occur only in a thin surface layer of regolith rather than the entire body. In the context of that model, they find that Q scales as R^2 and Q/k_2 as R. Hyperion is icy and much larger than the typical rubble pile asteroids they investigate, but extrapolating their model would predict that Hyperion has a very large Q/k_2.

7.4 Discussion and Conclusions

Despite its apparent simplicity, the outer saturnian system has confounded understanding for decades and arguably has become more challenging with new discoveries. At face value, the orbit of Hyperion implies that Titan migrated slowly, while the survival of Iapetus requires faster migration. Both cases rely on tidal dissipation in Saturn much stronger than conventionally expected. Taken together, these properties are a challenge to reconcile, especially while remaining consistent with constraints provided by the inner system.

We have shown that Hyperion's rotation is the key to resolving this discrepancy. Hyperion's spin rate depends steeply on its orbital eccentricity, a consequence of a chaotic sea generated from the overlap of spin-orbit resonances that grows with eccentricity. Tidal dissipation is much stronger at higher spins and is thus a steep function of e_{H} as well. Although the mean-motion resonant interaction between Titan and Hyperion grows the latter's orbital eccentricity as Titan migrates outward, the enhanced tidal dissipation resulting from rapid tumbling damps the eccentricity. The degree of dissipation within Hyperion can be probed by comparing the relative strengths of these two effects to match the observed $e_{\mathrm{H}} = 0.1$. The precise rate of Titan's migration is disputed in recent works. If it is rapid, Hyperion must have a tidal quality factor of $Q_{\mathrm{H}} \approx 40$, similar to what is typically expected for rocky bodies. Alternatively, if migration is slow, Hyperion must be only weakly dissipative ($Q_{\mathrm{H}} \gtrsim 1000$), which is reasonable if dissipation occurs solely in a surface layer, as suggested by Nimmo & Matsuyama, 2019.

The dissipation itself could in principle be detected directly through an excess thermal signature. Energy provided by the orbit acts to heat up Hyperion and sublimate its water ice. If Titan is migrating rapidly and $Q_{\mathrm{H}} = 40$ (e.g., right panel of Figure 7.3), the current energy dissipation rate is $dE/dt \sim 3\,\mathrm{MW}$. As a crude approximation, if this dissipation were constant over the lifetime of the Solar System, and assuming Hyperion is made entirely of water ice, approximately 3% of the mass of Hyperion would have sublimated due to the tidal dissipation. While non-negligible, this amount is insufficient to explain Hyperion's high ($> 40\%$) internal porosity (Thomas et al., 2007). However, it is possible that Hyperion experienced a transient phase of high eccentricity, perhaps due to a scattering event before the resonant capture with Titan. An excitation to $e_{\mathrm{H}} \approx 0.3$ followed by damping to a circular orbit could sublimate $\approx 40\%$ of Hyperion's mass in < 1 Gyr and account for its current porosity.

Significant sublimation could have other impacts. Seligman & Laughlin (2020) demonstrate that uniform sublimation across the surface of an ellipsoid acts to elongate it; they use this effect to explain the extreme body axis ratio of 'Oumuamua. If Hyperion underwent a similar process, its current shape could therefore be the consequence of a small irregularity in the shape of the primordial Hyperion that grew as material preferentially sublimated from certain regions.

These two complications highlight an important assumption we have made throughout this work. We have taken Hyperion's shape and material properties to be constant over the lifetime of the Solar System. However, sublimation, gravitational settling from tumbling, and impacts can vary the mass, composition, porosity, strength, and shape of Hyperion, all of which would affect the tidal dissipation rate. Incorporating all of these effects, while challenging, would provide a more complete picture of Hyperion's evolution.

Our detailed investigations of Hyperion's rotation showed that it is more complex than the original predictions derived from a one-dimensional model. Even so, generation of chaos via overlap of non-linear spin-orbit resonances remains qualitatively useful. Our results suggest that Hyperion has had a rich rotational history, alternating between tumbling and quasi-regular states that depend on its instantaneous eccentricity. The orbit and rotation of Hyperion are inextricably coupled: orbital eccentricity sets the typical spin rate, and in turn, the nonsynchronous spin damps the orbital eccentricity. Similar spin-to-orbit and orbit-to-spin coupling has been suggested for asteroid binaries (Efroimsky, 2015; Nimmo & Matsuyama, 2019; Quillen et al., 2022) and close-in satellites (Dobrovolskis et al., 1997; Quillen et al., 2017; Quillen et al., 2020). Hyperion, despite its small size and great distance from Saturn, is subject to the same complex feedback between spin and orbital evolution.

Although we have identified a compelling *process* to explain the current state of Hyperion, we have not determined the exact *scenario* that transpired. Of particular interest is Hyperion's initial orbit. If its original period ratio with Titan exceeded 1.5, capture into the 3:2 resonance is highly likely, unless another mechanism can break the resonance or avoid capture entirely. On the other hand, formation of Hyperion in such close proximity to the very massive Titan seems *a priori* unlikely. We encourage further work on this topic. Finally, our rotation model of Hyperion does not include the effects of tidal despinning. While it is clear that the current rotation state is not in the 1:1 or 3:2 island, it remains possible that it lies on a strange attractor with perpetual chaotic but quasi-regular motion (Melnikov, 2014). A self-consistent rotation model incorporating wobble damping and tidal dissipation that is coupled to the orbital evolution would thus be necessary to further constrain the history of Hyperion and more precisely measure its tidal parameters.

Chapter 8

CONCLUSION

The work presented in this thesis has made significant progress in understanding the physical processes involved in the assembly of compact multiplanet systems. Embedded in their architectures are the traces of their formation and evolution, revealing histories of gentle migration punctuated by violent dynamical instabilities. Nevertheless, this model is far from the complete story of extrasolar system formation. Many questions remain and present promising directions for future research.

For one, perhaps the most contentious object of study during the past five years in exoplanets has been the cause of the small planet radius valley. Most work has converged on one of two hypotheses: stellar FUV-driven photoevaporation or intrinsic core-powered mass loss (Bean et al., 2021; Weiss et al., 2022, and references therein). While atmospheric loss certainly operates in single-planet systems, it remains unclear whether the process is independent of the assembly of multiplanet systems, or deeply connected in some way. Giant impacts during dynamical instability (Chapter 2) could instead be responsible for atmospheric stripping, depending on the degree of thermal inflation (Izidoro et al., 2022; Biersteker & Schlichting, 2019). Alternatively, mass loss itself could act as the trigger of instability in marginally stable systems (Matsumoto & Ogihara, 2020; Wang & Lin, 2023, see theoretical explanation in Chapter 3), generating an intriguing feedback loop.

Another major question is the origin of mass uniformity in small planet systems. It is widely believed that some property of the protoplanetary disk sets a characteristic planet mass, but which property is most important? Ideas include the amount of local material available to accrete, growth limited by migration out of a feeding zone (Batygin & Morbidelli, 2023), or atmospheric mass loss. One additional channel we have begun to investigate is mass-dependent planet trapping within pressure bumps, which are likely widespread in protoplanetary disks. Low-mass planets are trapped in the bump by corotation torques (Paardekooper et al., 2011; Guilera et al., 2020), but sufficiently massive planets will saturate the torque and escape to the inner disk. Different mass scales would then be explained by the intensity of the pressure bump and the local turbulent viscosity.

Looking towards the future, major theoretical and observational challenges loom in the quest to answer these and other questions. Theoretical studies have increasingly tended towards population synthesis models that include as much physics as possible in an attempt to recreate the full diversity of the exoplanet census (e.g., Bitsch et al., 2019; Izidoro et al., 2021; Emsenhuber et al., 2021). Beyond the computational difficulties of such an approach, population synthesis has the potential to impede fundamental understanding of the formation process. Disentangling dozens of physical effects to isolate the relevant ones will be paramount. Nevertheless, the power of population synthesis lies in its ability to couple disparate effects that interact in complex and unexpected ways (e.g., Schlecker et al., 2021; Bitsch & Izidoro, 2023). This is especially important as observational results expand more and more beyond bulk population statistics to correlations in system properties.

Of course, just like the unanticipated discoveries of pulsar planets and Hot Jupiters triggered a revolution, nearly all major advances in astronomy come from new observations. Enormous progress has been made recently in measuring disk structures, leading to paradigm shifts in basic disk models (Andrews et al., 2018; Pascucci et al., 2023). Likewise, young massive planets have been directly imaged and are now being probed for clues to their formation location and mechanism (Bae et al., 2019; Wang et al., 2018). But what about accretion, the process that actually creates planets? Dust grains must grow by more than ten orders of magnitude to become planetary embryos, and numerous details along the way are poorly understood. Unlike the assembly of systems, which so far has been successfully probed by observing the architectures of existing systems, accretion is difficult to observe and measure. Close-in planets are deeply embedded in a dense disk inaccessible to most wavelengths, obscuring most of the action. Worse, if growth is dominated by rare giant impacts, the chance of observing one in real time is vanishingly small. To add to the complexity further, extrasolar circum*planetary* disks are even smaller than protoplanetary ones and probably only amenable to bulk characterization (Benisty et al., 2021).

Instead, indirect study of accretion is a promising path forward. JWST and future telescopes will characterize the chemical compositions of the atmospheres of smaller and smaller planets. Simultaneously, ALMA is uncovering the radial distributions of molecules in protoplanetary disks (Öberg et al., 2021). Synthesizing these results to determine when, where, and how planets formed is not trivial. To do so, we need a sufficient theoretical understanding of both planetary system assembly and accretion. As an example, growth of planets is most rapid beyond the water snowline and the resulting planets would remain rich in water even after significant inward migration. But, the small planets discovered by *Kepler* tentatively appear to be predominantly rocky, suggesting that they may have formed in the inner disk (Rogers & Owen, 2021). To ensure that the planets indeed lack ices, pebbles could be thermally devolatilized as they are accreted (Wang et al., 2023). This theory remains speculative pending observational tests, but the point is that observational results will only be interpretable using theoretical models.

It is clear from the study of the Solar System that planetary architecture alone does not tell the full story and fine details are critically important. The structures of the asteroid and Kuiper belts imply that the giant planets migrated, while meteoritic isotope evidence demonstrates both isolation and mixing of multiple primordial reservoirs of material (Malhotra, 1995; Deienno et al., 2016;

Warren, 2011; Kruijer et al., 2017). Furthermore, measurements of the interior structures of planets and satellites reveals a complicated and diverse accretion history (Canup & Ward, 2002; Rubie et al., 2015). Just as these measurements have upended existing theories of the Solar System's formation, similar measurements made outside of the Solar System, once possible, will undoubtedly revolutionize our current theories of exoplanet formation. We are far from understanding all of the nuances and complexities of the Solar System, and we live here. How far must we be from truly comprehending extrasolar worlds!

BIBLIOGRAPHY

Adams, F. C., Laughlin, G. & Bloch, A. M. (Aug. 2008). “Turbulence Implies That Mean Motion Resonances Are Rare.” In: *The Astrophysical Journal* 683, pp. 1117–1128. DOI: `10.1086/589986`.

Agol, E., Dorn, C., Grimm, S. L., et al. (Feb. 2021). “Refining the Transit-timing and Photometric Analysis of TRAPPIST-1: Masses, Radii, Densities, Dynamics, and Ephemerides.” In: *The Planetary Science Journal* 2, p. 1. ISSN: 2632-3338. DOI: `10.3847/PSJ/abd022`.

Agol, E., Steffen, J., Sari, R., et al. (May 2005). “On Detecting Terrestrial Planets with Timing of Giant Planet Transits.” In: *Monthly Notices of the Royal Astronomical Society* 359, pp. 567–579. ISSN: 0035-8711. DOI: `10.1111/j.1365-2966.2005.08922.x`.

Agrusa, H. F., Gkolias, I., Tsiganis, K., et al. (Dec. 2021). “The Excited Spin State of Dimorphos Resulting from the DART Impact.” In: *Icarus* 370, p. 114624. ISSN: 0019-1035. DOI: `10.1016/j.icarus.2021.114624`.

Andrews, S. M. (Aug. 2020). “Observations of Protoplanetary Disk Structures.” In: *Annual Review of Astronomy and Astrophysics* 58, pp. 483–528. ISSN: 0066-4146. DOI: `10.1146/annurev-astro-031220-010302`.

Andrews, S. M., Huang, J., Pérez, L. M., et al. (Dec. 2018). “The Disk Substructures at High Angular Resolution Project (DSHARP). I. Motivation, Sample, Calibration, and Overview.” In: *The Astrophysical Journal* 869, p. L41. ISSN: 0004-637X. DOI: `10.3847/2041-8213/aaf741`.

Armitage, P. J. (Jan. 2020). *Astrophysics of Planet Formation, Second Edition*. Cambridge University.

Arribas, M., Elipe, A. & Palacios, M. (Nov. 2006). “Quaternions and the Rotation of a Rigid Body.” In: *Celestial Mechanics and Dynamical Astronomy* 96.3, pp. 239–251. ISSN: 1572-9478. DOI: `10.1007/s10569-006-9037-6`.

Ataiee, S. & Kley, W. (Mar. 2020). “The Role of Disc Torques in Forming Resonant Planetary Systems.” In: *Astronomy and Astrophysics* 635, A204. ISSN: 0004-6361. DOI: `10.1051/0004-6361/201936390`.

Bae, J., Zhu, Z., Baruteau, C., et al. (Oct. 2019). “An Ideal Testbed for Planet-Disk Interaction: Two Giant Protoplanets in Resonance Shaping the PDS 70 Protoplanetary Disk.” In: *The Astrophysical Journal* 884, p. L41. ISSN: 0004-637X. DOI: `10.3847/2041-8213/ab46b0`.

Batalha, N. M., Rowe, J. F., Bryson, S. T., et al. (Feb. 2013). “Planetary Candidates Observed by Kepler. III. Analysis of the First 16 Months of Data.” In: *The Astrophysical Journal Supplement Series* 204, p. 24. DOI: `10.1088/0067-0049/204/2/24`.

Batygin, K. (Aug. 2015). “Capture of Planets into Mean-Motion Resonances and the Origins of Extrasolar Orbital Architectures.” In: *Monthly Notices of the Royal Astronomical Society* 451, pp. 2589–2609. ISSN: 0035-8711. DOI: `10.1093/mnras/stv1063`.

Batygin, K. & Adams, F. C. (Mar. 2017). “An Analytic Criterion for Turbulent Disruption of Planetary Resonances.” In: *The Astronomical Journal* 153, p. 120. ISSN: 0004-6256. DOI: `10.3847/1538-3881/153/3/120`.

Batygin, K., Adams, F. C. & Becker, J. (July 2023). “The Origin of Universality in the Inner Edges of Planetary Systems.” In: *The Astrophysical Journal* 951, p. L19. ISSN: 0004-637X. DOI: `10.3847/2041-8213/acdb5d`.

Batygin, K. & Brown, M. E. (June 2010). “Early Dynamical Evolution of the Solar System: Pinning Down the Initial Conditions of the Nice Model.” In: *The Astrophysical Journal* 716, pp. 1323–1331. ISSN: 0004-637X. DOI: `10.1088/0004-637X/716/2/1323`.

Batygin, K., Deck, K. M. & Holman, M. J. (May 2015). “Dynamical Evolution of Multi-resonant Systems: The Case of GJ876.” In: *The Astronomical Journal* 149, p. 167. ISSN: 0004-6256. DOI: `10.1088/0004-6256/149/5/167`.

Batygin, K. & Laughlin, G. (Apr. 2015). “Jupiter’s Decisive Role in the Inner Solar System’s Early Evolution.” In: *Proceedings of the National Academy of Science* 112, pp. 4214–4217. ISSN: 0027-8424. DOI: `10.1073/pnas.1423252112`.

Batygin, K. & Laughlin, G. (Aug. 2008). “On the Dynamical Stability of the Solar System.” In: *The Astrophysical Journal* 683, pp. 1207–1216. ISSN: 0004-637X. DOI: `10.1086/589232`.

Batygin, K. & Morbidelli, A. (Jan. 2013). “Dissipative Divergence of Resonant Orbits.” In: *The Astronomical Journal* 145, p. 1. DOI: `10.1088/0004-6256/145/1/1`.

Batygin, K. & Morbidelli, A. (Jan. 2023). “Formation of Rocky Super-Earths from a Narrow Ring of Planetesimals.” In: *Nature Astronomy*. ISSN: 2397-3366. DOI: `10.1038/s41550-022-01850-5`.

Bean, J. L., Raymond, S. N. & Owen, J. E. (Jan. 2021). “The Nature and Origins of Sub-Neptune Size Planets.” In: *Journal of Geophysical Research (Planets)* 126, e06639. ISSN: 0148-0227. DOI: `10.1029/2020JE006639`.

Beauge, C. (Oct. 1994). “Asymmetric Librations in Exterior Resonances.” In: *Celestial Mechanics and Dynamical Astronomy* 60, pp. 225–248. ISSN: 0923-2958. DOI: `10.1007/BF00693323`.

Benisty, M., Bae, J., Facchini, S., et al. (July 2021). “A Circumplanetary Disk around PDS70c.” In: *The Astrophysical Journal* 916, p. L2. ISSN: 0004-637X. DOI: `10.3847/2041-8213/ac0f83`.

Berger, T. A., Howard, A. W. & Boesgaard, A. M. (Mar. 2018). “Identifying Young Kepler Planet Host Stars from Keck-HIRES Spectra of Lithium.” In: *The Astrophysical Journal* 855, p. 115. DOI: `10.3847/1538-4357/aab154`.

Betancourt, M. (Jan. 2017). *A Conceptual Introduction to Hamiltonian Monte Carlo*. DOI: `10.48550/arXiv.1701.02434`.

Biersteker, J. B. & Schlichting, H. E. (May 2019). “Atmospheric Mass-Loss Due to Giant Impacts: The Importance of the Thermal Component for Hydrogen-Helium Envelopes.” In: *Monthly Notices of the Royal Astronomical Society* 485, pp. 4454–4463. ISSN: 0035-8711. DOI: `10.1093/mnras/stz738`.

Bitsch, B. & Izidoro, A. (June 2023). “Giants Are Bullies: How Their Growth Influences Systems of Inner Sub-Neptunes and Super-Earths.” In: *Astronomy and Astrophysics* 674, A178. ISSN: 0004-6361. DOI: `10.1051/0004-6361/202245040`.

Bitsch, B., Izidoro, A., Johansen, A., et al. (Mar. 2019). “Formation of Planetary Systems by Pebble Accretion and Migration: Growth of Gas Giants.” In: *Astronomy and Astrophysics* 623, A88. ISSN: 0004-6361. DOI: `10.1051/0004-6361/201834489`.

Black, G. J., Nicholson, P. D. & Thomas, P. C. (Sept. 1995). “Hyperion: Rotational Dynamics.” In: *Icarus* 117, pp. 149–161. ISSN: 0019-1035. DOI: `10.1006/icar.1995.1148`.

Borderies, N. & Goldreich, P. (Feb. 1984). “A Simple Derivation of Capture Probabilities for the J + 1 : J and J + 2 : J Orbit-Orbit Resonance Problems.” In: *Celestial Mechanics* 32, pp. 127–136. DOI: `10.1007/BF01231120`.

Borucki, W. J., Koch, D. G., Basri, G., et al. (July 2011). “Characteristics of Planetary Candidates Observed by Kepler. II. Analysis of the First Four Months of Data.” In: *The Astrophysical Journal* 736, p. 19. ISSN: 0004-637X. DOI: `10.1088/0004-637X/736/1/19`.

Bottke, W. F., Vokrouhlický, D., Marshall, R., et al. (Sept. 2023). “The Collisional Evolution of the Primordial Kuiper Belt, Its Destabilized Population, and the Trojan Asteroids.” In: *The Planetary Science Journal* 4, p. 168. ISSN: 2632-3338. DOI: `10.3847/PSJ/ace7cd`.

Brasser, R. (Sept. 2020). “Efficient Tidal Dissipation in Deimos.” In: *Icarus* 347, p. 113791. ISSN: 0019-1035. DOI: `10.1016/j.icarus.2020.113791`.

Brozović, M., Showalter, M. R., Jacobson, R. A., et al. (Mar. 2020). “Orbits and Resonances of the Regular Moons of Neptune.” In: *Icarus* 338, p. 113462. ISSN: 0019-1035. DOI: `10.1016/j.icarus.2019.113462`.

Budde, G., Burkhardt, C., Brennecka, G. A., et al. (Nov. 2016). “Molybdenum Isotopic Evidence for the Origin of Chondrules and a Distinct Genetic Heritage of Carbonaceous and Non-Carbonaceous Meteorites.” In: *Earth and Planetary Science Letters* 454, pp. 293–303. ISSN: 0012-821X. DOI: `10.1016/j.epsl.2016.09.020`.

Burns, J. A. & Safronov, V. S. (Jan. 1973). “Asteroid Nutation Angles.” In: *Monthly Notices of the Royal Astronomical Society* 165, p. 403. ISSN: 0035-8711. DOI: `10.1093/mnras/165.4.403`.

Cameron, A. G. W. (1988). “Origin of the Solar System.” In: *Annual Review of Astronomy and Astrophysics* 26, pp. 441–472. DOI: `10.1146/annurev.aa.26.090188.002301`.

Canup, R. M. & Ward, W. R. (Dec. 2002). “Formation of the Galilean Satellites: Conditions of Accretion.” In: *The Astronomical Journal* 124, pp. 3404–3423. ISSN: 0004-6256. DOI: `10.1086/344684`.

Carter, J. A., Agol, E., Chaplin, W. J., et al. (Aug. 2012). “Kepler-36: A Pair of Planets with Neighboring Orbits and Dissimilar Densities.” In: *Science* 337, p. 556. ISSN: 0036-8075. DOI: `10.1126/science.1223269`.

Cerioni, M., Beaugé, C. & Gallardo, T. (June 2022). “Is the Orbital Distribution of Multiplanet Systems Influenced by Pure Three-Planet Resonances?” In: *Monthly Notices of the Royal Astronomical Society* 513, pp. 541–550. ISSN: 0035-8711. DOI: `10.1093/mnras/stac876`.

Chambers, J. E., Wetherill, G. W. & Boss, A. P. (Feb. 1996). "The Stability of Multi-Planet Systems." In: *Icarus* 119, pp. 261–268. ISSN: 0019-1035. DOI: `10.1006/icar.1996.0019`.

Charalambous, C., Martí, J. G., Beaugé, C., et al. (June 2018). "Resonance Capture and Dynamics of Three-Planet Systems." In: *Monthly Notices of the Royal Astronomical Society* 477, pp. 1414–1425. ISSN: 0035-8711. DOI: `10.1093/mnras/sty676`.

Charalambous, C., Teyssandier, J. & Libert, A.-S. (Aug. 2022). "Proximity of Exoplanets to First-Order Mean-Motion Resonances." In: *Monthly Notices of the Royal Astronomical Society* 514, pp. 3844–3856. ISSN: 0035-8711. DOI: `10.1093/mnras/stac1554`.

Chatterjee, S. & Ford, E. B. (Apr. 2015). "Planetesimal Interactions Can Explain the Mysterious Period Ratios of Small Near-Resonant Planets." In: *The Astrophysical Journal* 803, p. 33. ISSN: 0004-637X. DOI: `10.1088/0004-637X/803/1/33`.

Chen, J. & Kipping, D. (Jan. 2017). "Probabilistic Forecasting of the Masses and Radii of Other Worlds." In: *The Astrophysical Journal* 834, p. 17. ISSN: 0004-637X. DOI: `10.3847/1538-4357/834/1/17`.

Chirikov, B. V. (May 1979). "A Universal Instability of Many-Dimensional Oscillator Systems." In: *Physics Reports* 52, pp. 263–379. ISSN: 0370-1573. DOI: `10.1016/0370-1573(79)90023-1`.

Choksi, N. & Chiang, E. (July 2020). "Sub-Neptune Formation: The View from Resonant Planets." In: *Monthly Notices of the Royal Astronomical Society* 495, pp. 4192–4209. ISSN: 0035-8711. DOI: `10.1093/mnras/staa1421`.

Christiansen, J. L., Crossfield, I. J. M., Barentsen, G., et al. (Feb. 2018). "The K2-138 System: A Near-resonant Chain of Five Sub-Neptune Planets Discovered by Citizen Scientists." In: *The Astronomical Journal* 155, p. 57. ISSN: 0004-6256. DOI: `10.3847/1538-3881/aa9be0`.

Ciardi, D. R., Fabrycky, D. C., Ford, E. B., et al. (Jan. 2013). "On the Relative Sizes of Planets within Kepler Multiple-candidate Systems." In: *The Astrophysical Journal* 763, p. 41. ISSN: 0004-637X. DOI: `10.1088/0004-637X/763/1/41`.

Colombo, G., Franklin, F. A. & Shapiro, I. I. (Jan. 1974). "On the Formation of the Orbit-Orbit Resonance of Titan and Hyperion." In: *The Astronomical Journal* 79, p. 61. ISSN: 0004-6256. DOI: `10.1086/111533`.

Cossou, C., Raymond, S. N., Hersant, F., et al. (Sept. 2014). "Hot Super-Earths and Giant Planet Cores from Different Migration Histories." In: *Astronomy and Astrophysics* 569, A56. ISSN: 0004-6361. DOI: `10.1051/0004-6361/201424157`.

Cresswell, P. & Nelson, R. P. (May 2006). "On the Evolution of Multiple Protoplanets Embedded in a Protostellar Disc." In: *Astronomy and Astrophysics* 450, pp. 833–853. ISSN: 0004-6361. DOI: `10.1051/0004-6361:20054551`.

Cresswell, P. & Nelson, R. P. (May 2008). "Three-Dimensional Simulations of Multiple Protoplanets Embedded in a Protostellar Disc." In: *Astronomy and Astrophysics* 482, pp. 677–690. ISSN: 0004-6361. DOI: `10.1051/0004-6361:20079178`.

Crida, A., Papaloizou, J. C. B., Rein, H., et al. (Oct. 2010). “Migration of a Moonlet in a Ring of Solid Particles: Theory and Application to Saturn’s Propellers.” In: *The Astronomical Journal* 140, pp. 944–953. ISSN: 0004-6256. DOI: `10.1088/0004-6256/140/4/944`.

Crossfield, I. J. M., Ciardi, D. R., Petigura, E. A., et al. (Sept. 2016). “197 Candidates and 104 Validated Planets in K2’s First Five Fields.” In: *The Astrophysical Journal Supplement Series* 226, p. 7. ISSN: 0067-0049. DOI: `10.3847/0067-0049/226/1/7`.

Cui, Z., Papaloizou, J. C. B. & Szuszkiewicz, E. (Nov. 2021). “On the Importance of Wave-Planet Interactions for the Migration of Two Super-Earths Embedded in a Protoplanetary Disk.” In: *The Astrophysical Journal* 921, p. 142. ISSN: 0004-637X. DOI: `10.3847/1538-4357/ac17eb`.

Ćuk, M., Dones, L. & Nesvorný, D. (Nov. 2013). *Titan-Hyperion Resonance and the Tidal Q of Saturn.*

Ćuk, M., Dones, L. & Nesvorný, D. (Apr. 2016a). “Dynamical Evidence for a Late Formation of Saturn’s Moons.” In: *The Astrophysical Journal* 820, p. 97. ISSN: 0004-637X. DOI: `10.3847/0004-637X/820/2/97`.

Ćuk, M. & El Moutamid, M. (July 2023). “A Past Episode of Rapid Tidal Evolution of Enceladus?” In: *The Planetary Science Journal* 4, p. 119. ISSN: 2632-3338. DOI: `10.3847/PSJ/acde80`.

Ćuk, M., Hamilton, D. P., Lock, S. J., et al. (Nov. 2016b). “Tidal Evolution of the Moon from a High-Obliquity, High-Angular-Momentum Earth.” In: *Nature* 539, pp. 402–406. ISSN: 0028-0836. DOI: `10.1038/nature19846`.

Dai, F., Masuda, K., Beard, C., et al. (Feb. 2023). “TOI-1136 Is a Young, Coplanar, Aligned Planetary System in a Pristine Resonant Chain.” In: *The Astronomical Journal* 165, p. 33. ISSN: 0004-6256. DOI: `10.3847/1538-3881/aca327`.

Dawson, R. I., Lee, E. J. & Chiang, E. (May 2016). “Correlations between Compositions and Orbits Established by the Giant Impact Era of Planet Formation.” In: *The Astrophysical Journal* 822, p. 54. ISSN: 0004-637X. DOI: `10.3847/0004-637X/822/1/54`.

Deck, K. M. & Batygin, K. (Sept. 2015). “Migration of Two Massive Planets into (and out of) First Order Mean Motion Resonances.” In: *The Astrophysical Journal* 810, p. 119. ISSN: 0004-637X. DOI: `10.1088/0004-637X/810/2/119`.

Deck, K. M., Holman, M. J., Agol, E., et al. (Aug. 2012). “Rapid Dynamical Chaos in an Exoplanetary System.” In: *The Astrophysical Journal* 755, p. L21. ISSN: 0004-637X. DOI: `10.1088/2041-8205/755/1/L21`.

Deck, K. M., Payne, M. & Holman, M. J. (Sept. 2013). “First-Order Resonance Overlap and the Stability of Close Two-planet Systems.” In: *The Astrophysical Journal* 774, p. 129. ISSN: 0004-637X. DOI: `10.1088/0004-637X/774/2/129`.

Deienno, R., Gomes, R. S., Walsh, K. J., et al. (July 2016). “Is the Grand Tack Model Compatible with the Orbital Distribution of Main Belt Asteroids?” In: *Icarus* 272, pp. 114–124. ISSN: 0019-1035. DOI: `10.1016/j.icarus.2016.02.043`.

Delisle, J.-B. (Sept. 2017). “Analytical Model of Multi-Planetary Resonant Chains and Constraints on Migration Scenarios.” In: *Astronomy and Astrophysics* 605, A96. ISSN: 0004-6361. DOI: `10.1051/0004-6361/201730857`.

Delisle, J.-B. & Laskar, J. (Oct. 2014). “Tidal Dissipation and the Formation of Kepler Near-Resonant Planets.” In: *Astronomy and Astrophysics* 570, p. L7. ISSN: 0004-6361. DOI: `10.1051/0004-6361/201424227`.

Delisle, J.-B., Laskar, J., Correia, A. C. M., et al. (Oct. 2012). “Dissipation in Planar Resonant Planetary Systems.” In: *Astronomy and Astrophysics* 546, A71. ISSN: 0004-6361. DOI: `10.1051/0004-6361/201220001`.

Dobrovolskis, A. R., Peale, S. J. & Harris, A. W. (Jan. 1997). *Dynamics of the Pluto-Charon Binary*, p. 159.

Dobrovolskis, A. R. (Nov. 1995). “Chaotic Rotation of Nereid?” In: *Icarus* 118, pp. 181–198. ISSN: 0019-1035. DOI: `10.1006/icar.1995.1184`.

Drążkowska, J., Alibert, Y. & Moore, B. (Oct. 2016). “Close-in Planetesimal Formation by Pile-up of Drifting Pebbles.” In: *Astronomy and Astrophysics* 594, A105. ISSN: 0004-6361. DOI: `10.1051/0004-6361/201628983`.

Efroimsky, M. (Oct. 2015). “Tidal Evolution of Asteroidal Binaries. Ruled by Viscosity. Ignorant of Rigidity.” In: *The Astronomical Journal* 150, p. 98. ISSN: 0004-6256. DOI: `10.1088/0004-6256/150/4/98`.

Efroimsky, M. & Lainey, V. (Dec. 2007). “Physics of Bodily Tides in Terrestrial Planets and the Appropriate Scales of Dynamical Evolution.” In: *Journal of Geophysical Research (Planets)* 112, E12003. DOI: `10.1029/2007JE002908`.

Emsenhuber, A., Mordasini, C., Burn, R., et al. (Dec. 2021). “The New Generation Planetary Population Synthesis (NGPPS). I. Bern Global Model of Planet Formation and Evolution, Model Tests, and Emerging Planetary Systems.” In: *Astronomy and Astrophysics* 656, A69. ISSN: 0004-6361. DOI: `10.1051/0004-6361/202038553`.

Esteves, L., Izidoro, A., Bitsch, B., et al. (Jan. 2022). “The ’breaking the Chains’ Migration Model for Super-Earth Formation: The Effect of Collisional Fragmentation.” In: *Monthly Notices of the Royal Astronomical Society* 509, pp. 2856–2868. ISSN: 0035-8711. DOI: `10.1093/mnras/stab3203`.

Esteves, L., Izidoro, A., Raymond, S. N., et al. (July 2020). “The Origins of Nearly Coplanar, Non-Resonant Systems of Close-in Super-Earths.” In: *Monthly Notices of the Royal Astronomical Society* 497, pp. 2493–2500. DOI: `10.1093/mnras/staa2112`.

Fabrycky, D. C., Ford, E. B., Steffen, J. H., et al. (May 2012). “Transit Timing Observations from Kepler. IV. Confirmation of Four Multiple-planet Systems by Simple Physical Models.” In: *The Astrophysical Journal* 750, p. 114. ISSN: 0004-637X. DOI: `10.1088/0004-637X/750/2/114`.

Fabrycky, D. C., Lissauer, J. J., Ragozzine, D., et al. (Aug. 2014). “Architecture of Kepler’s Multi-transiting Systems. II. New Investigations with Twice as Many Candidates.” In: *The Astrophysical Journal* 790, p. 146. ISSN: 0004-637X. DOI: `10.1088/0004-637X/790/2/146`.

Flock, M., Fromang, S., Turner, N. J., et al. (Feb. 2017). “3D Radiation Nonideal Magnetohydrodynamical Simulations of the Inner Rim in Protoplanetary Disks.” In: *The Astrophysical Journal* 835, p. 230. ISSN: 0004-637X. DOI: `10.3847/1538-4357/835/2/230`.

Ford, E. B., Quinn, S. N. & Veras, D. (May 2008). “Characterizing the Orbital Eccentricities of Transiting Extrasolar Planets with Photometric Observations.” In: *The Astrophysical Journal* 678, pp. 1407–1418. ISSN: 0004-637X. DOI: `10.1086/587046`.

Fressin, F., Torres, G., Charbonneau, D., et al. (Apr. 2013). “The False Positive Rate of Kepler and the Occurrence of Planets.” In: *The Astrophysical Journal* 766, p. 81. ISSN: 0004-637X. DOI: `10.1088/0004-637X/766/2/81`.

Fuller, J., Luan, J. & Quataert, E. (June 2016). “Resonance Locking as the Source of Rapid Tidal Migration in the Jupiter and Saturn Moon Systems.” In: *Monthly Notices of the Royal Astronomical Society* 458, pp. 3867–3879. ISSN: 0035-8711. DOI: `10.1093/mnras/stw609`.

Fulton, B. J., Petigura, E. A., Howard, A. W., et al. (Sept. 2017). “The California-Kepler Survey. III. A Gap in the Radius Distribution of Small Planets.” In: *The Astronomical Journal* 154, p. 109. ISSN: 0004-6256. DOI: `10.3847/1538-3881/aa80eb`.

Fulton, B. J., Rosenthal, L. J., Hirsch, L. A., et al. (July 2021). “California Legacy Survey. II. Occurrence of Giant Planets beyond the Ice Line.” In: *The Astrophysical Journal Supplement Series* 255, p. 14. ISSN: 0067-0049. DOI: `10.3847/1538-4365/abfcc1`.

Gallardo, T., Coito, L. & Badano, L. (Aug. 2016). “Planetary and Satellite Three Body Mean Motion Resonances.” In: *Icarus* 274, pp. 83–98. ISSN: 0019-1035. DOI: `10.1016/j.icarus.2016.03.018`.

Ghosh, T. & Chatterjee, S. (Jan. 2023). “Effects of Planetesimal Scattering: Explaining the Observed Offsets from Period Ratios 3:2 and 2:1.” In: *The Astrophysical Journal* 943, p. 8. ISSN: 0004-637X. DOI: `10.3847/1538-4357/aca58e`.

Gilbert, G. J. & Fabrycky, D. C. (June 2020). “An Information Theoretic Framework for Classifying Exoplanetary System Architectures.” In: *The Astronomical Journal* 159, p. 281. ISSN: 0004-6256. DOI: `10.3847/1538-3881/ab8e3c`.

Gillon, M., Triaud, A. H. M. J., Demory, B.-O., et al. (Feb. 2017). “Seven Temperate Terrestrial Planets around the Nearby Ultracool Dwarf Star TRAPPIST-1.” In: *Nature* 542, pp. 456–460. ISSN: 0028-0836. DOI: `10.1038/nature21360`.

Gladman, B. (Nov. 1993). “Dynamics of Systems of Two Close Planets.” In: *Icarus* 106, pp. 247–263. ISSN: 0019-1035. DOI: `10.1006/icar.1993.1169`.

Goldberg, M. & Batygin, K. (July 2021). “A Tidal Origin for a Three-body Resonance in Kepler-221.” In: *The Astronomical Journal* 162, p. 16. ISSN: 0004-6256. DOI: `10.3847/1538-3881/abfb78`.

Goldberg, M. & Batygin, K. (May 2022). “Architectures of Compact Super-Earth Systems Shaped by Instabilities.” In: *The Astronomical Journal* 163, p. 201. ISSN: 0004-6256. DOI: `10.3847/1538-3881/ac5961`.

Goldreich, P. & Tremaine, S. (Nov. 1979). “The Excitation of Density Waves at the Lindblad and Corotation Resonances by an External Potential.” In: *The Astrophysical Journal* 233, pp. 857–871. ISSN: 0004-637X. DOI: `10.1086/157448`.

Goldreich, P. & Tremaine, S. (Oct. 1980). “Disk-Satellite Interactions.” In: *The Astrophysical Journal* 241, pp. 425–441. ISSN: 0004-637X. DOI: `10.1086/158356`.

Goldreich, P. & Peale, S. (Aug. 1966). “Spin-Orbit Coupling in the Solar System.” In: *The Astronomical Journal* 71, p. 425. ISSN: 0004-6256. DOI: `10.1086/109947`.

Goldreich, P. & Sari, R. (Jan. 2009). “Tidal Evolution of Rubble Piles.” In: *The Astrophysical Journal* 691, pp. 54–60. ISSN: 0004-637X. DOI: `10.1088/0004-637X/691/1/54`.

Goldreich, P. & Schlichting, H. E. (Feb. 2014). “Overstable Librations Can Account for the Paucity of Mean Motion Resonances among Exoplanet Pairs.” In: *The Astronomical Journal* 147, p. 32. ISSN: 0004-6256. DOI: `10.1088/0004-6256/147/2/32`.

Goldreich, P. & Soter, S. (Jan. 1966). “Q in the Solar System.” In: *Icarus* 5, pp. 375–389. ISSN: 0019-1035. DOI: `10.1016/0019-1035(66)90051-0`.

Goździewski, K., Migaszewski, C., Panichi, F., et al. (Jan. 2016). “The Laplace Resonance in the Kepler-60 Planetary System.” In: *Monthly Notices of the Royal Astronomical Society* 455, pp. L104–L108. ISSN: 0035-8711. DOI: `10.1093/mnrasl/slv156`.

Guilera, O. M., Sándor, Z., Ronco, M. P., et al. (Oct. 2020). “Giant Planet Formation at the Pressure Maxima of Protoplanetary Disks. II. A Hybrid Accretion Scenario.” In: *Astronomy and Astrophysics* 642, A140. ISSN: 0004-6361. DOI: `10.1051/0004-6361/202038458`.

Hadden, S. (Dec. 2019). “An Integrable Model for the Dynamics of Planetary Mean-motion Resonances.” In: *The Astronomical Journal* 158, p. 238. ISSN: 0004-6256. DOI: `10.3847/1538-3881/ab5287`.

Hadden, S. & Lithwick, Y. (May 2014). “Densities and Eccentricities of 139 Kepler Planets from Transit Time Variations.” In: *The Astrophysical Journal* 787, p. 80. DOI: `10.1088/0004-637X/787/1/80`.

Hadden, S. & Lithwick, Y. (Sept. 2016). “Numerical and Analytical Modeling of Transit Timing Variations.” In: *The Astrophysical Journal* 828, p. 44. ISSN: 0004-637X. DOI: `10.3847/0004-637X/828/1/44`.

Hadden, S. & Lithwick, Y. (July 2017). “Kepler Planet Masses and Eccentricities from TTV Analysis.” In: *The Astronomical Journal* 154, p. 5. ISSN: 0004-6256. DOI: `10.3847/1538-3881/aa71ef`.

Hadden, S. & Lithwick, Y. (Sept. 2018). “A Criterion for the Onset of Chaos in Systems of Two Eccentric Planets.” In: *The Astronomical Journal* 156, p. 95. ISSN: 0004-6256. DOI: `10.3847/1538-3881/aad32c`.

Hadden, S. & Payne, M. J. (Sept. 2020). “Modeling Radial Velocity Data of Resonant Planets to Infer Migration Histories.” In: *The Astronomical Journal* 160, p. 106. ISSN: 0004-6256. DOI: `10.3847/1538-3881/aba751`.

Hands, T. O., Alexander, R. D. & Dehnen, W. (Nov. 2014). “Understanding the Assembly of Kepler’s Compact Planetary Systems.” In: *Monthly Notices of the Royal Astronomical Society* 445, pp. 749–760. ISSN: 0035-8711. DOI: `10.1093/mnras/stu1751`.

Hansen, B. M. S. & Murray, N. (June 2012). “Migration Then Assembly: Formation of Neptune-mass Planets inside 1 AU.” In: *The Astrophysical Journal* 751, p. 158. ISSN: 0004-637X. DOI: `10.1088/0004-637X/751/2/158`.

Harbison, R. A., Thomas, P. C. & Nicholson, P. C. (May 2011). “Rotational Modeling of Hyperion.” In: *Celestial Mechanics and Dynamical Astronomy* 110, pp. 1–16. ISSN: 0923-2958. DOI: `10.1007/s10569-011-9337-3`.

Hayashi, C. (Jan. 1981). “Structure of the Solar Nebula, Growth and Decay of Magnetic Fields and Effects of Magnetic and Turbulent Viscosities on the Nebula.” In: *Progress of Theoretical Physics Supplement* 70, pp. 35–53. ISSN: 0375-9687. DOI: `10.1143/PTPS.70.35`.

Hayes, W. & Tremaine, S. (Oct. 1998). “Fitting Selected Random Planetary Systems to Titius-Bode Laws.” In: *Icarus* 135, pp. 549–557. ISSN: 0019-1035. DOI: `10.1006/icar.1998.5999`.

He, M. Y., Ford, E. B., Ragozzine, D., et al. (Dec. 2020). “Architectures of Exoplanetary Systems. III. Eccentricity and Mutual Inclination Distributions of AMD-stable Planetary Systems.” In: *The Astronomical Journal* 160, p. 276. ISSN: 0004-6256. DOI: `10.3847/1538-3881/abba18`.

Henrard, J. (May 1982). “Capture into Resonance - an Extension of the Use of Adiabatic Invariants.” In: *Celestial Mechanics* 27, pp. 3–22. ISSN: 0008-8714. DOI: `10.1007/BF01228946`.

Henrard, J. & Lemaitre, A. (June 1983). “A Second Fundamental Model for Resonance.” In: *Celestial Mechanics* 30, pp. 197–218. ISSN: 0008-8714. DOI: `10.1007/BF01234306`.

Howard, A. W., Marcy, G. W., Bryson, S. T., et al. (Aug. 2012). “Planet Occurrence within 0.25 AU of Solar-type Stars from Kepler.” In: *The Astrophysical Journal Supplement Series* 201, p. 15. ISSN: 0067-0049. DOI: `10.1088/0067-0049/201/2/15`.

Howard, A. W., Marcy, G. W., Johnson, J. A., et al. (Oct. 2010). “The Occurrence and Mass Distribution of Close-in Super-Earths, Neptunes, and Jupiters.” In: *Science* 330, p. 653. ISSN: 0036-8075. DOI: `10.1126/science.1194854`.

Hühn, L.-A., Pichierri, G., Bitsch, B., et al. (Dec. 2021). “Kepler-223 Resonance Holds Information about Turbulence during the Gas-Disk Phase.” In: *Astronomy and Astrophysics* 656, A115. ISSN: 0004-6361. DOI: `10.1051/0004-6361/202142176`.

Ida, S. & Lin, D. N. C. (Jan. 2008). “Toward a Deterministic Model of Planetary Formation. IV. Effects of Type I Migration.” In: *The Astrophysical Journal* 673, pp. 487–501. ISSN: 0004-637X. DOI: `10.1086/523754`.

Ida, S. & Lin, D. N. C. (Aug. 2010). “Toward a Deterministic Model of Planetary Formation. VI. Dynamical Interaction and Coagulation of Multiple Rocky Embryos and Super-Earth Systems around Solar-type Stars.” In: *The Astrophysical Journal* 719, pp. 810–830. ISSN: 0004-637X. DOI: `10.1088/0004-637X/719/1/810`.

Isaacson, H. & Fischer, D. (Dec. 2010). “Chromospheric Activity and Jitter Measurements for 2630 Stars on the California Planet Search.” In: *The Astrophysical Journal, Volume 725, Issue 1, pp. 875-885 (2010).* 725, pp. 875–885. ISSN: 0004-637X. DOI: `10.1088/0004-637X/725/1/875`.

Izidoro, A., Ogihara, M., Raymond, S. N., et al. (Sept. 2017). “Breaking the Chains: Hot Super-Earth Systems from Migration and Disruption of Compact Resonant Chains.” In: *Monthly Notices of the Royal Astronomical Society* 470.2, pp. 1750–1770. ISSN: 0035-8711. DOI: `10.1093/mnras/stx1232`.

Izidoro, A., Bitsch, B., Raymond, S. N., et al. (June 2021). “Formation of Planetary Systems by Pebble Accretion and Migration. Hot Super-Earth Systems from Breaking Compact Resonant Chains.” In: *Astronomy and Astrophysics* 650, A152. ISSN: 0004-6361. DOI: `10.1051/0004-6361/201935336`.

Izidoro, A., Raymond, S. N., Morbidelli, A., et al. (Feb. 2015). “Gas Giant Planets as Dynamical Barriers to Inward-Migrating Super-Earths.” In: *The Astrophysical Journal* 800, p. L22. ISSN: 0004-637X. DOI: `10.1088/2041-8205/800/2/L22`.

Izidoro, A., Schlichting, H. E., Isella, A., et al. (Nov. 2022). “The Exoplanet Radius Valley from Gas-driven Planet Migration and Breaking of Resonant Chains.” In: *The Astrophysical Journal* 939, p. L19. ISSN: 0004-637X. DOI: `10.3847/2041-8213/ac990d`.

Jacobson, R. A. (Nov. 2022). “The Orbits of the Main Saturnian Satellites, the Saturnian System Gravity Field, and the Orientation of Saturn’s Pole.” In: *The Astronomical Journal* 164, p. 199. ISSN: 0004-6256. DOI: `10.3847/1538-3881/ac90c9`.

Jensen, D. & Millholland, S. C. (Oct. 2022). “Inferred Properties of Planets in Mean-motion Resonances Are Biased by Measurement Noise.” In: *The Astronomical Journal* 164, p. 144. ISSN: 0004-6256. DOI: `10.3847/1538-3881/ac86c5`.

Jontof-Hutter, D., Ford, E. B., Rowe, J. F., et al. (Mar. 2016). “Secure Mass Measurements from Transit Timing: 10 Kepler Exoplanets between 3 and 8 M⊕ with Diverse Densities and Incident Fluxes.” In: *The Astrophysical Journal* 820, p. 39. ISSN: 0004-637X. DOI: `10.3847/0004-637X/820/1/39`.

Jontof-Hutter, D., Wolfgang, A., Ford, E. B., et al. (May 2021). “Following Up the Kepler Field: Masses of Targets for Transit Timing and Atmospheric Characterization.” In: *The Astronomical Journal* 161, p. 246. ISSN: 0004-6256. DOI: `10.3847/1538-3881/abd93f`.

Kane, S. R., Arney, G. N., Byrne, P. K., et al. (Feb. 2021). “The Fundamental Connections between the Solar System and Exoplanetary Science.” In: *Journal of Geophysical Research (Planets)* 126, e06643. ISSN: 0148-0227. DOI: `10.1029/2020JE006643`.

Karney, C. F. F. (Sept. 1983). “Long-Time Correlations in the Stochastic Regime.” In: *Physica D: Nonlinear Phenomena* 8.3, pp. 360–380. ISSN: 0167-2789. DOI: `10.1016/0167-2789(83)90232-4`.

Klavetter, J. J. (Nov. 1989). “Rotation of Hyperion. II. Dynamics.” In: *The Astronomical Journal* 98, p. 1855. ISSN: 0004-6256. DOI: `10.1086/115264`.

Kley, W., Lee, M. H., Murray, N., et al. (July 2005). "Modeling the Resonant Planetary System GJ 876." In: *Astronomy and Astrophysics* 437, pp. 727–742. ISSN: 0004-6361. DOI: `10.1051/0004-6361:20052656`.

Kley, W. & Nelson, R. P. (Sept. 2012). "Planet-Disk Interaction and Orbital Evolution." In: *Annual Review of Astronomy and Astrophysics* 50, pp. 211–249. ISSN: 0066-4146. DOI: `10.1146/annurev-astro-081811-125523`.

Kreidberg, L. (Nov. 2015). "Batman: BAsic Transit Model cAlculatioN in Python." In: *Publications of the Astronomical Society of the Pacific* 127, p. 1161. ISSN: 0004-6280. DOI: `10.1086/683602`.

Kruijer, T. S., Burkhardt, C., Budde, G., et al. (June 2017). "Age of Jupiter Inferred from the Distinct Genetics and Formation Times of Meteorites." In: *Proceedings of the National Academy of Science* 114, pp. 6712–6716. ISSN: 0027-8424. DOI: `10.1073/pnas.1704461114`.

Kunimoto, M. & Matthews, J. M. (June 2020). "Searching the Entirety of Kepler Data. II. Occurrence Rate Estimates for FGK Stars." In: *The Astronomical Journal* 159, p. 248. ISSN: 0004-6256. DOI: `10.3847/1538-3881/ab88b0`.

Lainey, V., Casajus, L. G., Fuller, J., et al. (June 2020). "Resonance Locking in Giant Planets Indicated by the Rapid Orbital Expansion of Titan." In: *Nature Astronomy* 4, pp. 1053–1058. ISSN: 2397-3366. DOI: `10.1038/s41550-020-1120-5`.

Lainey, V., Jacobson, R. A., Tajeddine, R., et al. (Jan. 2017). "New Constraints on Saturn's Interior from Cassini Astrometric Data." In: *Icarus* 281, pp. 286–296. ISSN: 0019-1035. DOI: `10.1016/j.icarus.2016.07.014`.

Lainey, V., Karatekin, Ö., Desmars, J., et al. (June 2012). "Strong Tidal Dissipation in Saturn and Constraints on Enceladus' Thermal State from Astrometry." In: *The Astrophysical Journal* 752, p. 14. ISSN: 0004-637X. DOI: `10.1088/0004-637X/752/1/14`.

Lambrechts, M., Johansen, A. & Morbidelli, A. (Dec. 2014). "Separating Gas-Giant and Ice-Giant Planets by Halting Pebble Accretion." In: *Astronomy and Astrophysics* 572, A35. ISSN: 0004-6361. DOI: `10.1051/0004-6361/201423814`.

Laplace, P. S. (1799). *Traité de mécanique céleste*. de l'Imprimerie de Crapelet.

Laskar, J. (Mar. 1989). "A Numerical Experiment on the Chaotic Behaviour of the Solar System." In: *Nature* 338, pp. 237–238. ISSN: 0028-0836. DOI: `10.1038/338237a0`.

Laskar, J. (July 2008). "Chaotic Diffusion in the Solar System." In: *Icarus* 196, pp. 1–15. ISSN: 0019-1035. DOI: `10.1016/j.icarus.2008.02.017`.

Laune, J. T., Rodet, L. & Lai, D. (Dec. 2022). "Apsidal Alignment and Anti-Alignment of Planets in Mean-Motion Resonance: Disc-Driven Migration and Eccentricity Driving." In: *Monthly Notices of the Royal Astronomical Society* 517, pp. 4472–4488. ISSN: 0035-8711. DOI: `10.1093/mnras/stac2914`.

Le Verrier, U. J. J. (1840). "Sur Les Variations Séculaires Des Éléments Elliptiques Des Sept Planetes Principales: Mercure, Vénus, La Terre, Mars, Jupiter, Saturne et Uranus." In: *Journal de Mathématiques Pures et Appliquées* 4.1840, pp. 220–254.

Lee, M. H., Fabrycky, D. & Lin, D. N. C. (Sept. 2013). "Are the Kepler Near-resonance Planet Pairs Due to Tidal Dissipation?" In: *The Astrophysical Journal* 774, p. 52. ISSN: 0004-637X. DOI: `10.1088/0004-637X/774/1/52`.

Lee, M. H. & Peale, S. J. (Mar. 2002). "Dynamics and Origin of the 2:1 Orbital Resonances of the GJ 876 Planets." In: *The Astrophysical Journal* 567, pp. 596–609. ISSN: 0004-637X. DOI: `10.1086/338504`.

Leinhardt, Z. M. & Stewart, S. T. (Jan. 2012). "Collisions between Gravity-dominated Bodies. I. Outcome Regimes and Scaling Laws." In: *The Astrophysical Journal* 745, p. 79. ISSN: 0004-637X. DOI: `10.1088/0004-637X/745/1/79`.

Leleu, A., Alibert, Y., Hara, N. C., et al. (May 2021a). "Six Transiting Planets and a Chain of Laplace Resonances in TOI-178." In: *Astronomy and Astrophysics* 649, A26. ISSN: 0004-6361. DOI: `10.1051/0004-6361/202039767`.

Leleu, A., Chatel, G., Udry, S., et al. (Nov. 2021b). "Alleviating the Transit Timing Variation Bias in Transit Surveys. I. RIVERS: Method and Detection of a Pair of Resonant Super-Earths around Kepler-1705." In: *Astronomy and Astrophysics* 655, A66. ISSN: 0004-6361. DOI: `10.1051/0004-6361/202141471`.

Lissauer, J. J., Ragozzine, D., Fabrycky, D. C., et al. (Nov. 2011). "Architecture and Dynamics of Kepler's Candidate Multiple Transiting Planet Systems." In: *The Astrophysical Journal Supplement Series* 197, p. 8. ISSN: 0067-0049. DOI: `10.1088/0067-0049/197/1/8`.

Lithwick, Y. & Wu, Y. (Sept. 2012). "Resonant Repulsion of Kepler Planet Pairs." In: *The Astrophysical Journal Letters* 756, p. L11. ISSN: 0004-637X. DOI: `10.1088/2041-8205/756/1/L11`.

Lithwick, Y., Xie, J. & Wu, Y. (Dec. 2012). "Extracting Planet Mass and Eccentricity from TTV Data." In: *The Astrophysical Journal* 761, p. 122. ISSN: 0004-637X. DOI: `10.1088/0004-637X/761/2/122`.

Lopez, E. D. & Fortney, J. J. (Oct. 2013). "The Role of Core Mass in Controlling Evaporation: The Kepler Radius Distribution and the Kepler-36 Density Dichotomy." In: *The Astrophysical Journal* 776, p. 2. ISSN: 0004-637X. DOI: `10.1088/0004-637X/776/1/2`.

Luger, R., Sestovic, M., Kruse, E., et al. (June 2017). "A Seven-Planet Resonant Chain in TRAPPIST-1." In: *Nature Astronomy* 1, p. 0129. ISSN: 2397-3366. DOI: `10.1038/s41550-017-0129`.

MacDonald, M. G., Ragozzine, D., Fabrycky, D. C., et al. (Oct. 2016). "A Dynamical Analysis of the Kepler-80 System of Five Transiting Planets." In: *The Astronomical Journal* 152, p. 105. ISSN: 0004-6256. DOI: `10.3847/0004-6256/152/4/105`.

Malhotra, R. (July 1995). "The Origin of Pluto's Orbit: Implications for the Solar System Beyond Neptune." In: *The Astronomical Journal* 110, p. 420. ISSN: 0004-6256. DOI: `10.1086/117532`.

Mamajek, E. E. & Hillenbrand, L. A. (Nov. 2008). "Improved Age Estimation for Solar-Type Dwarfs Using Activity-Rotation Diagnostics." In: *The Astrophysical Journal* 687, pp. 1264–1293. DOI: `10.1086/591785`.

Marcy, G. W., Weiss, L. M., Petigura, E. A., et al. (Sept. 2014). “Occurrence and Core-Envelope Structure of 1-4× Earth-size Planets around Sun-like Stars.” In: *Proceedings of the National Academy of Science* 111, pp. 12655–12660. ISSN: 0027-8424. DOI: `10.1073/pnas.1304197111`.

Masset, F. S., Morbidelli, A., Crida, A., et al. (May 2006). “Disk Surface Density Transitions as Protoplanet Traps.” In: *The Astrophysical Journal* 642, pp. 478–487. ISSN: 0004-637X. DOI: `10.1086/500967`.

Matsumoto, Y. & Kokubo, E. (July 2017). “Formation of Close-in Super-Earths by Giant Impacts: Effects of Initial Eccentricities and Inclinations of Protoplanets.” In: *The Astronomical Journal* 154, p. 27. ISSN: 0004-6256. DOI: `10.3847/1538-3881/aa74c7`.

Matsumoto, Y., Nagasawa, M. & Ida, S. (Nov. 2012). “The Orbital Stability of Planets Trapped in the First-Order Mean-Motion Resonances.” In: *Icarus* 221, pp. 624–631. DOI: `10.1016/j.icarus.2012.08.032`.

Matsumoto, Y. & Ogihara, M. (Apr. 2020). “Breaking Resonant Chains: Destabilization of Resonant Planets Due to Long-term Mass Evolution.” In: *The Astrophysical Journal* 893, p. 43. ISSN: 0004-637X. DOI: `10.3847/1538-4357/ab7cd7`.

Mayor, M. & Queloz, D. (Nov. 1995). “A Jupiter-mass Companion to a Solar-Type Star.” In: *Nature* 378, pp. 355–359. ISSN: 0028-0836. DOI: `10.1038/378355a0`.

Meiss, J. D. (July 1992). “Symplectic Maps, Variational Principles, and Transport.” In: *Reviews of Modern Physics* 64, pp. 795–848. ISSN: 0034-6861. DOI: `10.1103/RevModPhys.64.795`.

Mel’nikov, A. V. (Oct. 2020). “Orientation of Figures of Small Planetary Satellites During Chaotic Rotation.” In: *Solar System Research* 54, pp. 432–441. ISSN: 0038-0946. DOI: `10.1134/S0038094620050068`.

Melnikov, A. V. (Nov. 2014). “Conditions for Appearance of Strange Attractors in Rotational Dynamics of Small Planetary Satellites.” In: *Cosmic Research* 52, pp. 461–471. ISSN: 0023-4206. DOI: `10.1134/S0010952514060045`.

Migaszewski, C. (Oct. 2015). “On the Migration of Two Planets in a Disc and the Formation of Mean Motion Resonances.” In: *Monthly Notices of the Royal Astronomical Society* 453, pp. 1632–1643. ISSN: 0035-8711. DOI: `10.1093/mnras/stv1739`.

Migaszewski, C., Goździewski, K. & Panichi, F. (Feb. 2017). “The Origin and 9:7 MMR Dynamics of the Kepler-29 System.” In: *Monthly Notices of the Royal Astronomical Society* 465, pp. 2366–2380. ISSN: 0035-8711. DOI: `10.1093/mnras/stw2866`.

Migaszewski, C., Słonina, M. & Goździewski, K. (Nov. 2012). “A Dynamical Analysis of the Kepler-11 Planetary System.” In: *Monthly Notices of the Royal Astronomical Society* 427, pp. 770–789. ISSN: 0035-8711. DOI: `10.1111/j.1365-2966.2012.21976.x`.

Millholland, S. (Nov. 2019). “Tidally Induced Radius Inflation of Sub-Neptunes.” In: *The Astrophysical Journal* 886, p. 72. DOI: `10.3847/1538-4357/ab4c3f`.

Millholland, S. & Laughlin, G. (May 2019). “Obliquity-Driven Sculpting of Exoplanetary Systems.” In: *Nature Astronomy* 3.5, pp. 424–433. ISSN: 2397-3366. DOI: `10.1038/s41550-019-0701-7`.

Millholland, S., Laughlin, G., Teske, J., et al. (Mar. 2018). "New Constraints on Gliese 876—Exemplar of Mean-motion Resonance." In: *The Astronomical Journal* 155, p. 106. ISSN: 0004-6256. DOI: `10.3847/1538-3881/aaa894`.

Millholland, S., Wang, S. & Laughlin, G. (Nov. 2017). "Kepler Multi-planet Systems Exhibit Unexpected Intra-system Uniformity in Mass and Radius." In: *The Astrophysical Journal Letters* 849, p. L33. ISSN: 0004-637X. DOI: `10.3847/2041-8213/aa9714`.

Millholland, S. C., He, M. Y., Ford, E. B., et al. (Oct. 2021). "Evidence for a Nondichotomous Solution to the Kepler Dichotomy: Mutual Inclinations of Kepler Planetary Systems from Transit Duration Variations." In: *The Astronomical Journal* 162, p. 166. ISSN: 0004-6256. DOI: `10.3847/1538-3881/ac0f7a`.

Millholland, S. C. & Winn, J. N. (Oct. 2021). "Split Peas in a Pod: Intra-system Uniformity of Super-Earths and Sub-Neptunes." In: *The Astrophysical Journal* 920, p. L34. ISSN: 0004-637X. DOI: `10.3847/2041-8213/ac2c77`.

Mills, S. M., Fabrycky, D. C., Migaszewski, C., et al. (May 2016). "A Resonant Chain of Four Transiting, Sub-Neptune Planets." In: *Nature* 533, pp. 509–512. ISSN: 0028-0836. DOI: `10.1038/nature17445`.

Mills, S. M., Howard, A. W., Petigura, E. A., et al. (May 2019). "The California-Kepler Survey. VIII. Eccentricities of Kepler Planets and Tentative Evidence of a High-metallicity Preference for Small Eccentric Planets." In: *The Astronomical Journal* 157, p. 198. ISSN: 0004-6256. DOI: `10.3847/1538-3881/ab1009`.

Morbidelli, A. (Jan. 2002). *Modern Celestial Mechanics : Aspects of Solar System Dynamics*. Taylor & Francis. ISBN: 978-0-415-27939-0.

Morbidelli, A. (Nov. 2010). "A Coherent and Comprehensive Model of the Evolution of the Outer Solar System." In: *Comptes Rendus Physique* 11, pp. 651–659. DOI: `10.1016/j.crhy.2010.11.001`.

Mordasini, C., Mollière, P., Dittkrist, K.-M., et al. (Apr. 2015). "Global Models of Planet Formation and Evolution." In: *International Journal of Astrobiology* 14, pp. 201–232. DOI: `10.1017/S1473550414000263`.

Morley, C. V., Knutson, H., Line, M., et al. (Feb. 2017). "Forward and Inverse Modeling of the Emission and Transmission Spectrum of GJ 436b: Investigating Metal Enrichment, Tidal Heating, and Clouds." In: *The Astronomical Journal* 153, p. 86. ISSN: 0004-6256. DOI: `10.3847/1538-3881/153/2/86`.

Murray, C. D. & Dermott, S. F. (1999). "Solar System Dynamics." In: *Solar system dynamics by C.D. Murray and S.F. McDermott. (Cambridge, UK: Cambridge University Press), ISBN 0-521-57295-9 (hc.), ISBN 0-521-57297-4 (pbk.).*

Nelson, R. P. & Papaloizou, J. C. B. (May 2004). "The Interaction of Giant Planets with a Disc with MHD Turbulence - IV. Migration Rates of Embedded Protoplanets." In: *Monthly Notices of the Royal Astronomical Society* 350, pp. 849–864. ISSN: 0035-8711. DOI: `10.1111/j.1365-2966.2004.07406.x`.

Nesvorný, D., Chrenko, O. & Flock, M. (Jan. 2022). “TOI-216: Resonant Constraints on Planet Migration.” In: *The Astrophysical Journal* 925, p. 38. issn: 0004-637X. doi: `10.3847/1538-4357/ac36cd`.

Nesvorný, D. & Morbidelli, A. (Oct. 2012). “Statistical Study of the Early Solar System’s Instability with Four, Five, and Six Giant Planets.” In: *The Astronomical Journal* 144, p. 117. issn: 0004-6256. doi: `10.1088/0004-6256/144/4/117`.

Nesvorný, D. & Vokrouhlický, D. (June 2016). “Dynamics and Transit Variations of Resonant Exoplanets.” In: *The Astrophysical Journal* 823, p. 72. issn: 0004-637X. doi: `10.3847/0004-637X/823/2/72`.

Nimmo, F. & Matsuyama, I. (Mar. 2019). “Tidal Dissipation in Rubble-Pile Asteroids.” In: *Icarus* 321, pp. 715–721. issn: 0019-1035. doi: `10.1016/j.icarus.2018.12.012`.

Niţu, I. C., Keith, M. J., Stappers, B. W., et al. (May 2022). “A Search for Planetary Companions around 800 Pulsars from the Jodrell Bank Pulsar Timing Programme.” In: *Monthly Notices of the Royal Astronomical Society* 512, pp. 2446–2459. issn: 0035-8711. doi: `10.1093/mnras/stac593`.

Öberg, K. I., Guzmán, V. V., Walsh, C., et al. (Nov. 2021). “Molecules with ALMA at Planet-forming Scales (MAPS). I. Program Overview and Highlights.” In: *The Astrophysical Journal Supplement Series* 257, p. 1. issn: 0067-0049. doi: `10.3847/1538-4365/ac1432`.

Ogihara, M. & Ida, S. (July 2009). “N-Body Simulations of Planetary Accretion Around M Dwarf Stars.” In: *The Astrophysical Journal* 699, pp. 824–838. issn: 0004-637X. doi: `10.1088/0004-637X/699/1/824`.

Ogihara, M., Morbidelli, A. & Guillot, T. (June 2015). “A Reassessment of the in Situ Formation of Close-in Super-Earths.” In: *Astronomy and Astrophysics* 578, A36. issn: 0004-6361. doi: `10.1051/0004-6361/201525884`.

Ogilvie, G. I. & Lin, D. N. C. (July 2004). “Tidal Dissipation in Rotating Giant Planets.” In: *The Astrophysical Journal* 610, pp. 477–509. issn: 0004-637X. doi: `10.1086/421454`.

Ormel, C. W., Ida, S. & Tanaka, H. (Oct. 2012). “Migration Rates of Planets Due to Scattering of Planetesimals.” In: *The Astrophysical Journal* 758, p. 80. issn: 0004-637X. doi: `10.1088/0004-637X/758/2/80`.

Ormel, C. W. (Jan. 2017). “The Emerging Paradigm of Pebble Accretion.” In: *Formation, Evolution, and Dynamics of Young Solar Systems* 445, p. 197. doi: `10.1007/978-3-319-60609-5_7`.

Owen, J. E. (May 2019). “Atmospheric Escape and the Evolution of Close-In Exoplanets.” In: *Annual Review of Earth and Planetary Sciences* 47, pp. 67–90. issn: 0084-6597. doi: `10.1146/annurev-earth-053018-060246`.

Paardekooper, S., Dong, R., Duffell, P., et al. (July 2023). “Planet-Disk Interactions and Orbital Evolution.” In: 534, p. 685.

Paardekooper, S.-J., Baruteau, C., Crida, A., et al. (Jan. 2010). "A Torque Formula for Non-Isothermal Type I Planetary Migration - I. Unsaturated Horseshoe Drag." In: *Monthly Notices of the Royal Astronomical Society* 401, pp. 1950–1964. ISSN: 0035-8711. DOI: `10.1111/j.1365-2966.2009.15782.x`.

Paardekooper, S.-J., Baruteau, C. & Kley, W. (Jan. 2011). "A Torque Formula for Non-Isothermal Type I Planetary Migration - II. Effects of Diffusion." In: *Monthly Notices of the Royal Astronomical Society* 410, pp. 293–303. ISSN: 0035-8711. DOI: `10.1111/j.1365-2966.2010.17442.x`.

Paardekooper, S.-J., Rein, H. & Kley, W. (Oct. 2013). "The Formation of Systems with Closely Spaced Low-Mass Planets and the Application to Kepler-36." In: *Monthly Notices of the Royal Astronomical Society* 434, pp. 3018–3029. ISSN: 0035-8711. DOI: `10.1093/mnras/stt1224`.

Papaloizou, J. C. B. & Larwood, J. D. (July 2000). "On the Orbital Evolution and Growth of Protoplanets Embedded in a Gaseous Disc." In: *Monthly Notices of the Royal Astronomical Society* 315, pp. 823–833. ISSN: 0035-8711. DOI: `10.1046/j.1365-8711.2000.03466.x`.

Papaloizou, J. C. B. & Terquem, C. (June 2010). "On the Dynamics of Multiple Systems of Hot Super-Earths and Neptunes: Tidal Circularization, Resonance and the HD 40307 System." In: *Monthly Notices of the Royal Astronomical Society* 405, pp. 573–592. ISSN: 0035-8711. DOI: `10.1111/j.1365-2966.2010.16477.x`.

Pascucci, I., Cabrit, S., Edwards, S., et al. (July 2023). "The Role of Disk Winds in the Evolution and Dispersal of Protoplanetary Disks." In: 534, p. 567. DOI: `10.48550/arXiv.2203.10068`.

Peale, S. J., Cassen, P. & Reynolds, R. T. (Mar. 1979). "Melting of Io by Tidal Dissipation." In: *Science* 203, pp. 892–894. ISSN: 0036-8075. DOI: `10.1126/science.203.4383.892`.

Petigura, E. A., Benneke, B., Batygin, K., et al. (Sept. 2018). "Dynamics and Formation of the Near-resonant K2-24 System: Insights from Transit-timing Variations and Radial Velocities." In: *The Astronomical Journal* 156, p. 89. DOI: `10.3847/1538-3881/aaceac`.

Petigura, E. A., Howard, A. W. & Marcy, G. W. (Nov. 2013). "Prevalence of Earth-size Planets Orbiting Sun-like Stars." In: *Proceedings of the National Academy of Science* 110, pp. 19273–19278. ISSN: 0027-8424. DOI: `10.1073/pnas.1319909110`.

Petigura, E. A., Howard, A. W., Marcy, G. W., et al. (Sept. 2017). "The California-Kepler Survey. I. High-resolution Spectroscopy of 1305 Stars Hosting Kepler Transiting Planets." In: *The Astronomical Journal, Volume 154, Issue 3, article id. 107, 20 pp. (2017).* 154, p. 107. ISSN: 0004-6256. DOI: `10.3847/1538-3881/aa80de`.

Petigura, E. A., Livingston, J., Batygin, K., et al. (Jan. 2020). "K2-19b and c Are in a 3:2 Commensurability but out of Resonance: A Challenge to Planet Assembly by Convergent Migration." In: *The Astronomical Journal* 159, p. 2. DOI: `10.3847/1538-3881/ab5220`.

Petit, A. C., Laskar, J. & Boué, G. (Sept. 2018). "Hill Stability in the AMD Framework." In: *Astronomy and Astrophysics* 617, A93. ISSN: 0004-6361. DOI: `10.1051/0004-6361/201833088`.

Petit, A. C., Petigura, E. A., Davies, M. B., et al. (Aug. 2020a). "Resonance in the K2-19 System Is at Odds with Its High Reported Eccentricities." In: *Monthly Notices of the Royal Astronomical Society* 496, pp. 3101–3111. ISSN: 0035-8711. DOI: `10.1093/mnras/staa1736`.

Petit, A. C., Pichierri, G., Davies, M. B., et al. (Sept. 2020b). “The Path to Instability in Compact Multi-Planetary Systems.” In: *Astronomy and Astrophysics* 641, A176. ISSN: 0004-6361. DOI: `10.1051/0004-6361/202038764`.

Petrovich, C., Deibert, E. & Wu, Y. (May 2019). “Ultra-Short-Period Planets from Secular Chaos.” In: *The Astronomical Journal* 157, p. 180. ISSN: 0004-6256. DOI: `10.3847/1538-3881/ab0e0a`.

Pichierri, G., Batygin, K. & Morbidelli, A. (May 2019). “The Role of Dissipative Evolution for Three-Planet, near-Resonant Extrasolar Systems.” In: *Astronomy and Astrophysics* 625, A7. ISSN: 0004-6361. DOI: `10.1051/0004-6361/201935259`.

Pichierri, G. & Morbidelli, A. (June 2020). “The Onset of Instability in Resonant Chains.” In: *Monthly Notices of the Royal Astronomical Society* 494, pp. 4950–4968. ISSN: 0035-8711. DOI: `10.1093/mnras/staa1102`.

Pichierri, G., Morbidelli, A. & Crida, A. (Aug. 2018). “Capture into First-Order Resonances and Long-Term Stability of Pairs of Equal-Mass Planets.” In: *Celestial Mechanics and Dynamical Astronomy* 130, p. 54. ISSN: 0923-2958. DOI: `10.1007/s10569-018-9848-2`.

Plescia, J. B. & Boyce, J. M. (Feb. 1983). “Crater Numbers and Geological Histories of Iapetus, Enceladus, Tethys and Hyperion.” In: *Nature* 301, pp. 666–670. ISSN: 0028-0836. DOI: `10.1038/301666a0`.

Poincaré, H. (1899). *Les méthodes nouvelles de la mécanique céleste*. Gauthier-Villars et fils.

Polycarpe, W., Saillenfest, M., Lainey, V., et al. (Nov. 2018). “Strong Tidal Energy Dissipation in Saturn at Titan’s Frequency as an Explanation for Iapetus Orbit.” In: *Astronomy and Astrophysics* 619, A133. ISSN: 0004-6361. DOI: `10.1051/0004-6361/201833930`.

Poon, S. T. S., Nelson, R. P., Jacobson, S. A., et al. (Feb. 2020). “Formation of Compact Systems of Super-Earths via Dynamical Instabilities and Giant Impacts.” In: *Monthly Notices of the Royal Astronomical Society* 491, pp. 5595–5620. ISSN: 0035-8711. DOI: `10.1093/mnras/stz3296`.

Pu, B. & Wu, Y. (July 2015). “Spacing of Kepler Planets: Sculpting by Dynamical Instability.” In: *The Astrophysical Journal* 807, p. 44. ISSN: 0004-637X. DOI: `10.1088/0004-637X/807/1/44`.

Puranam, A. & Batygin, K. (Apr. 2018). “Chaotic Excitation and Tidal Damping in the GJ 876 System.” In: *The Astronomical Journal* 155, p. 157. ISSN: 0004-6256. DOI: `10.3847/1538-3881/aab09f`.

Quillen, A. C. (Dec. 2011). “Three-Body Resonance Overlap in Closely Spaced Multiple-Planet Systems.” In: *Monthly Notices of the Royal Astronomical Society* 418, pp. 1043–1054. ISSN: 0035-8711. DOI: `10.1111/j.1365-2966.2011.19555.x`.

Quillen, A. C., LaBarca, A. & Chen, Y. (Mar. 2022). “Non-Principal Axis Rotation in Binary Asteroid Systems and How It Weakens the BYORP Effect.” In: *Icarus* 374, p. 114826. ISSN: 0019-1035. DOI: `10.1016/j.icarus.2021.114826`.

Quillen, A. C., Lane, M., Nakajima, M., et al. (Apr. 2020). “Excitation of Tumbling in Phobos and Deimos.” In: *Icarus* 340, p. 113641. ISSN: 0019-1035. DOI: `10.1016/j.icarus.2020.113641`.

Quillen, A. C., Nichols-Fleming, F., Chen, Y.-Y., et al. (Sept. 2017). “Obliquity Evolution of the Minor Satellites of Pluto and Charon.” In: *Icarus* 293, pp. 94–113. ISSN: 0019-1035. DOI: `10.1016/j.icarus.2017.04.012`.

Ramos, X. S., Charalambous, C., Benítez-Llambay, P., et al. (June 2017). “Planetary Migration and the Origin of the 2:1 and 3:2 (near)-Resonant Population of Close-in Exoplanets.” In: *Astronomy and Astrophysics* 602, A101. ISSN: 0004-6361. DOI: `10.1051/0004-6361/201629642`.

Rath, J., Hadden, S. & Lithwick, Y. (June 2022). “The Criterion for Chaos in Three-planet Systems.” In: *The Astrophysical Journal* 932, p. 61. ISSN: 0004-637X. DOI: `10.3847/1538-4357/ac5f57`.

Raymond, S. N., Izidoro, A. & Morbidelli, A. (Dec. 2018). *Solar System Formation in the Context of Extra-Solar Planets*.

Raymond, S. N. & Morbidelli, A. (Feb. 2020). “Planet Formation: Key Mechanisms and Global Models.” In: *arXiv e-prints* 2002, arXiv:2002.05756.

Rein, H. & Papaloizou, J. C. B. (Apr. 2009). “On the Evolution of Mean Motion Resonances through Stochastic Forcing: Fast and Slow Libration Modes and the Origin of HD 128311.” In: *Astronomy and Astrophysics* 497, pp. 595–609. ISSN: 0004-6361. DOI: `10.1051/0004-6361/200811330`.

Rein, H. (Nov. 2012). “Period Ratios in Multiplanetary Systems Discovered by Kepler Are Consistent with Planet Migration.” In: *Monthly Notices of the Royal Astronomical Society* 427, pp. L21–L24. ISSN: 0035-8711. DOI: `10.1111/j.1745-3933.2012.01337.x`.

Rein, H. & Choksi, N. (May 2022). “An Implementation of Stochastic Forces for the N-body Code REBOUND.” In: *Research Notes of the American Astronomical Society* 6, p. 95. ISSN: 2515-5172. DOI: `10.3847/2515-5172/ac6e41`.

Rein, H., Hernandez, D. M., Tamayo, D., et al. (June 2019). “Hybrid Symplectic Integrators for Planetary Dynamics.” In: *Monthly Notices of the Royal Astronomical Society* 485, pp. 5490–5497. ISSN: 0035-8711. DOI: `10.1093/mnras/stz769`.

Rein, H. & Tamayo, D. (Sept. 2015). “WHFAST: A Fast and Unbiased Implementation of a Symplectic Wisdom-Holman Integrator for Long-Term Gravitational Simulations.” In: *Monthly Notices of the Royal Astronomical Society* 452, pp. 376–388. ISSN: 0035-8711. DOI: `10.1093/mnras/stv1257`.

Ricker, G. R., Winn, J. N., Vanderspek, R., et al. (Aug. 2014). “Transiting Exoplanet Survey Satellite (TESS).” In: 9143, p. 914320. DOI: `10.1117/12.2063489`.

Rivera, E. J., Laughlin, G., Butler, R. P., et al. (Aug. 2010). “The Lick-Carnegie Exoplanet Survey: A Uranus-Mass Fourth Planet for GJ 876 in an Extrasolar Laplace Configuration.” In: *The Astrophysical Journal* 719, pp. 890–899. DOI: `10.1088/0004-637X/719/1/890`.

Rogers, J. G. & Owen, J. E. (May 2021). “Unveiling the Planet Population at Birth.” In: *Monthly Notices of the Royal Astronomical Society* 503, pp. 1526–1542. ISSN: 0035-8711. DOI: `10.1093/mnras/stab529`.

Roy, A. E., Walker, I. W., Macdonald, A. J., et al. (Jan. 1988). “Project LONGSTOP.” In: *Vistas in Astronomy* 32, pp. 95–116. ISSN: 0083-6656. DOI: `10.1016/0083-6656(88)90399-6`.

Rubie, D. C., Jacobson, S. A., Morbidelli, A., et al. (Mar. 2015). “Accretion and Differentiation of the Terrestrial Planets with Implications for the Compositions of Early-Formed Solar System Bodies and Accretion of Water.” In: *Icarus* 248, pp. 89–108. ISSN: 0019-1035. DOI: `10.1016/j.icarus.2014.10.015`.

Schlecker, M., Mordasini, C., Emsenhuber, A., et al. (Dec. 2021). “The New Generation Planetary Population Synthesis (NGPPS). III. Warm Super-Earths and Cold Jupiters: A Weak Occurrence Correlation, but with a Strong Architecture-Composition Link.” In: *Astronomy and Astrophysics* 656, A71. ISSN: 0004-6361. DOI: `10.1051/0004-6361/202038554`.

Schultz, K., Spalding, C. & Batygin, K. (Sept. 2021). “The Distribution of Mutual Inclinations Arising from the Stellar Quadrupole Moment.” In: *Monthly Notices of the Royal Astronomical Society* 506, pp. 2999–3009. ISSN: 0035-8711. DOI: `10.1093/mnras/stab1899`.

Seligman, D. & Laughlin, G. (June 2020). “Evidence That 1I/2017 U1 (’Oumuamua) Was Composed of Molecular Hydrogen Ice.” In: *The Astrophysical Journal* 896, p. L8. ISSN: 0004-637X. DOI: `10.3847/2041-8213/ab963f`.

Sessin, W. & Ferraz-Mello, S. (Apr. 1984). “Motion of Two Planets with Periods Commensurable in the Ratio 2:1 Solutions of the Hori Auxiliary System.” In: *Celestial Mechanics* 32, pp. 307–332. ISSN: 0008-8714. DOI: `10.1007/BF01229087`.

Shevchenko, I. I. (Jan. 1999). “The Separatrix Algorithmic Map: Application to the Spin-Orbit Motion.” In: *Celestial Mechanics and Dynamical Astronomy* 73, pp. 259–268. ISSN: 0923-2958. DOI: `10.1023/A:1008367618329`.

Siegel, J. C. & Fabrycky, D. (June 2021). “Resonant Chains of Exoplanets: Libration Centers for Three-body Angles.” In: *The Astronomical Journal* 161, p. 290. ISSN: 0004-6256. DOI: `10.3847/1538-3881/abf8a6`.

Silburt, A. & Rein, H. (Nov. 2015). “Tides Alone Cannot Explain Kepler Planets Close to 2:1 MMR.” In: *Monthly Notices of the Royal Astronomical Society* 453, pp. 4089–4096. ISSN: 0035-8711. DOI: `10.1093/mnras/stv1924`.

Sinclair, A. T. (Apr. 1975). “The Orbital Resonance amongst the Galilean Satellites of Jupiter.” In: *Monthly Notices of the Royal Astronomical Society* 171, pp. 59–72. ISSN: 0035-8711. DOI: `10.1093/mnras/171.1.59`.

Spalding, C. & Batygin, K. (Oct. 2016). “Spin-Orbit Misalignment as a Driver of the Kepler Dichotomy.” In: *The Astrophysical Journal* 830, p. 5. ISSN: 0004-637X. DOI: `10.3847/0004-637X/830/1/5`.

Spalding, C., Marx, N. W. & Batygin, K. (Apr. 2018). “The Resilience of Kepler Systems to Stellar Obliquity.” In: *The Astronomical Journal* 155, p. 167. DOI: `10.3847/1538-3881/aab43a`.

Stewart, S. T. & Leinhardt, Z. M. (May 2012). “Collisions between Gravity-dominated Bodies. II. The Diversity of Impact Outcomes during the End Stage of Planet Formation.” In: *The Astrophysical Journal* 751, p. 32. ISSN: 0004-637X. DOI: `10.1088/0004-637X/751/1/32`.

Tamayo, D., Cranmer, M., Hadden, S., et al. (Aug. 2020a). “Predicting the Long-Term Stability of Compact Multiplanet Systems.” In: *Proceedings of the National Academy of Science* 117, pp. 18194–18205. ISSN: 0027-8424. DOI: `10.1073/pnas.2001258117`.

Tamayo, D., Murray, N., Tremaine, S., et al. (Nov. 2021). "A Criterion for the Onset of Chaos in Compact, Eccentric Multiplanet Systems." In: *The Astronomical Journal* 162, p. 220. ISSN: 0004-6256. DOI: `10.3847/1538-3881/ac1c6a`.

Tamayo, D., Rein, H., Petrovich, C., et al. (May 2017). "Convergent Migration Renders TRAPPIST-1 Long-lived." In: *The Astrophysical Journal* 840, p. L19. ISSN: 0004-637X. DOI: `10.3847/2041-8213/aa70ea`.

Tamayo, D., Rein, H., Shi, P., et al. (Jan. 2020b). "REBOUNDx: A Library for Adding Conservative and Dissipative Forces to Otherwise Symplectic N-body Integrations." In: *Monthly Notices of the Royal Astronomical Society* 491, pp. 2885–2901. ISSN: 0035-8711. DOI: `10.1093/mnras/stz2870`.

Tanaka, H., Takeuchi, T. & Ward, W. R. (Feb. 2002). "Three-dimensional Interaction between a Planet and an Isothermal Gaseous Disk. I. Corotation and Lindblad Torques and Planet Migration." In: *The Astrophysical Journal* 565.2, pp. 1257–1274. ISSN: 0004-637X, 1538-4357. DOI: `10.1086/324713`.

Tanaka, H. & Ward, W. R. (Feb. 2004). "Three-Dimensional Interaction between a Planet and an Isothermal Gaseous Disk. II. Eccentricity Waves and Bending Waves." In: *The Astrophysical Journal* 602, pp. 388–395. ISSN: 0004-637X. DOI: `10.1086/380992`.

Terquem, C. (June 2021). "On a New Formulation for Energy Transfer between Convection and Fast Tides with Application to Giant Planets and Solar Type Stars." In: *Monthly Notices of the Royal Astronomical Society* 503, pp. 5789–5806. ISSN: 0035-8711. DOI: `10.1093/mnras/stab224`.

Terquem, C. & Papaloizou, J. C. B. (Jan. 2007). "Migration and the Formation of Systems of Hot Super-Earths and Neptunes." In: *The Astrophysical Journal* 654, pp. 1110–1120. ISSN: 0004-637X. DOI: `10.1086/509497`.

Terquem, C. & Papaloizou, J. C. B. (Jan. 2019). "First-Order Mean Motion Resonances in Two-Planet Systems: General Analysis and Observed Systems." In: *Monthly Notices of the Royal Astronomical Society* 482, pp. 530–549. ISSN: 0035-8711. DOI: `10.1093/mnras/sty2693`.

Thomas, P. C., Armstrong, J. W., Asmar, S. W., et al. (July 2007). "Hyperion's Sponge-like Appearance." In: *Nature* 448, pp. 50–56. ISSN: 0028-0836. DOI: `10.1038/nature05779`.

Thomas, P. C., Black, G. J. & Nicholson, P. D. (Sept. 1995). "Hyperion: Rotation, Shape, and Geology from Voyager Images." In: *Icarus* 117, pp. 128–148. ISSN: 0019-1035. DOI: `10.1006/icar.1995.1147`.

Thomas, P. C., Tajeddine, R., Tiscareno, M. S., et al. (Jan. 2016). "Enceladus's Measured Physical Libration Requires a Global Subsurface Ocean." In: *Icarus* 264, pp. 37–47. ISSN: 0019-1035. DOI: `10.1016/j.icarus.2015.08.037`.

Thompson, S. E., Coughlin, J. L., Hoffman, K., et al. (Apr. 2018). "Planetary Candidates Observed by Kepler. VIII. A Fully Automated Catalog with Measured Completeness and Reliability Based on Data Release 25." In: *The Astrophysical Journal Supplement Series* 235, p. 38. ISSN: 0067-0049. DOI: `10.3847/1538-4365/aab4f9`.

Tremaine, S. (July 2015). "The Statistical Mechanics of Planet Orbits." In: *The Astrophysical Journal* 807, p. 157. ISSN: 0004-637X. DOI: `10.1088/0004-637X/807/2/157`.

Tsiganis, K., Gomes, R., Morbidelli, A., et al. (May 2005). “Origin of the Orbital Architecture of the Giant Planets of the Solar System.” In: *Nature* 435, pp. 459–461. DOI: `10.1038/nature03539`.

Van Eylen, V. & Albrecht, S. (Aug. 2015). “Eccentricity from Transit Photometry: Small Planets in Kepler Multi-planet Systems Have Low Eccentricities.” In: *The Astrophysical Journal* 808, p. 126. ISSN: 0004-637X. DOI: `10.1088/0004-637X/808/2/126`.

Van Eylen, V., Albrecht, S., Huang, X., et al. (Feb. 2019). “The Orbital Eccentricity of Small Planet Systems.” In: *The Astronomical Journal* 157, p. 61. ISSN: 0004-6256. DOI: `10.3847/1538-3881/aaf22f`.

Vissapragada, S., Jontof-Hutter, D., Shporer, A., et al. (Mar. 2020). “Diffuser-Assisted Infrared Transit Photometry for Four Dynamically Interacting Kepler Systems.” In: *The Astronomical Journal* 159, p. 108. ISSN: 0004-6256. DOI: `10.3847/1538-3881/ab65c8`.

Wang, J. J., Graham, J. R., Dawson, R., et al. (Nov. 2018). “Dynamical Constraints on the HR 8799 Planets with GPI.” In: *The Astronomical Journal* 156, p. 192. ISSN: 0004-6256. DOI: `10.3847/1538-3881/aae150`.

Wang, S. (Dec. 2017). “RV-detected Kepler-multi Analogs Exhibit Intra-system Mass Uniformity.” In: *Research Notes of the American Astronomical Society* 1, p. 26. DOI: `10.3847/2515-5172/aa9be5`.

Wang, S. & Lin, D. N. C. (Apr. 2023). “Dynamical Evolution of Closely Packed Multiple Planetary Systems Subject to Atmospheric Mass Loss.” In: *The Astronomical Journal* 165, p. 174. ISSN: 0004-6256. DOI: `10.3847/1538-3881/acc070`.

Wang, Y., Ormel, C. W., Huang, P., et al. (Aug. 2023). “Atmospheric Recycling of Volatiles by Pebble-Accreting Planets.” In: *Monthly Notices of the Royal Astronomical Society* 523, pp. 6186–6207. ISSN: 0035-8711. DOI: `10.1093/mnras/stad1753`.

Ward, W. R. (July 1986). “Density Waves in the Solar Nebula: Diffential Lindblad Torque.” In: *Icarus* 67, pp. 164–180. ISSN: 0019-1035. DOI: `10.1016/0019-1035(86)90182-X`.

Ward, W. R. (Apr. 1997). “Protoplanet Migration by Nebula Tides.” In: *Icarus* 126, pp. 261–281. ISSN: 0019-1035. DOI: `10.1006/icar.1996.5647`.

Warren, P. H. (Nov. 2011). “Stable-Isotopic Anomalies and the Accretionary Assemblage of the Earth and Mars: A Subordinate Role for Carbonaceous Chondrites.” In: *Earth and Planetary Science Letters* 311, pp. 93–100. ISSN: 0012-821X. DOI: `10.1016/j.epsl.2011.08.047`.

Weiss, L. M., Marcy, G. W., Petigura, E. A., et al. (Jan. 2018). “The California-Kepler Survey. V. Peas in a Pod: Planets in a Kepler Multi-planet System Are Similar in Size and Regularly Spaced.” In: *The Astronomical Journal* 155, p. 48. ISSN: 0004-6256. DOI: `10.3847/1538-3881/aa9ff6`.

Weiss, L. M., Millholland, S. C., Petigura, E. A., et al. (Mar. 2022). “Architectures of Compact Multi-planet Systems: Diversity and Uniformity.” In: *arXiv e-prints*.

Winn, J. N. & Fabrycky, D. C. (Aug. 2015). “The Occurrence and Architecture of Exoplanetary Systems.” In: *Annual Review of Astronomy and Astrophysics, vol. 53, p.409-447* 53, p. 409. ISSN: 0066-4146. DOI: `10.1146/annurev-astro-082214-122246`.

Wisdom, J. (Oct. 1983). “Chaotic Behavior and the Origin of the 3/1 Kirkwood Gap.” In: *Icarus* 56, pp. 51–74. ISSN: 0019-1035. DOI: `10.1016/0019-1035(83)90127-6`.

Wisdom, J. (Nov. 1987). “Rotational Dynamics of Irregularly Shaped Natural Satellites.” In: *The Astronomical Journal* 94, p. 1350. ISSN: 0004-6256. DOI: `10.1086/114573`.

Wisdom, J., Peale, S. J. & Mignard, F. (May 1984). “The Chaotic Rotation of Hyperion.” In: *Icarus* 58, pp. 137–152. ISSN: 0019-1035. DOI: `10.1016/0019-1035(84)90032-0`.

Wolszczan, A. & Frail, D. A. (Jan. 1992). “A Planetary System around the Millisecond Pulsar PSR1257 + 12.” In: *Nature* 355, pp. 145–147. ISSN: 0028-0836. DOI: `10.1038/355145a0`.

Xiang-Gruess, M. & Papaloizou, J. C. B. (May 2015). “Evolutionary Outcomes for Pairs of Planets Undergoing Orbital Migration and Circularization: Second-Order Resonances and Observed Period Ratios in Kepler’s Planetary Systems.” In: *Monthly Notices of the Royal Astronomical Society* 449, pp. 3043–3056. ISSN: 0035-8711. DOI: `10.1093/mnras/stv482`.

Xie, J.-W., Dong, S., Zhu, Z., et al. (Oct. 2016). “Exoplanet Orbital Eccentricities Derived from LAMOST-Kepler Analysis.” In: *Proceedings of the National Academy of Science* 113, pp. 11431–11435. ISSN: 0027-8424. DOI: `10.1073/pnas.1604692113`.

Xu, W. & Lai, D. (July 2017). “Migration of Planets into and out of Mean Motion Resonances in Protoplanetary Discs: Analytical Theory of Second-Order Resonances.” In: *Monthly Notices of the Royal Astronomical Society* 468, pp. 3223–3238. ISSN: 0035-8711. DOI: `10.1093/mnras/stx668`.

Yee, S. W., Tamayo, D., Hadden, S., et al. (Aug. 2021). “How Close Are Compact Multiplanet Systems to the Stability Limit?” In: *The Astronomical Journal* 162, p. 55. ISSN: 0004-6256. DOI: `10.3847/1538-3881/ac00a9`.

Youdin, A. N. & Chiang, E. I. (Feb. 2004). “Particle Pileups and Planetesimal Formation.” In: *The Astrophysical Journal* 601, pp. 1109–1119. ISSN: 0004-637X. DOI: `10.1086/379368`.

Zhu, W., Petrovich, C., Wu, Y., et al. (June 2018). “About 30% of Sun-like Stars Have Kepler-like Planetary Systems: A Study of Their Intrinsic Architecture.” In: *The Astrophysical Journal* 860, p. 101. ISSN: 0004-637X. DOI: `10.3847/1538-4357/aac6d5`.

Zhu, Z., Stone, J. M. & Calvet, N. (Dec. 2023). “A Global 3-D Simulation of Magnetospheric Accretion: I. Magnetically Disrupted Discs and Surface Accretion.” In: *Monthly Notices of the Royal Astronomical Society*. ISSN: 0035-8711. DOI: `10.1093/mnras/stad3712`.

Zink, J. K., Christiansen, J. L. & Hansen, B. M. S. (Mar. 2019). “Accounting for Incompleteness Due to Transit Multiplicity in Kepler Planet Occurrence Rates.” In: *Monthly Notices of the Royal Astronomical Society* 483, pp. 4479–4494. ISSN: 0035-8711. DOI: `10.1093/mnras/sty3463`.